



# Modélisation des cellules solaires pérovskites, des dispositifs optoélectroniques III-V et de la microscopie à sonde de Kelvin

Yong Huang

## ► To cite this version:

Yong Huang. Modélisation des cellules solaires pérovskites, des dispositifs optoélectroniques III-V et de la microscopie à sonde de Kelvin. Optique [physics.optics]. INSA de Rennes, 2018. Français. NNT : 2018ISAR0007 . tel-01881871

**HAL Id: tel-01881871**

**<https://theses.hal.science/tel-01881871>**

Submitted on 26 Sep 2018

**HAL** is a multi-disciplinary open access archive for the deposit and dissemination of scientific research documents, whether they are published or not. The documents may come from teaching and research institutions in France or abroad, or from public or private research centers.

L'archive ouverte pluridisciplinaire **HAL**, est destinée au dépôt et à la diffusion de documents scientifiques de niveau recherche, publiés ou non, émanant des établissements d'enseignement et de recherche français ou étrangers, des laboratoires publics ou privés.



# Thèse

UNIVERSITÉ  
BRETAGNE  
LOIRE

**THESE INSA Rennes**  
sous le sceau de l'Université Bretagne Loire  
pour obtenir le titre de  
DOCTEUR DE L'INSA RENNES  
Spécialité : Photonique

présentée par

**Yong HUANG**

**ECOLE DOCTORALE :** *Matière Molécules Matériaux*  
**LABORATOIRE :** *FOTON*

Drift diffusion modelling  
of perovskite based  
solar cells, III-V  
optoelectronic devices  
and Kelvin probe force  
microscopy

**Thèse soutenue le 14.03.2018**  
devant le jury composé de :

**Bernard Ratier**

Professeur (XLIM, Université de Limoges) / Président

**Peter Reiss**

Chercheur HDR (CEA, Grenoble) / Rapporteur

**Zakaria Djebbour**

MCF HDR (GeePs, Gif-sur-Yvette) / Rapporteur

**Emmanuelle Deleporte**

Professeur (ENS, Cachan) / Examinatrice

**Claudine Katan**

Chargée de recherche CNRS HDR (ISCR, Rennes) / Examinatrice

**Alain Rolland**

Professeur (IUT Lannion / UR1 Rennes) / Co-directeur de thèse

**Jacky Even**

Professeur (FOTON, Rennes) / Directeur de thèse







# Drift diffusion modelling of perovskite solar cells, III-V optoelectronic devices and Kelvin probe force microscopy

Yong HUANG



En partenariat avec





## Acknowledgements

Due to international program between China and France, I got a chance to come here, Rennes and met lots of nice people, who helped me or shared wonderful day with me. Thank you.

I really need to thank you, my supervisor, Jacky EVEN. I remember that was an afternoon, I went to Jacky with my puzzled brain. It was the end of my first year, I still didn't know how to do my thesis, and I began to question myself shall I continue my Ph.D. study? Jacky just asked me to sit down on the table and began to interpret the physical equations like reading poetry in the sunshine. Science was so beautiful to me at that moment. And I also remember the mornings and



the evening, when I noticed Jacky working so hard and I got encouraged to pursue my success. I like the French saying: Nous avons toute la vie pour nous amuser, nous avons toute la mort pour nous reposer. I really enjoyed working with you, Jacky, Laurent, and Alain. It was my pleasure and fortune to be one of the simulation team members.

I am grateful to my collaborators. It was fantastic to have the opportunity to work with you, L. Egan, A. Gheno, S. Vedraïne, J. Bouclé, J. P. Connolly, M. Kepenekian, B. Tsare, X. Che and C. Katan. With a special mention to Katan, who took care of me like my mother in France.

And finally, to my grandmother and parents.  
我所获得的一切属于你们。没有你们的支持，我  
活不到现在。感谢我的奶奶和父母。





# Content

<b>Acknowledgements .....</b>	<b>I</b>
<b>List of Abbreviations .....</b>	<b>i</b>
<b>List of Figures.....</b>	<b>iii</b>
<b>List of Equations .....</b>	<b>v</b>
<b>Chapter 1            Context .....</b>	<b>1</b>
1.1    Global energy issue and photovoltaics .....	1
1.2    Features of perovskite solar cells .....	4
1.2.1    Nature of good absorbers .....	4
1.2.2    Superior architecture and low-cost process.....	5
1.3    Challenges of perovskite solar cells .....	6
1.4    Demand of nano-scale characterization and modelling .....	7
1.5    Introduction of the chapters.....	8
<b>Chapter 2            Theory and objectives .....</b>	<b>11</b>
2.1    Basic carrier transport equations .....	11
2.2    Carrier generation .....	15
2.2.1    Generation by electrical injection .....	15
2.2.2    Generation by optical illumination.....	15
2.3    Carrier recombination .....	16
2.3.1    Band to band recombination in bulk materials .....	16
2.3.2    Recombination through deep trap states .....	17
2.4    Carrier tunneling.....	18
2.5    Ion migration .....	19
2.6    Thermal effect .....	20
<b>Chapter 3            KPFM and C-V modelling .....</b>	<b>23</b>
3.1    Introduction.....	23
3.2    Development of a novel numerical approach to KPFM .....	23
3.2.1    Fundamental concepts.....	23
3.2.2    Theoretical approach to the KPFM using drift-diffusion modelling .....	25





3.2.3	Surface work-function of a $\text{TiO}_x$ slab without surface states .....	25
3.2.4	Surface work-function of a $\text{TiO}_x$ slab with surface states .....	28
3.2.5	Surface photovoltage in a perovskite hetero-structure on $\text{TiO}_x$ .....	29
3.2.6	Conclusion.....	31
3.3	C-V and KPFM on silicon based diffused junctions .....	32
3.3.1	Introduction .....	32
3.3.2	Sample preparation and C-V and KPFM measurements .....	33
3.3.3	Preliminary discussion.....	35
3.4	C-V and KPFM on meso-porous HTM-free PSCs .....	38
3.4.1	Introduction .....	38
3.4.2	Basic properties of HTM-free PSCs.....	39
3.4.3	Capacitance characteristics.....	39
3.4.4	Photovoltaic characteristics .....	42
3.4.5	Preliminary discussion of $V_{\text{CPD}}$ along the cross section of HTM-free PSCs .....	44
3.5	Summary.....	45
<b>Chapter 4</b>	<b>Investigation of PSCs .....</b>	<b>47</b>
4.1	$\text{TiO}_x$ and $\text{WO}_x$ based PSCs .....	47
4.1.1	Introduction to flexible and printable PSCs.....	47
4.1.2	Experiments and characterizations of $\text{WO}_x$ PSCs .....	47
4.1.3	Experimental comparison between $\text{WO}_x$ based and classic $\text{TiO}_x$ based PSCs .....	50
4.1.4	Modelling of $\text{TiO}_x/\text{MAPbI}_3/\text{Spiro-OMeTAD}$ cells .....	51
4.1.5	Modelling of $\text{WO}_x/\text{MAPbI}_3/\text{Spiro-OMeTAD}$ cells.....	55
4.1.6	Discussion.....	57
4.2	Modelling of light-induced $J_{\text{SC}}$ degradation on inverted PSCs.....	57
4.3	Summary.....	61
<b>Chapter 5</b>	<b>Tunnel junctions in 2T-tandem PSC/SSCs.....</b>	<b>63</b>
5.1	Introduction.....	63
5.2	Device structure and simulation .....	65
5.2.1	Silicon tunnel junction.....	65
5.2.2	Modelling of perovskite/silicon tandem solar cells.....	66
5.3	Perspective .....	68
<b>Chapter 6</b>	<b>Electrical properties of III-V/GaP QD structures on silicon for light emission .....</b>	<b>71</b>
6.1	Introduction.....	71
6.2	Architecture and EL characteristics of devices .....	72
6.3	Modelling of electrical properties of QDs.....	72
6.4	Perspective .....	76
<b>Annex I</b>	<b>Material properties for perovskite modelling .....</b>	<b>79</b>
<b>Annex II</b>	<b>KPFM on silicon-based junctions under light .....</b>	<b>81</b>





<b>Annex III Material properties for III-V QDs modelling.....</b>	<b>83</b>
<b>Annex IV Experimental set-ups .....</b>	<b>85</b>
<b>Annex V Simulation of mobile MA ions .....</b>	<b>87</b>
<b>Annex VI EL of QDs under high electric injection .....</b>	<b>89</b>
<b>Resumé.....</b>	<b>91</b>
<b>References.....</b>	<b>101</b>
<b>List of publication .....</b>	<b>117</b>





## List of Abbreviations

A	Device area	k	Boltzmann constant
AR	Auger recombination	LH	Light hole state
AFM	Atomic Force Microscopy	$m_e$	electron effective mass
PV	PhotoVoltaics	$m_h$	hole effective mass
$\alpha, \beta$	Varshni parameters	n	Electron density
$a_f$	Attempt frequency	$n_i$	Intrinsic carrier density
$\alpha_t$	Fitting parameter in Equation 2–24	$N_d$	Donor density
A	Junction area	$N_a$	Acceptor density
AM	Air mass coefficient	p	Hole density
aug	Auger coefficient	q	Elementary charge
BR	Bimolecular radiative recombination	QDs	Quantum dots
C	Capacitance	PSCs	Perovskite solar cells
C-V	Capacitance-voltage	R	Recombination rate
CBM	Conduction band minimum	RRR	Radiative recombination rate
CPD	Contact potential difference	sGaP	Strained GaP
D	Diffusion coefficient	SSCs	Silicon based solar cells
Di	Diffusion coefficient of ions	STM	Scanning Tunneling Microscopy
$d_h$	Hopping distance	SPV	Surface photovoltage
$\vec{E}$	Electric field	SPM	Scanning Probe Microscopy
$E_f$	Fermi level	SIG	Cross section of defects
$E_i$	Intrinsic Fermi level	SPS	Surface Photovoltage Spectroscopy
$E_{fn}$	Quasi-Fermi level for electrons	t	Time
$E_{fp}$	Quasi-Fermi level for holes	$T_L$	Lattice temperature
$E_t$	Energy level of defects	TR	Trap-assisted recombination
$E_{a,i}$	Ion activation energy	T(E)	tunnel probability
$E_{a,t}$	Activation energy of traps	TRPL	Time-Resolved PhotoLuminescence
$e_{n,m}$	Emission rates	VBM	Valence band maximum
ETM	Electron transport material	$V_{bi}$	Built-in potential
EL	ElectroLuminescence	$V_b$	External bias
$E_{f,r}E_{f,l}$	Quasi-Fermi levels on sides of tunnel	$V_{b.anode}$	External bias on anode
$F_i$	Ion induced-current	$V_{CPD}$	Bias neutralising the electrostatic force
FTO	F-doped SnO <sub>2</sub> substrate	$V_{OC}$	Open circuit voltage
G	Generation rate	$v_{th}$	Thermal velocity
h	Planck constant	WKB	Wentzel-Kramers-Brillouin
HH	Heavy hole state	WF	Work-Function
HTM	Hole transport material	WL	Wetting layer
i	Ion density	$Z_i$	Ionic charge
IF	Interfacial layer	$\mu$	Mobility



---

#### List of Abbreviations

---

ITS	Interface trap state	$\mu_i$	Ion mobility
IEA	International Energy Agency	$\epsilon_0$	Vacuum permittivity
J-V	Current-voltage	$\epsilon_r$	Relative static permittivity
$J_n$	Electron current density	1D	One dimensional
$J_p$	Hole current density	$\rho$	Charge density
$J_{sc}$	Short circuit current	$\psi$	Potential
$J_t$	Tunnelling current	$\psi_s$	Surface potential

The subscripts n, p and t are related to electron, hole and trap, respectively.





# List of Figures

Figure 1:1 a) basic operation of a solar cell. b) Evaluation of the whole J-V characteristic. ....	2
Figure 1:2 Schematic J-V characteristics of solar cells a) in the dark and b) under illumination.....	2
Figure 1:3 Research-cell efficiencies over the years certificated by NREL (04-25-2018) .....	3
Figure 1:4 ABX <sub>3</sub> -like cell crystal of halide perovskite absorbers.....	4
Figure 1:5 Band alignment of some materials available for perovskite solar cells <sup>37</sup> .....	5
Figure 2:1 Example of a) static, b) biased and c) illuminated band alignments .....	14
Figure 2:2 Simulation flows for a) solar cell and b) EL .....	15
Figure 2:3 Schematic recombination transition .....	17
Figure 3:1 Illustration of the basic KPFM setup. ....	24
Figure 3:2 Schematic representations of the simulated architectures. ....	26
Figure 3:3 Static band diagram of the FTO/TiO <sub>x</sub> structure.....	27
Figure 3:4 Electrostatic field intensity in the spacer layer .....	27
Figure 3:5 CPD and band alignment of a TiO <sub>x</sub> slab with ITS .....	29
Figure 3:6 Band alignment and carrier distribution of FTO/TiO <sub>x</sub> /MAPbI <sub>3</sub> .....	30
Figure 3:7 Surface photovoltage spectrum .....	31
Figure 3:8 Acceptor doping profile of the silicon wafer deduced from C-V measurements .....	33
Figure 3:9 Schematic representation of the silicon layer.....	34
Figure 3:10 V <sub>CPD</sub> along the cross section of the silicon wafer .....	35
Figure 3:11 Effective electric field extracted as a derivative of the V <sub>CPD</sub> in the dark. ....	35
Figure 3:12 The C-V measured and the assumed doping profiles.....	36
Figure 3:13 Experimental and simulated V <sub>CPD</sub> in the dark and under illumination. ....	37
Figure 3:14 Schematic representations of HTM-free and classic PSCs .....	38
Figure 3:15 Real and modeled architectures along with the static band diagram.....	39
Figure 3:16 Circuit and architectures used for C-V and J-V characteristic. ....	41
Figure 3:17 The computed and experimental (solid line) C-V characteristics.....	42
Figure 3:18 Experimental and simulated J-V characteristics under one sun illumination .....	43
Figure 3:19 a) Static band alignments and b) potential profiles .....	43
Figure 3:20 a) Phase mapping and b) V <sub>CPD</sub> profile.....	45
Figure 4:1 a-g) Schematic procedures of WO <sub>x</sub> based PSC fabrication and h) a real device.....	49
Figure 4:2 Statistics of the performance of PSCs .....	50
Figure 4:3 Static characteristics of TiO <sub>x</sub> based PSCs.....	52
Figure 4:4 Experimental and simulated J-V characteristics of TiO <sub>x</sub> based solar cells. ....	53
Figure 4:5 Computed potential, carrier and ion distribution .....	55
Figure 4:6 Computed a) potential profile and b) ion distribution .....	55
Figure 4:7 Experimental and simulated J-V characteristics of WO <sub>x</sub> -based PSCs .....	56



Figure 4:8 C-V characteristics of WO <sub>x</sub> based PSCs .....	57
Figure 4:9 a) Reversible degradation of J <sub>SC</sub> under light soaking and b) influence of light power <sup>40</sup> .....	58
Figure 4:10 Schematic of inverted PSCs.....	58
Figure 4:11 Experimental and simulated a) C-V and b) J-V characteristics .....	59
Figure 4:12 Carrier distribution under light .....	60
Figure 4:13 Schematic operation mechanism of metastable and stable traps .....	60
Figure 5:1 a) solar spectrum is splitted into two parts and absorbed by b) a tandem solar cell.....	65
Figure 5:2 Characteristic of the tunnel junction as a function of the doping level. ....	66
Figure 5:3 Schematic architecture of a 2T perovskite/silicon tandem solar cell.....	66
Figure 5:4 Simulated photovoltaic properties of tandem cells .....	67
Figure 5:5 Static energy band alignment of a tandem solar cell.....	68
Figure 5:6 J-V characteristics of the individual cells and the tandem one. ....	69
Figure 6:1 Schematic representation of the QD device architecture.....	73
Figure 6:2 a) Experimental and b) computed EL spectra under low electrical injection. ....	74
Figure 6:3 Band alignment in the (In,Ga)As/GaP QDs structure .....	75
Figure 6:4 Carrier distribution and radiative recombination profiles .....	77
Figure S1 Absorption spectrum of various materials .....	79
Figure S2 Reference Solar Spectral Irradiance. ....	80
Figure S3 Experiments and simulation of V <sub>CPD</sub> in the dark and under illumination. ....	81
Figure S4 KPFM set-up (GeePs Lab.) .....	86
Figure S5 Simulated a) MA ion migration and b) potential profile before and after electrical poling .	87
Figure S6 EL characteristics under high continue wave electrical injection. ....	90



## List of Equations

Equation 2–1 Poisson equation .....	11
Equation 2–2 Continuity equations .....	11
Equation 2–3 Drift-diffusion approximation .....	12
Equation 2–4 carrier densities expressed as a function of the Fermi level.....	12
Equation 2–5 Relation between the intrinsic Fermi level and the electric potential and electric field.	12
Equation 2–6 Einstein relation.....	12
Equation 2–7 Boltzmann relation .....	13
Equation 2–8 Definition of quasi-Fermi levels as a function of the intrinsic level .....	13
Equation 2–9 Definition of quasi-Fermi levels as a function of the band edges .....	13
Equation 2–10 Analytic expression for the absorption spectrum.....	16
Equation 2–11 Radiative recombination expression .....	17
Equation 2–12 Carrier emission from energy states within the bandgap.....	18
Equation 2–13 Recombination associated with states in the bandgap .....	18
Equation 2–14 Relation between the carrier lifetime and the deep trap density. ....	18
Equation 2–15 Trap-assisted recombination expression .....	18
Equation 2–16 Tunneling current .....	19
Equation 2–17 Continuity equation for ions.....	19
Equation 2–18 Drift-diffusion equation for ions .....	19
Equation 2–19 Einstein relation for ions.....	20
Equation 2–20 Ion mobility expression.....	20
Equation 2–21 Varshini law for energy bandgap .....	20
Equation 2–22 Temperature dependent thermal velocity .....	20
Equation 2–23 Temperature dependent mobility .....	20
Equation 2–24 Temperature dependent trap density .....	21
Equation 3–1 Determination of contact potential difference.....	24
Equation 3–2 Capacitance-voltage expression .....	40
Equation 3–3 Classic parallel plate capacitance expression .....	41





# Chapter 1 Context

## 1.1 Global energy issue and photovoltaics

Solar energy<sup>1</sup> could be the ultimate solution to surpass in great excess any human energy needs on the earth<sup>2-4</sup> today and even in the space<sup>5</sup> tomorrow. Photovoltaics (PV) as one strategic branch of the solar energy conversion technologies is green and favoured<sup>6</sup>, converting straightforwardly from photons to electrons. The PV phenomenon was discovered in 1839 by A.C. Becquerel and his son A.E. Becquerel. The first solar cell with thin layers of gold on selenium was fabricated<sup>7</sup> in 1883 by Charles Fritts; the photon conversion efficiency (PCE) was close to 1% but the project was stopped due to materials cost. Since then, researchers never stop the investigation of solar cells from a scientific curiosity to a profitable energy solution, suited to an extensive diffusion in the market and effective utilization in the society. The standard solar cell operation is illustrated in Figure 1:1 a); photons are converted to electrons and holes within the absorber materials, then selective carrier transport materials separate and extract the photo-generated carriers to supply power to a load. ETM and HTM are short names for electron and hole transport materials, respectively. The standard circuit for the solar cell electrical characterization is shown on Figure 1:1 b). The related current-voltage (J-V) characteristics are illustrated in the dark and under illumination (Figure 1:2). The short circuit current ( $J_{sc}$ ) and open circuit voltage ( $V_{oc}$ ) are evaluated in addition to the whole J-V characteristic during bias sweeping. Then, the PCE is redefined as the maximum output power ( $P_m$ ) over the illumination power, and a fill factor (FF) is defined as  $P_m/(J_{sc} \cdot V_{oc})$ .

A low PCE of conversion requires very large panel area to produce a significant power. Thus, any material solution far below 20% power conversion efficiency is considered a lesser competitor for massive energy production, though it might be suitable for niche markets.<sup>8</sup> Now as shown in the record chart summarized by NREL (Figure 1:3), the most efficient research-cells<sup>9</sup> are made of four-junction GaAs based concentrators with PCE of 46%, while they are not cost competitive in com-



parison with the first generation, silicon-based ones. Today, the record commercial cell efficiency of silicon based solar cells (SSCs)<sup>10</sup> is 25%, whose installed capacity is about to hit 200 GW and is expected to grow by 500% in 2040.<sup>11</sup> Will all the capacity be made of SSCs or alternative solar cells in the future? The answer appears to be negative for GaAs, facing the inconvenient demand of large production facilities with expensive and high temperature procedures. And the answer becomes even more irresolute after the unexpected appearance of perovskite solar cells (PSCs), with rocket-like rise of PCE in recent years<sup>12,13</sup>. The 2016 champion cell<sup>14</sup> was FAPbI<sub>3</sub> (FA: formamidinium) based PSCs with PCE around 20%, and the record raises to 22.7% in November 2017. It's really a shocking news; the record of PSCs was 3.8% eight years ago<sup>15</sup>, while it took more than 40 years for single crystal SSCs to reach the current record of 26%. Bearing in mind these recent encouraging developments, solar cells might become adequate and reliable solutions to meet the prophecy that “the future is electrifying”. The International Energy Agency (IEA)<sup>11</sup> advocates this prediction in the last outlook, expecting the weight of electricity among world energy consumption to reach 40% by 2040, driven by its increasing use in industries, living standards and the electrification of vehicles in the urban centers.

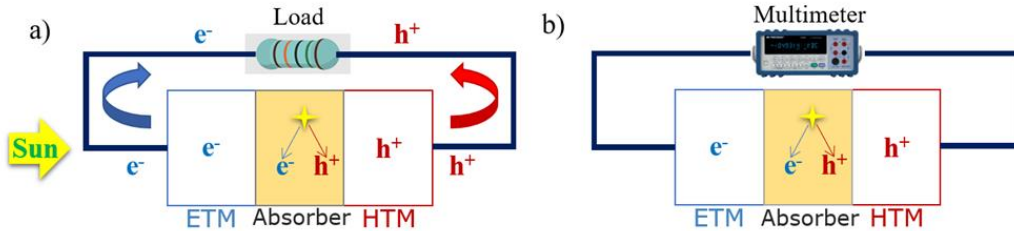


Figure 1:1 a) basic operation of a solar cell. b) Evaluation of the whole J-V characteristic.

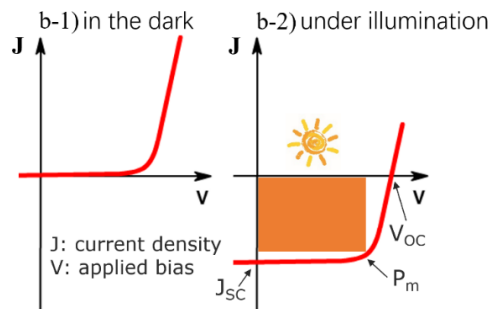


Figure 1:2 Schematic J-V characteristics of solar cells a) in the dark and b) under illumination



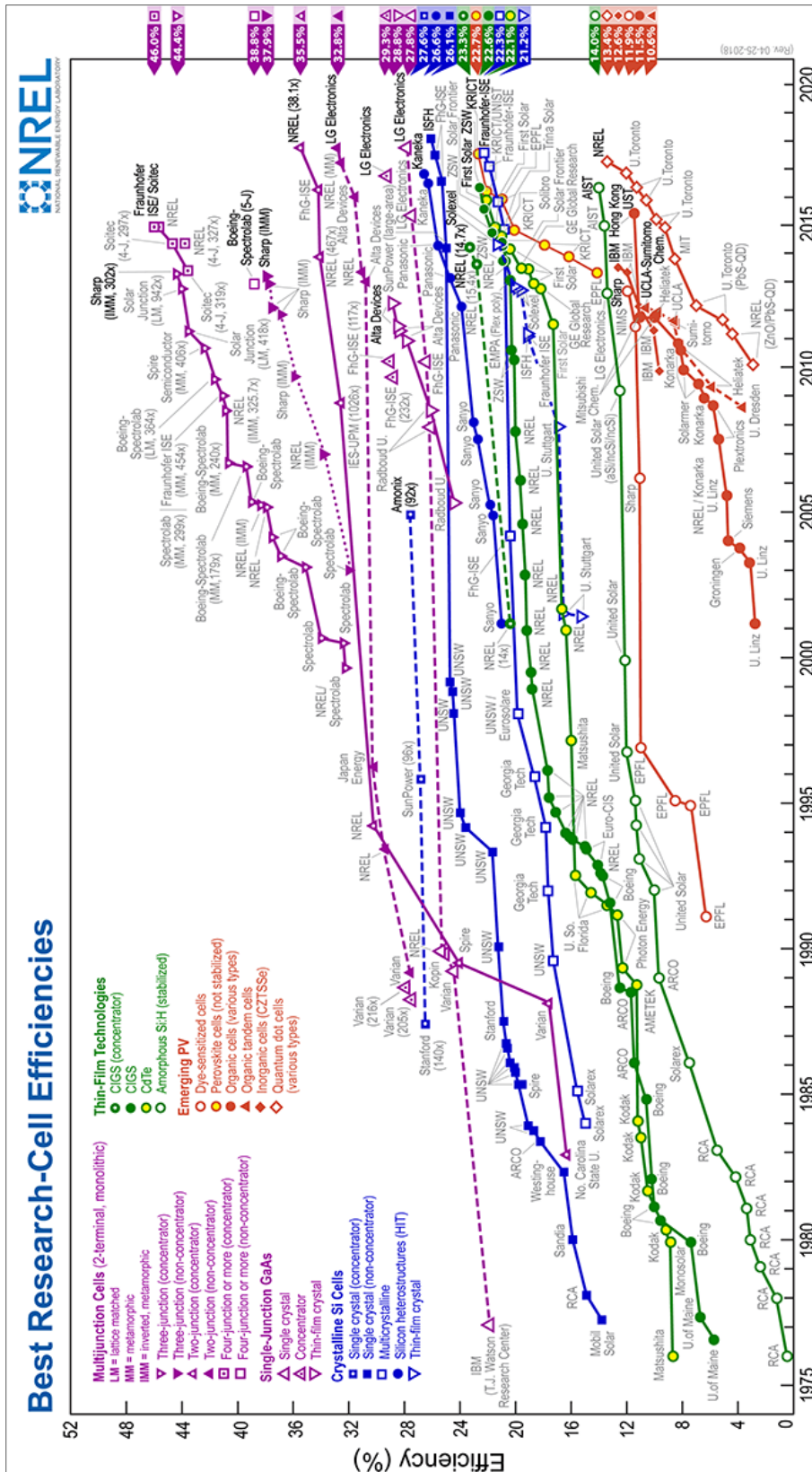


Figure 1:3 Research-cell efficiencies over the years certificated by NREL (04-25-2018)



## 1.2 Features of perovskite solar cells

### 1.2.1 Nature of good absorbers

As seen in Figure 1:4, halide perovskite materials ( $ABX_3$ ) share a similar cell structure with the classic mineral oxide perovskite ( $ABO_3$ ). The cation A site is typically composed of organic methylammonium (MA), formamidinium (FA), or inorganic Cs or Rb cations. At the present stage of PSC progress, cation alloys are put forward for enhancing the stability of perovskite absorbers<sup>16</sup>. Generally, lead (Pb) sits in the B site. Although Pb content in typical halide perovskites is reduced by comparison to vehicle batteries<sup>17,18</sup> and Pb recycled from vehicle batteries may be a solution to synthesize lead-based perovskites<sup>19</sup>, the search for lead-free and environment-friendly perovskite with other alternatives is very active<sup>20,21</sup>. The X site is filled with halide atoms I, Br, or Cl. One of the most widely studied compounds is  $MAPbI_3$ , which will be the major perovskite absorber considered in the following chapters. One may wonder why such simple crystallographic cell structure and simple chemical elements can bring such bright capability to efficiently convert sunlight to charge carriers. Linear combinations of orbitals including spin-orbit coupling (SOC)<sup>22</sup> are essential to explain it from the perspective of electronic band structure. According to atomistic computations<sup>22</sup>, the appropriate absorption and transport properties are afforded by the multibandgap and multivalley nature of their band structure, which are further confirmed by the study<sup>23</sup> of the structural and optical properties of  $MAPbI_3$  from room temperature to 5 K. Furthermore<sup>22</sup>, exciton screening by collective orientational motion of the organic cation MA at room temperature, leads to almost free carriers. The low effective mass of excitons in  $MAPbI_3$  was accurately determined using magneto-reflectivity at very high magnetic fields model<sup>24</sup> in 2015.

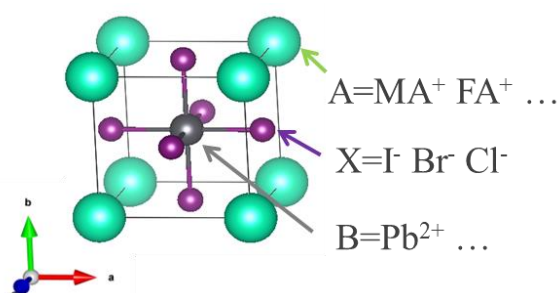


Figure 1:4  $ABX_3$ -like cell crystal of halide perovskite absorbers  
FA<sup>+</sup>: formamidinium cation, MA<sup>+</sup>: methylammonium cation)



### 1.2.2 Superior architecture and low-cost process

The architecture of PSCs has not substantially changed, since the first solid-state devices were introduced<sup>25,26</sup> in 2012. In general, a transparent conducting oxide (TCO) on glass is the substrate where an ETM or an HTM layer is deposited, followed by the perovskite absorbing layer, and covered by the HTM or the ETM layer and a metal contact; the former (n-i-p) configuration refers to standard devices and the latter one (p-i-n) to inverted devices. The thickness of the perovskite layer is generally equal to about 350 nm, and half of it might be wrapped by the meso-porosities of  $\text{TiO}_x$  (a classic ETM)<sup>25</sup>. Ideally, the perovskite absorbing layer is non-intentionally and lightly doped and fully depleted in the static case<sup>27</sup>, leading to drift-dominated carrier transport. Furthermore, the thin perovskite layers can perform well<sup>28,29</sup> with a short carrier diffusion length corresponding to high density of traps<sup>30</sup>. That's why PSCs deposited by simple and low-cost solution procedures<sup>31</sup>, can rival other established technologies based on such as Si, CdTe and GaAs<sup>32,33</sup>. PSCs are also attractive due to the numerous combinations of heterojunctions<sup>34,35</sup> as presented in Figure 1:5. Favorable ETM and HTM generally have work-functions (WF) closed to the conduction band minimum (CBM) and the valence band maximum (VBM) of halide perovskite absorbers, respectively. On the other hand, the band discontinuity of VBM (CBM) at interface of ETM/perovskite (HTM/perovskite) can result in a strong electric field and efficient carrier separation, while single crystal SSCs need extra technologies<sup>36</sup> to relieve recombination at interfaces.

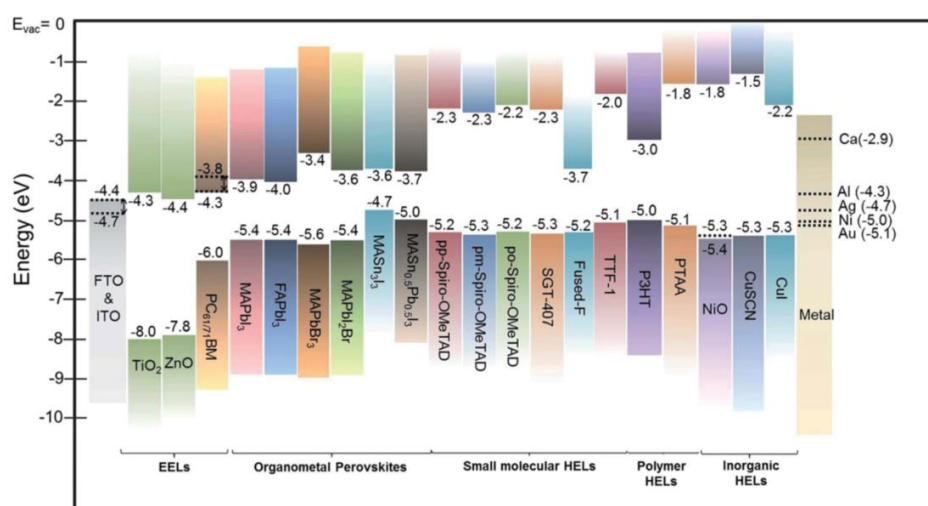


Figure 1:5 Band alignment of some materials available for perovskite solar cells<sup>37</sup>



### 1.3 Challenges of perovskite solar cells

*“Despite impressively high efficiencies, PSCs face challenges such as long-term durability that prevent them from competing with established technologies. However, advancements in materials processing during the past 2 years have yielded remarkable progress in long-term material and device stability, enabling the research community to better identify intrinsic versus extrinsic degradation mechanisms, some of which are summarized here. Despite the rapid improvement in performance, there is still room for tailoring charge carrier recombination, both in the perovskite and at the interfaces within the device, to increase PCEs. Major challenges to long-term stability also remain.”* A review published in a special section of Science journal opened for PSCs in 2017.<sup>38</sup>

Three essential instabilities of PSCs are related to firstly, aging stability under moisture<sup>39</sup>; secondly, the photocurrent ( $J_{SC}$ ) degrades as a function of time during the light soaking<sup>40</sup>; thirdly, the current–voltage (J–V) characteristics of devices depend on the sweeping speed, scan direction and precondition of bias, the so-called anomalous hysteresis effect<sup>41</sup>. The first issue can be circumvented through encapsulation schemes, preventing reactions of the perovskite with water and oxygen<sup>42</sup>. The second source of  $J_{SC}$  degradation is assumed to be caused by metastable MA-associated traps<sup>40</sup> and can be dramatically improved by using mixed cations perovskites<sup>16,43–45</sup> and/or operating cells under low temperature or low external bias<sup>40</sup>. PSCs can recover after a rest in the dark, while SSCs cannot recover after ageing<sup>46</sup>. The third issue is related to the hysteresis effect, which can be suppressed by replacing the electron transport material (ETM) by PCBM<sup>40,47</sup> and/or modifying the ETM/perovskite interface<sup>48–50</sup>, however the mechanism underneath is still not clear.

Since the hysteresis effect observed during PSC operation<sup>41</sup>, researchers never stop carefully investigating possible origins; ferroelectric polarization/depolarization seems to be less likely from the perspective of timescales<sup>51</sup>; charge accumulation and release at the heterojunction are assumed to cause extra current over the normal response<sup>52,53</sup>; high density of ions are supposed to slowly migrate inside perovskite and dominate the global electric field<sup>48</sup>. Direct observations of ion migration inside the perovskite material or devices are reported for MA<sup>54</sup> and iodide<sup>55,56</sup>-related ions, which might further support the models of hysteresis effect caused by charge accumulation and release at interface coupled with ion migration. Most of the available simulation works treat PSCs as normal cells without hysteresis effect and predict cell properties by varying basic material parameters, such



as band structure, radiative coefficient, carrier lifetime, carrier mobility, thickness of layers, or interface recombination rate etc<sup>57–63</sup>. These approaches work well for reproducing local traps induced  $J_{SC}$  degradation<sup>40</sup>, while it doesn't work for the simulation of the hysteresis effect. Some groups have tried to use a static model to illustrate dynamic hysteresis effect by introducing interface traps with/without fixed and abrupt dopants at interfaces<sup>64,65</sup>. Recently, other groups are working on reproducing hysteresis effect, by simulating the simultaneous diffusion of carriers and/or ions as a function of time. However, there are some drawbacks; the scale of scan rate and mobility of ions are not realistic<sup>66</sup>; FF variation under different scan directions can be reproduced, while that of  $V_{OC}$  is not<sup>67,68</sup>; some groups only focus on the ETM/perovskite interface without a consideration of the HTM/perovskite interface<sup>53</sup>, or directly simulate a Schottky interface<sup>69</sup>; some groups reproduce hysteresis effects with a flat or reverse built-in potential inside perovskite in the static case<sup>48</sup>, which is opposite to the observation of potential measured by Kelvin probe force microscopy (KPFM)<sup>70,71</sup>. This last point will be addressed in this work.

In the light of the numerous challenges remaining, the application of PSCs might be questioned on a longer term, even though the performances are still progressing. Looking at the nano-scale PSCs rather than micro-scale SSCs, nano-scale characterization and modelling are even more critical than before for a better understanding of the device operation. More, it might help redirecting PSC research toward other applications such as LED<sup>72</sup>, LD<sup>73</sup>, synaptic devices<sup>74</sup>, memory devices<sup>75</sup>, X-ray detectors<sup>76</sup> or electric-field sensors<sup>77</sup> for example.

## 1.4 Demand of nano-scale characterization and modelling

*“For scanning tunneling microscopy, we brought along some experience in tunneling and angstroms but none in microscopy or surface science. This probably gave us the courage and lightheartedness to start something which should ‘not have worked in principle’ as we were so often told.”* Gerd Binnig and Heinrich Rohrer, Nobel Lecture, December 8th 1986 – Scanning Tunneling Microscopy from Birth to Adolescence<sup>78</sup>.

Since the invention of the Scanning Tunneling Microscope (STM) in 1986, a new family of microscopy techniques called “Scanning Probe Microscopy” (SPM) grows up. It enables today access to extensive surface observation at the nano-scale<sup>79</sup>. One of the attractive followers is the Atomic



Force Microscope (AFM), which can use forces between the tip and the sample to take a three-dimensional (3D) photo of the material surface at nano-scale. The motion of AFM tip is monitored by a photodetector, which can record the reflection of a laser beam on the tip. Compared to STM, AFM is not limited to the measurement on an electrically conductive surface. Based on the invention of AFM in 1986 by G. Binnig, C. Gerber and C.F. Quate<sup>80</sup>, another interested extension showed up and brought the surface potential at the nano-scale to researchers in 1991. KPFM<sup>81</sup> allows identifications of potential profiles and predictions of ultimate performance of solar cells<sup>70,82–84</sup> and lasers<sup>85</sup>, energy levels<sup>86,87</sup> and assessments of heterojunctions<sup>88,89</sup>. After the topography of a surface is studied by AFM, the distance between the tip and sample surface is kept constant to investigate the electrostatic force as with the ancient Kelvin probe. The surface potential ( $\Psi_s$ ) of the samples can be consequently deduced relatively to the WF of the tip. However, due to many artefacts on the surface, it is difficult to further deduce a quantitative analysis of the bulk potential ( $\Psi$ ). And the  $\Psi$  is strongly related to the device operation and performance. Therefore, designing simulations to interpret KPFM measurements is highly required. Technical improvements of KPFM are still underway and advanced nano-scale modelling will be helpful to make progress on various topics<sup>90</sup>.

## 1.5 Introduction of the chapters

In Chapter 2, the simulation flow for drift-diffusion based optoelectronic models is reviewed. It allows addressing various questions, which are essential for the next chapters. 1) Why the  $\Psi$  gives an insight into semiconductor device operation? 2) How carriers are generated and recombined? 3) How is it possible to account for the tunneling phenomenon? 4) How do devices operate with mobile ions? 5) How do thermal aspects influence device operation?

In Chapter 3, a new approach to the modelling of KPFM for hetero-structures in the dark and under illumination is developed. It is used to study the surface potential on top of a  $\text{TiO}_x$  slab and a MAPbI<sub>3</sub> absorber, on the cross section of silicon based diffused junctions and finally, meso-porous  $\text{TiO}_x$  based HTM-free PSCs.

In Chapter 4, PSCs are experimentally and theoretically investigated. PSCs include the classic ones based on  $\text{TiO}_x$ , printable ones based on  $\text{WO}_x$  and inverted ones. The characterizations include J-V,



capacitance-voltage (C-V) and KPFM measurements. These electrical characteristics are simulated to analyze the  $V_{OC}$  losses and the hysteresis effect and the reversible  $J_{SC}$  degradation.

In Chapter 5, silicon-based tunnel junctions are numerically studied for perovskite/silicon based two terminal tandem solar cells. The influence of the doping level in the tunnel junction is discussed.

In Chapter 6, devices based on 5 layers of (In,Ga)As/GaP quantum dots are experimentally and theoretically investigated under electrical injection. The red-shift of emission peak and the thermal quenching of Electroluminescence (EL) intensity are observed and simulated as a function of the temperature. In the simulation, the bandlineups and the traps in the active regions are considered. Carrier transport and recombination in the quantum structure are discussed in the end.

To sum, based on the numerical drift-diffusion model, the PhD study involves the investigation of the perovskite based solar cells, III-V optoelectronic devices and Kelvin probe force microscopy. The fundamental photovoltaic and EL effect are reproduced to interpret the experiments. Additionally, the nano-scale Kelvin probe force microscopy is modelled, which construct a potential dependent bridge between the characterization and simulation. The work is worthwhile for the further development of the optoelectronic devices, including but not limited to the solar cells and the lasers.







## Chapter 2 Theory and objectives

### 2.1 Basic carrier transport equations

First, we consider the Poisson equation, which relates the electric potential to the charge density:

$$\Delta\Psi = -\frac{\rho}{\varepsilon}$$

Equation 2–1 Poisson equation

where  $\Psi$  is the electric potential,  $\rho$  is the charge density and  $\varepsilon$  is the dielectric constant. To understand non-equilibrium phenomena, one must additionally solve the continuity equations for electrons and holes:

$$\begin{aligned}\frac{\partial n}{\partial t} &= \frac{1}{q} \operatorname{div} \vec{J}_n + G_n - R_n \\ \frac{\partial p}{\partial t} &= -\frac{1}{q} \operatorname{div} \vec{J}_p + G_p - R_p\end{aligned}$$

Equation 2–2 Continuity equations

where  $n$  ( $p$ ) is the electron (hole) density,  $t$  is the time,  $q$  is the elementary charge,  $J_n$  ( $J_p$ ) is the electron (hole) current density,  $G$  and  $R$  are the Generation and Recombination rates, respectively. (The subscripts  $n$  ( $p$ ) is related to electron (hole)). All variables are, in general, coordinate and functions of time, to describe the attempt process of carriers to return to equilibrium after a perturbation. Equation 2–2 express the charge conservation. To explicitly take, one must have experimental information about generation, recombination, and diffusion mechanisms. Generation/recombination mechanisms are discussed in the next sections. The electron and hole currents are expressed in the present work, using the drift-diffusion approximation in the present work:



$$\begin{aligned}\vec{J}_n &= qn\mu_n\vec{E} + qD_n\nabla n(x) \\ \vec{J}_p &= qp\mu_p\vec{E} - qD_p\nabla p(x)\end{aligned}$$

Equation 2–3 Drift-diffusion approximation

where  $\mu$  is the mobility,  $D$  the diffusion coefficient and  $\vec{E}$  the electric field. In Equation 2–3, the first terms represent the drift and the second terms the diffusion. Other current mechanisms like tunnelling may also be included through additional expressions and will be described in the next sections. At the equilibrium, the electron and hole densities in a non-degenerate semiconductor can be expressed as:

$$\begin{aligned}n &= n_i \exp\left(\frac{E_f - E_i}{k_B T_L}\right) \\ p &= n_i \exp\left(\frac{E_i - E_f}{k_B T_L}\right)\end{aligned}$$

Equation 2–4 carrier densities expressed as a function of the Fermi level

where  $n_i$  is the intrinsic carrier density,  $E_f$  is the Fermi level,  $k_B$  is the boltzmann constant,  $T_L$  is lattice temperature and  $E_i$  is the intrinsic Fermi level approximately situated at midgap. In the static case, the  $E_f$  is constant (Figure 2:1 a)), and  $E_i$  follows the changes in the electric potential:

$$\frac{dE_i}{dx} = -\frac{qd\Psi}{dx} = -qE$$

Equation 2–5 Relation between the intrinsic Fermi level and the electric potential and electric field.

Since at equilibrium current of electrons and holes are equal, Equation 2–3 to Equation 2–5 lead to the well-known Einstein relation:

$$\frac{D_{n,p}}{\mu_{n,p}} = \frac{k_B T_L}{q}$$

Equation 2–6 Einstein relation

as well as to the Boltzmann relations:



$$n(V_2) = n(V_1) \exp \left[ \frac{e(V_2 - V_1)}{k_B T_L} \right]$$

$$p(V_2) = p(V_1) \exp \left[ \frac{-e(V_2 - V_1)}{k_B T_L} \right]$$

Equation 2–7 Boltzmann relation

where the  $V$  is the local electrostatic potential, the subscripts ‘1’ and ‘2’ correspond to two different locations in the device.

Under non-equilibrium conditions, the Fermi level is not defined and therefore Equation 2–4 are not valid. However, for small perturbations with respect to the equilibrium, they may be replaced with the approximation:

$$n = n_i \exp \left( \frac{E_{fn} - E_i}{k_B T_L} \right)$$

$$p = n_i \exp \left( \frac{E_i - E_{fp}}{k_B T_L} \right)$$

Equation 2–8 Definition of quasi-Fermi levels as a function of the intrinsic level

where  $E_{fn}$  and  $E_{fp}$  are the electron and hole quasi-Fermi levels, respectively. Equation 2–8 retain the functional form<sup>91</sup> of Equation 2–4. But under bias (Figure 2:1 b)) or illumination (Figure 2:1 c)),  $E_f$  will be splitted into  $E_{fn}$  and  $E_{fp}$ ; the former moves upwards whereas the latter moves downwards. Using band edges as references, Equation 2–8 can transform into the well-known equations with the effective density of states in the conduction band ( $N_C$ ) and the valence band ( $N_V$ ), respectively:

$$n = N_C \exp \left( \frac{E_{fn} - CBM}{k_B T_L} \right)$$

$$p = N_V \exp \left( \frac{VBM - E_{fp}}{k_B T_L} \right)$$

Equation 2–9 Definition of quasi-Fermi levels as a function of the band edges

The Poisson Equation 2–1 and the two continuities Equation 2–2 form a set of three coupled differential equations for three unknown functions: the electron density ( $n$ ), the hole density ( $p$ ) and the



electric potential ( $\Psi$ ). The last one is the bulk potential mentioned before inside the devices, related to the surface states and the surface potential ( $\Psi_s$ ) characterized by KPFM measurements. In this work, the problem is numerically solved using the simulator Atlas of Silvaco software<sup>92</sup>, based on the finite element method. The related simulation flow is shown in Figure 2:2.

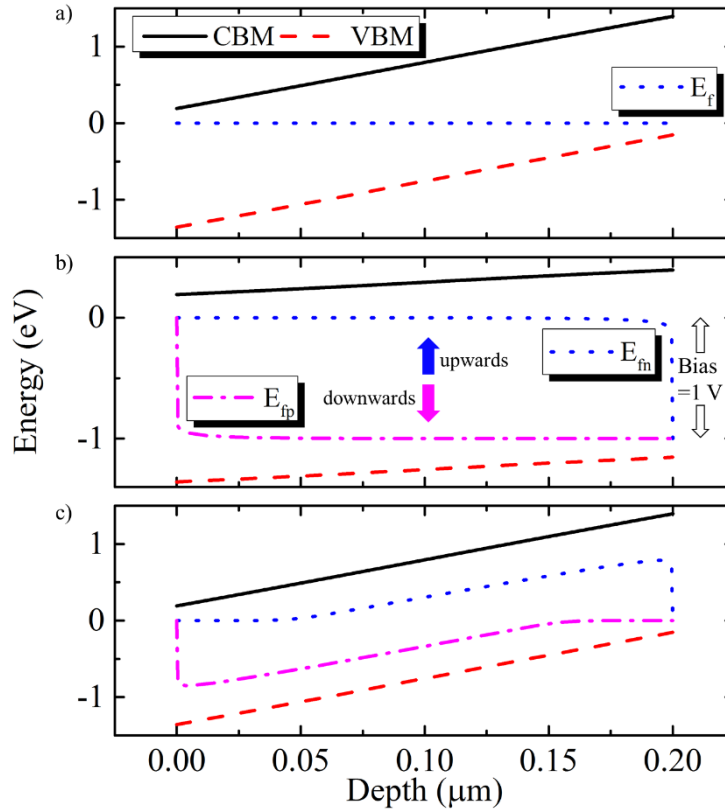


Figure 2:1 Example of a) static, b) biased and c) illuminated band alignments  
The structures in a) and c) are in the short circuit, therefore two terminals of Fermi level are constant of zero. Structure in b) is under bias of 1 V, for example, therefore the  $E_f$  difference between two terminals is 1 V.



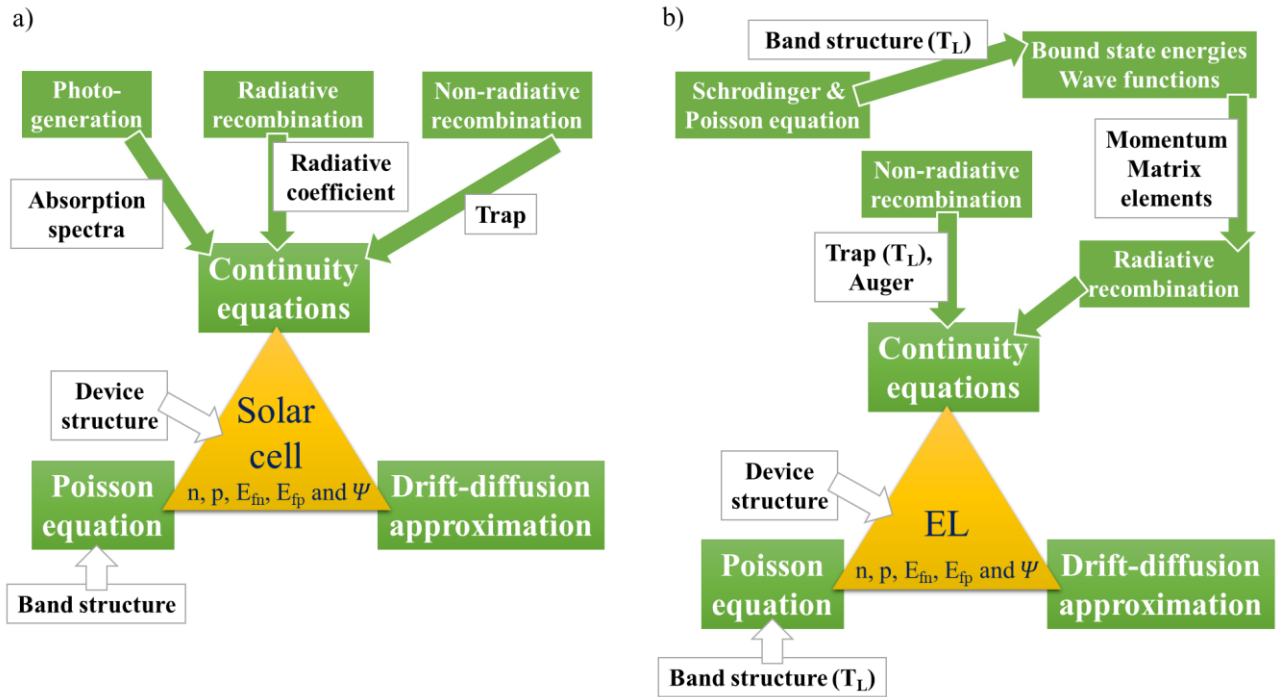


Figure 2:2 Simulation flows for a) solar cell and b) EL  
The input parameters and computation steps are indicated in open and solid squares, respectively.  $T_L$  in brackets indicates the temperature dependent parameters.

## 2.2 Carrier generation

### 2.2.1 Generation by electrical injection

Extra carriers can be injected into the devices under bias. In the Silvaco code, the boundary conditions for the band alignment depend on the external bias (Figure 2:1 b)).

### 2.2.2 Generation by optical illumination

Above bandgap light shining on the surface of a semiconductor leads to the generation of electron-hole pairs, affecting strongly the minority carrier concentration and the band alignment (Figure 2:1 c)). In silicon, this effect is insignificant, however, it is important for narrow gap semiconductors whose specific band structure allows direct transitions, such as halide perovskites; silicon is an indirect bandgap material, whose CBM is located in the X valley<sup>93</sup>. Halide perovskites, (as  $\text{MAPbI}_3$  for example) have the CBM and VBM both in the same valley ( $\Gamma$  valley) with  $E_g$  less than 2 eV, leading to nice capability for photon to carrier conversion<sup>22</sup>. The optical properties are generally characterized by the absorption spectrum, as shown in Figure S1. The absorption depth is given by the



inverse of the absorption coefficient, to describe how the light penetrates the semiconductor before being absorbed. Light with shorter wavelength has a shorter absorption depth. One might notice that the absorption properties of a semiconductor critically affect the solar cell design, such as its thickness, the direction of illumination and the subcell in a tandem configuration. In the Silvaco code, the photo-induced carrier generation is calculated according to the absorption spectrum (Figure S1). In the present study, the cavity effect and the light re-absorption are not taken into consideration. It would be useful for future studies based on texture surfaces<sup>94</sup> or back reflection<sup>95</sup> enhancing photon recycling.

For some halide perovskites without available experimental absorption curves, an analytic expression was used to represent the absorption spectrum:

$$\alpha_{co} = A_{\alpha} \cdot \sqrt{(E_{hv} - E_g)}$$

$$k = \frac{1.24\alpha_{co}}{4\pi E_{hv}}$$

Equation 2–10 Analytic expression for the absorption spectrum

where  $\alpha_{co}$  is absorption coefficient in  $\text{cm}^{-1}$ ,  $A_{\alpha}$  is a prefactor,  $E_{hv}$  is the photon energy in eV and  $k$  is the imaginary part of the refractive index.

## 2.3 Carrier recombination

### 2.3.1 Band to band recombination in bulk materials

In this process, an electron which initially occupies a state in the conduction band relaxes to a state in the valence band (Figure 2:3). In other words, an electron from the conduction band “annihilates” a hole in the crystal. Since the energy of the electron in the final state is lower than in the initial state the process is accompanied by a release of energy typically in the form of a photon (radiative process). This process is known as direct thermal recombination, radiative recombination or bimolecular recombination. In this work, BR is short for such recombination. The radiative process is favored for illumination applications, such as light emitting diodes (LEDs)<sup>96</sup>, while it is considered as a loss for the PV applications<sup>97,98</sup>. Due to its favorable band structure (section 2.2.2), the radiative



coefficient  $\alpha_{rad}$  of a halide perovskite is large, typically four orders of magnitude larger than the one of silicon, as listed in Table S1. The BR process is expressed as

$$R_{BR} = \alpha_{rad} \cdot (n \cdot p - n_i^2)$$

Equation 2–11 Radiative recombination expression

### 2.3.2 Recombination through deep trap states

This recombination process is also known as the Shockley-Read-Hall recombination. Electrons are relaxing from the conduction band to deep trap levels in the bandgap and then to the valence band (Figure 2:3). This two-step transition involves a lower energy release than for the direct transition described in section 2.3.1. The excess energy is transferred to lattice vibrations (phonons). A large difference between band edges and the trap state level ( $E_t$ ) leads to barely zero emission of carriers. On the other hand, for intentionally introduced defects (dopants), the energy levels are expected to be close to the band edges (<50 meV), leading to high emission of carriers and complete ionization of dopants. It is the essential difference between deep traps and shallow dopants from the perspective of energy band theory.

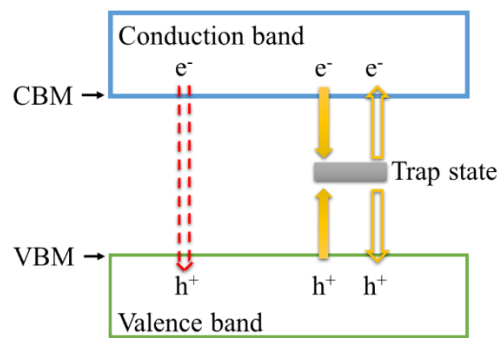


Figure 2:3 Schematic recombination transition

Band to band radiative recombination is indicated by a red dash open arrow. The transitions related to carrier captured and emitted by trap states are indicated by gold solid and open arrows, respectively. CBM is a short name for conduction band minimum and VBM is a short name for valence band minimum.



The carrier emission rate and capture rate expressions of a state within the bandgap are respectively determined as

$$e_n = v_{th,n} \cdot SIG_n \cdot n_i \exp \frac{E_t - E_i}{k_B T_L}$$

$$e_p = v_{th,p} \cdot SIG_p \cdot n_i \exp \frac{E_i - E_t}{k_B T_L}$$

Equation 2–12 Carrier emission from energy states within the bandgap

$$R_{TR} = \frac{n \cdot p - n_i^2}{\tau_n \left[ p + n_i \exp \left( \frac{E_i - E_t}{k_B T_L} \right) \right] + \tau_p \left[ n + n_i \exp \left( \frac{E_t - E_i}{k_B T_L} \right) \right]}$$

Equation 2–13 Recombination associated with states in the bandgap

where TR is a short name for trap-assisted recombination,  $e_{n(p)}$  is the emission rate,  $R_{TR}$  is the capture rate,  $v_{th}$  is the thermal velocity, SIG is the defect cross section. The relation between the carrier lifetime  $\tau$ ,  $v_{th}$  and SIG is:

$$\tau_{n,p} = \frac{1}{v_{th,n,p} \cdot SIG_{n,p} \cdot N_t}$$

Equation 2–14 Relation between the carrier lifetime and the deep trap density.

where  $N_t$  is the density of deep trap states. To reduce the number of parameters,  $v_{th}$  and SIG are set equal for electrons and holes. Thus, the Equation 2–13 can be put into a compact form for deep traps with barely zero emission rate:

$$R_{TR} = \frac{n \cdot p - n_i^2}{\tau(p + n)}$$

Equation 2–15 Trap-assisted recombination expression

## 2.4 Carrier tunneling

Ohmic contacts are necessary for the operation of semiconductor devices under electrical injection. A heavily doped layer is often used to form an Ohmic contact and to enable current tunneling at the metal/semiconductor junction, namely the Schottky junction. For two terminal tandem solar cells, a



band to band tunnel junction is necessary to allow current matching between the top and bottom cells. To approximately compute the tunneling current, an elastic model is proposed within Silvaco:

$$J_t = \frac{q k_B T_L}{2\pi^2 \hbar^3} \sqrt{m_e m_h} \int T(E) \ln \left\{ \frac{1 + \exp[(E_{f,r} - E)/k_B T_L]}{1 + \exp[(E_{f,l} - E)/k_B T_L]} \right\} dE$$

Equation 2–16 Tunneling current

where  $J_t$  is the tunneling current,  $\hbar$  is Planck constant, and  $m_e$  ( $m_h$ ) is the electron (hole) effective mass.  $J_t$  is evaluated for all energy at which tunneling is possible, up to the maximum of the band energy at the interface. The current in the  $[E-E+dE]$  range is integrated using the tunnel probability  $T(E)$ , which is given by the Wentzel-Kramers-Brillouin (WKB) approximation.  $E_{f,r}$  and  $E_{f,l}$  are the quasi-Fermi levels on either side of a tunnel junction.  $J_t$  is then converted into a generation rate for the Ohmic contact at a Schottky junction or into a recombination rate for the tunnel junction in tandem solar cells.

## 2.5 Ion migration

An extension of the standard carrier transport equation set (section 2.1) is proposed to take ion migration into account during the device operation. Like carriers, charged ions are involved within the drift-diffusion framework through a continuity equation:

$$\frac{\partial C_n}{\partial t} = \frac{1}{q} \text{div} \overrightarrow{J_{Cn}}$$

Equation 2–17 Continuity equation for ions

where  $C_n$  is ion density and  $\overrightarrow{J_{Cn}}$  is ion induced-current:

$$\overrightarrow{J_{Cn}} = -q C_n \mu_{Cn} \vec{E} + q D_{Cn} \nabla C_n(x)$$

Equation 2–18 Drift-diffusion equation for ions

where  $D_{Cn}$  is the diffusion coefficient for ions. It is related to the ion mobility  $\mu_{Cn}$  and the ion charge  $Z_{Cn}$ :



$$D_{Cn} = \frac{\mu_{Cn} k_B T_L}{Z_{Cn}}$$

Equation 2–19 Einstein relation for ions

From the perspective of solid state physics,  $\mu_{Cn}$  can be further defined as a production of an ion hopping distance  $d_h$ , an attempt frequency  $a_f$  and an ion activation energy  $E_{ac}$ :

$$\mu_{Cn} = \frac{d_h a_f \exp(-E_{ac}/k_B T_L)}{k_B T_L}$$

Equation 2–20 Ion mobility expression

## 2.6 Thermal effect

For thermal modelling (used in Chapter 6), thermal effect can be taken into account. In a bulk semiconductor, both direct and indirect band gaps in the materials are temperature dependent quantities, with the functional form often fitted to the empirical Varshni law<sup>99</sup>

$$E_g(T_L) = E_g(T_L = 0) - \alpha T_L^2 / (T_L + \beta)$$

Equation 2–21 Varshini law for energy bandgap

where  $\alpha$  and  $\beta$  are adjustable Varshni parameters. And  $v_{th}$  is redefined as a function of  $T_L$  in the active regions:

$$v_{th}(T_L) = \frac{v_{th}(T_L = 300)}{300^2 \cdot T_L^2}$$

Equation 2–22 Temperature dependent thermal velocity

Then the related carrier mobility is defined as a production of the electric field and the lattice temperature:

$$\mu(T_L, E) = v_{th}(T_L)/E$$

Equation 2–23 Temperature dependent mobility

In addition, the density of active traps ( $N_t$ ) is also a temperature dependent quantity:



$$N_t(T_L) = N_{t.total} / (1 + \alpha_t \cdot \exp(E_{at}/k_B T_L))$$

Equation 2–24 Temperature dependent trap density

where  $\alpha_t$  is a fitting parameter and  $E_{at}$  is the activation energy of traps. At low temperature, some of the traps are supposed to be freezed and have no interaction with the carriers. In other words, at low temperature, few traps are considered in our modeling.







## Chapter 3 KPFM and C-V modelling

### 3.1 Introduction

Kelvin probe force microscopy (KPFM) allows a contactless and non-destructive electrical or even optical characterization of interfaces in the dark or under illumination<sup>100</sup>. In-situ or ex-situ applications of KPFM are helpful in process monitoring and quality control of nano-sized devices. It is possible to save time and money assessing the quality of a layered structure before any irreversible degradation. In this work, a new theoretical model is developed to simulate KPFM experiments in steady state and under illumination. The model aims at analyzing KPFM experimental results and correlating the interface properties with the optoelectronic device performance. As far as we know, the theoretical analysis of KPFM under illumination is still in its infancy<sup>70</sup>. First, the method is examined to extract the surface WF on a  $\text{TiO}_x$  slab with and without surface states. Secondly, basic features of KPFM under illumination are simulated including the Surface PhotoVoltage (SPV) and the extraction of material bandgap. Thirdly, the doping profile of a diffused junction on Si is investigated. Finally, the photovoltaic effect of HTM-free PSCs under short circuit is discussed. The present work paves the way for further investigations of more complicated structures by KPFM.

### 3.2 Development of a novel numerical approach to KPFM

#### 3.2.1 Fundamental concepts

The Fermi level ( $E_f$ ) is the energy level which has a 50% probability of being occupied by electrons at any given time. Electrons being Fermions, their energy distributions in the conduction and valence bands are described by the Fermi-Dirac distribution, which is characterised by  $E_f$ . The difference between the vacuum level and  $E_f$  is equivalent to the so-called WF of a material. As shown in Figure 3:1, when a tip and a sample with different  $E_f$  values are electrically connected in the short circuit via an external conductor and the tip is placed close to the surface of the sample, the difference in  $E_f$  drives a current. Electrons flow from one material to the other along the conductor till



the Fermi level is aligned because of this electron redistribution. Correspondingly, the sample surface is positively (or negatively) charged. Then a built-in potential and an electrostatic force appear according to Coulomb's law. This force can be neutralized by applying an external bias between the two materials and injecting charges to exactly reverse the charge flow. When the force is neutralized, the magnitude of external bias equals to the original  $E_f$  difference divided by an elementary charge as the following classic analytical expression.

$$V_{CPD} = \frac{E_{f.tip} - E_{f.sample}}{q}$$

Equation 3-1 Determination of contact potential difference

where CPD is the abbreviation for Contact Potential Difference between the tip and the sample, and  $V_{CPD}$  is the bias neutralising the electrostatic force. Consequently, the Fermi level of the sample ( $E_{f.sample}$ ) can be deduced in contrast to the Fermi level of the tip ( $E_{f.tip}$ ).

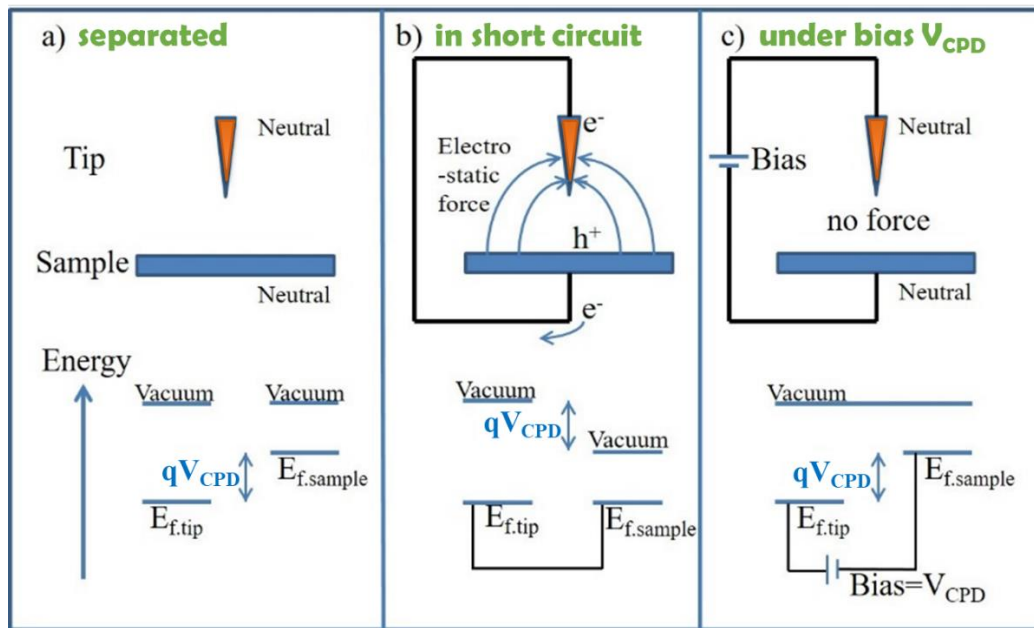


Figure 3:1 Illustration of the basic KPFM setup. Tip and sample are a) separated, b) connected in the short circuit and c) under external bias equal to  $V_{CPD}$ .

A typical KPFM measurement is conducted in the following way. An AC bias at a given frequency is applied between the tip and the sample in addition to a DC bias. The electrostatic force compo-



ment at this frequency is proportional to the CPD and it can be nullified by using an electrostatic-force-dependent feedback loop. The sign of the  $V_{CPD}$  depends on whether the bias is applied to the sample or to the tip. The difference between the  $V_{CPD}$  value in the dark and the  $V_{CPD}$  value under illumination is the SPV.

### 3.2.2 Theoretical approach to the KPFM using drift-diffusion modelling

In order to reproduce basic features of KPFM measurements in the dark and under illumination, two simple 1D architectures, referring to the experimental studies<sup>101,102</sup> were designed using the Silvaco codes as shown in Figure 3:2. A 10 nm thick insulator-like spacer layer is inserted between the tip and sample surface to ensure the continuity of the potential. The thickness of the spacer refers to the distance between the tip and the sample surface during KPFM measurements<sup>102</sup>. The spacer layer may correspond to air, or vacuum depending on the KPFM setup. In the present study, the material parameters of this spacer layer are: an energy band gap ( $E_g$ ) of 12 eV, an electron affinity equal to 0 eV and the vacuum dielectric permittivity  $\epsilon_0$ . The surface is defined as the interface between the spacer layer and the sample. The electric field intensity in the spacer layer is computed to investigate the electrostatic interaction between the tip and the sample, leading to the extraction of the surface WF and the  $E_g$  (see next sections for the details). In the study, we focused on the static part of the electrostatic force without taking the oscillating forces into account. The oscillating forces are necessary to perform topography measurements. The reader can refer to the text book by Sade-wasser and Glatzel<sup>103</sup> for a more detailed discussion of the KPFM measurements in the dark, and to the article by Kronik and Shapira<sup>104</sup> for the KPFM measurements under illumination.

### 3.2.3 Surface work-function of a $TiO_x$ slab without surface states

As illustrated on the left of Figure 3:2, a fluorine doped  $SnO_2$  substrate (FTO) / $TiO_x$  structure is considered to compute the surface WF of  $TiO_x$  (anatase) with and without interface trap states (ITS) at the surface. The footnote x of the  $TiO_x$  refers to the presence of oxygen vacancies, and is linearly dependent on the doping level in the metal oxide<sup>105</sup>. On top of the metallic-like FTO, a layer of heavily n-type doped  $TiO_x$  is necessary to allow intra-band tunnelling and hence efficient electrons transfer through the FTO/ $TiO_x$  interface<sup>106,107</sup>. An interfacial  $TiO_x$  layer (ift $TiO_x$ ) is used on the top of the structure in the present simulation and its thickness is fixed by comparison to existing exper-



imental data<sup>108</sup>. This thin layer is introduced to mimic as simply as possible the effect of the  $\text{TiO}_x$  surface roughness. A computed static band alignment is depicted in Figure 3:3, in which the 300 nm thick  $\text{TiO}_x$  layer is n-type doped<sup>105,109</sup> with  $5 \cdot 10^{18} \text{ cm}^{-3}$  and free of ITS. An intra-band heterojunction tunnelling model<sup>92</sup> is employed at the FTO/ $\text{TiO}_x$  interface. Few carriers are found in the insulator-like spacer layer, leading to a uniform electric field. By applying a bias on the tip and grounding the bottom of the FTO layer, the variation of the electrostatic field in the spacer layer is simulated and presented in Figure 3:4. The electrostatic field, as well as the electrostatic force, is nullified, when the external bias is 0.6 V, which corresponds to a computed WF of 4.2 eV in reference to the tip WF<sup>110</sup> of 4.8 eV. The WF value of 4.2 eV is consistent with the difference between the vacuum level and the  $E_f$  of a heavily doped  $\text{TiO}_x$  layer<sup>34</sup>.

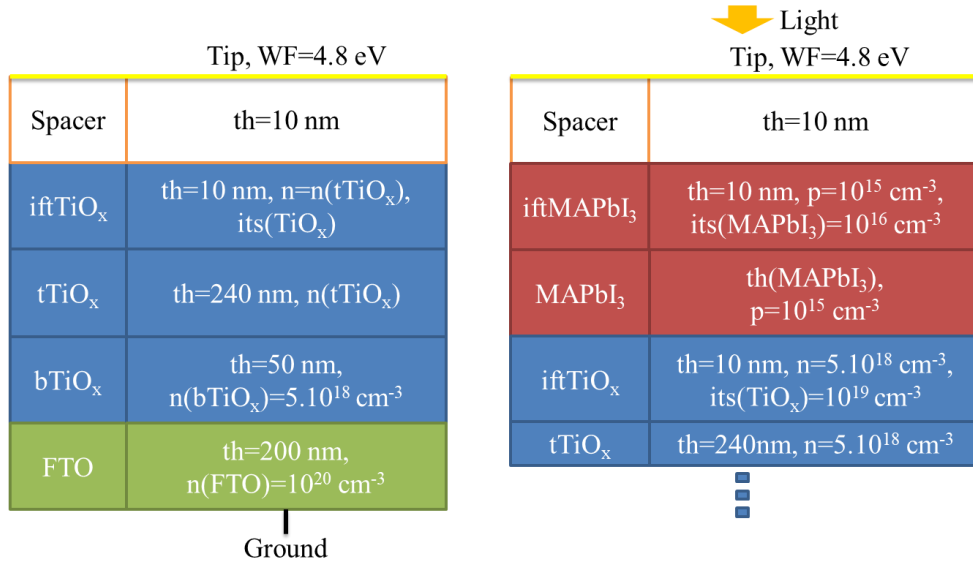


Figure 3:2 Schematic representations of the simulated architectures.

The scanning tip has a WF of 4.8 eV. ‘*ift*’ refers to the top interfacial layer, namely the effective surface. ‘*th*’ is the thickness, n(p) is the n(p)-type doping level and ‘*its*’ is the density of interface trap states. The back of FTO substrate is grounded. An insulator-like spacer layer is inserted between the sample and KPFM tip (see section 2). On the left, the bottom part of  $\text{TiO}_x$  (bTiO<sub>x</sub>) is heavily doped, while the doping level of the top part of  $\text{TiO}_x$  (tTiO<sub>x</sub>) is varied. The structure on the right is an extension of that on the left, in which MAPbI<sub>3</sub> perovskite layers are added on top of the structure. The *its* at  $\text{TiO}_x/\text{MAPbI}_3$  interface and n( $\text{TiO}_x$ ) are fixed as  $10^{19}$  and  $5 \cdot 10^{18} \text{ cm}^{-3}$ , respectively; tTiO<sub>x</sub> with thicknesses of 240 and 90 nm are separately simulated, referring to a total thickness of 300 and 150 nm, respectively. (the structure with th=240 nm is presented here). The light shines on the top of the right architecture.



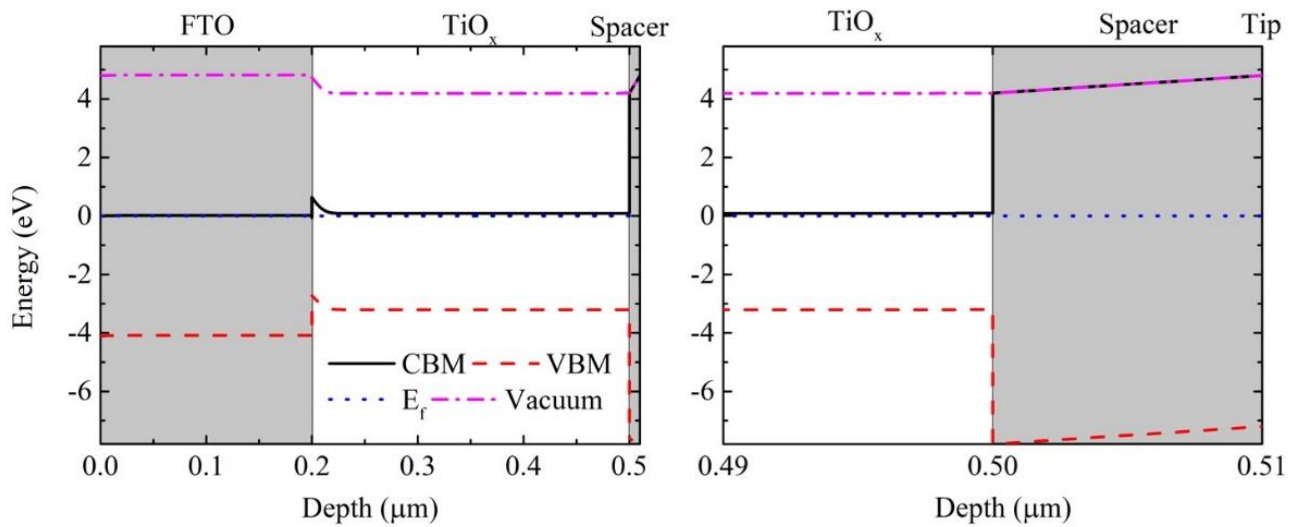


Figure 3:3 Static band diagram of the FTO/TiO<sub>x</sub> structure.

The band structure near the spacer layer is zoomed out on the right, in which the surface of TiO<sub>x</sub> is free of trap state and the tip locates on the rightmost. The n-type doping level of TiO<sub>x</sub> layer is set at  $5 \cdot 10^{18} \text{ cm}^{-3}$ .

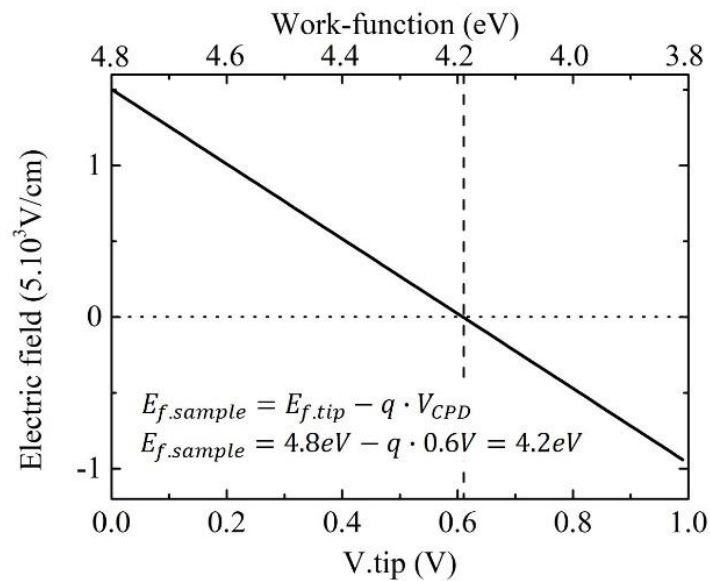


Figure 3:4 Electrostatic field intensity in the spacer layer

The corresponding WF values are given on the top axis. The figure illustrates how the contact potential difference (0.6 V) is deduced from the simulation where an electric field equals to zero. The WF of the tip (4.8 eV) is considered to calculate the surface WF of the sample (4.2 eV), as shown as the inset.



### 3.2.4 Surface work-function of a $\text{TiO}_x$ slab with surface states

Collaboration with A. Gheno and S. Vedraïne (XLIM laboratory, Limoges)

Unlike the periodic structure of an ideal crystalline semiconductor, the termination of the periodic structure of a semiconductor at an interface may form dipoles and/or localized electronic states, which might act as trap states with an energy level within the semiconductor bandgap. The formation of these states is normally due to dangling bonds; interface reconstruction or a change in the chemical bonding configuration, steps and kinks or external atoms captured on the surface. The surface WF of heavily n-doped  $\text{TiO}_x$  measured by KPFM<sup>102</sup> is as high as 4.5 eV on the top of FTO, or even higher as 5.2 eV on the top of glass. It is normally associated to a rather low doping level in the bulk of  $\text{TiO}_x$ . However, as mentioned before, the doping level of  $\text{TiO}_x$  shall be high enough to ensure tunneling at the FTO/ $\text{TiO}_x$  interface. The present work will analyse this contradiction by introducing surface trap states.

Computations with trap states on the  $\text{TiO}_x$  surface are summarised in Figure 3:5 a).  $\text{TiO}_x$  layer of 50 nm near the FTO layer corresponds to a high doping level of  $5 \cdot 10^{18} \text{ cm}^{-3}$  for tunnelling<sup>109</sup>, while the doping level of the top part of  $\text{TiO}_x$  and the surface trap state density are varied from  $5 \cdot 10^{17}$  to  $10^{19} \text{ cm}^{-3}$ . The  $E_t$  is located 1 eV below the conduction band and the  $\text{SIG}^{111}$  is equal to  $8.3 \cdot 10^{13} \text{ cm}^{-2}$ . A high density of surface states and a low doping level of the bulk material may lead to WF variations as large as 0.8 eV. The WF of 4.5 eV consistent with experimental results can be reproduced when  $n(\text{TiO}_x)$  and  $\text{its}(\text{TiO}_x)$  equal  $5 \cdot 10^{18}$  and  $10^{19} \text{ cm}^{-3}$ , respectively. The relative static band alignment is presented in Figure 3:5 b). The carrier redistribution near the free surface results in a space charge region, and a similar phenomenon could be found at the same location in Figure 3:3 but with rather low extent. Generally, a high density of active ITS is harmful for optoelectronic devices<sup>112</sup>, the present work suggests that the combination of KPFM measurement and theoretical computation might be an efficient way to study this issue and further improve device performance.



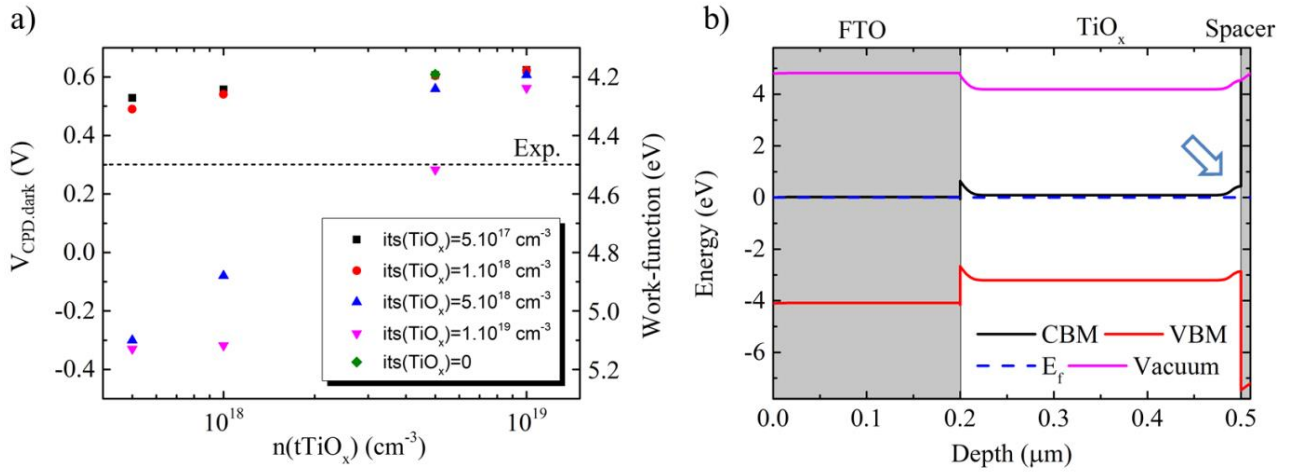


Figure 3:5 CPD and band alignment of a  $TiO_x$  slab with ITS  
a) Static Contact Potential Difference ( $V_{CPD,Dark}$ ) and WF as a function of the doping level,  $n(tTiO_x)$  and the surface trap density,  $its(TiO_x)$ . b) Schematic of the static band alignment with acceptor-like trap states of  $10^{19} cm^{-3}$  on the top of a  $5 \cdot 10^{18} cm^{-3}$  doped  $TiO_x$ . The open arrow indicates the surface trap-induced depletion region very close to the spacing layer.

### 3.2.5 Surface photovoltage in a perovskite hetero-structure on $TiO_x$

The analysis of  $V_{CPD}$  changes induced by illumination can afford quantitative characterization of the bandgap, the doping type, the carrier diffusion length and lifetime, and even energy levels in quantum structures and carrier accumulation in thin film structures<sup>113</sup>. Since the pioneering work of Brattain and Bardeen<sup>114</sup> in the early 1950s, the description of surface photovoltaic phenomena has evolved considerably from the fundamental viewpoint while strong progresses have been made for surface and bulk experimental characterizations.

As illustrated on the right of Figure 3:2, a structure FTO/ $TiO_x$ /MAPbI<sub>3</sub> is modelled to investigate SPV in this section. The present theoretical study are compared to the experimental SPV results, which were obtained on MAPbI<sub>3-x</sub>Cl<sub>x</sub> mixed halide perovskites<sup>101</sup>. It is shown in the literature that the Cl content in these alloys is very low and that the chlorine atoms are essentially located in the final structures at the interfaces<sup>115</sup>. Cl atoms are essentially useful for the initial nucleation of the perovskite seeds in the precursor solution and to enhance the crystallinity of the final perovskite films<sup>116</sup>. We thus consider the absorption spectrum (Figure S1) and the band structure of bulk<sup>117</sup> MAPbI<sub>3</sub>, which is more widely investigated. The electronic bandgap of 1.55 eV deduced in the experimental study on SPV<sup>101</sup> is indeed the same as bulk MAPbI<sub>3</sub>. The MAPbI<sub>3</sub> layers with different



thicknesses on the top of the  $\text{TiO}_x$  layer are modelled. The  $\text{MAPbI}_3$  layers are lightly p doped<sup>71,118</sup> and surface trap states of  $10^{16} \text{ cm}^{-3}$  are introduced<sup>119</sup>. The  $E_t$  in the  $\text{MAPbI}_3$  is located at 0.6 eV above the VBM<sup>120</sup>, and the density of trap states at the  $\text{TiO}_x/\text{MAPbI}_3$  interface is set as  $10^{19} \text{ cm}^{-3}$ . The simulated band alignment under illumination is depicted in Figure 3:6 a), in which the light illuminates on the top of a 200 nm  $\text{MAPbI}_3$  layer. Due to the light absorption,  $E_f$  is split into two quasi fermi levels  $E_{fn}$  and  $E_{fp}$ , separately. Related carrier distributions are represented in Figure 3:6 b). Driven by the built-in electric field in the p-n junction, the photon-generated electrons and holes are separated and shifted to different regions; Holes accumulate near the free surface, and electrons are driven to the other side. However, due to high density of the trap states at the  $\text{TiO}_x/\text{MAPbI}_3$  interface, a fraction of the electrons is captured nearby, where a part of the holes is unexpectedly accumulated as well. The detrimental effect of the trap states at the  $\text{TiO}_x/\text{MAPbI}_3$  interface is deleterious for the collection of photon-generated carriers and can directly decrease solar cell efficiency<sup>121</sup>. The SPV, which is the difference between  $V_{\text{CPD}}$  in the dark and under illumination is observed. For example, for the structure in Figure 3:6, the  $V_{\text{CPD}}$  under one sun illumination equals to 0.603 V and that in the dark is 0.275 V, leading to a SPV of 0.328 V.

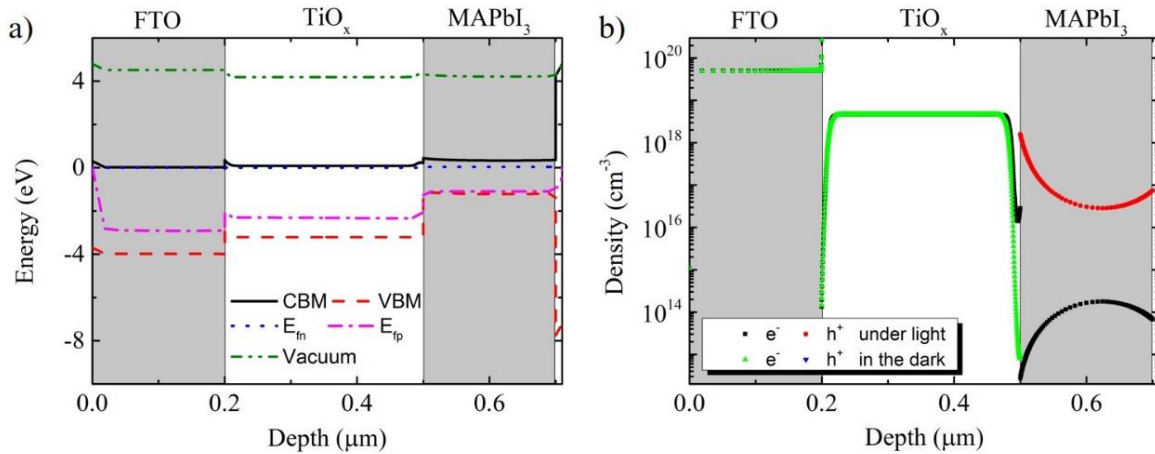


Figure 3:6 Band alignment and carrier distribution of FTO/ $\text{TiO}_x$ / $\text{MAPbI}_3$   
a) Band diagram under one-sun illumination. On the top of  $5 \cdot 10^{18} \text{ cm}^{-3}$  doped  $\text{TiO}_x$ , a slightly p-doped  $\text{MAPbI}_3$  is covered by surface states of  $10^{16} \text{ cm}^{-3}$ . One sun shines on the top of  $\text{MAPbI}_3$ . b) Carrier distribution in static condition and under illumination. Due to the interface trap states, a reduction of the electron density at the  $\text{TiO}_x/\text{MAPbI}_3$  interface is observed in the dark (black) and under illumination (green). The accumulations of photon-generated holes (red) are observed at the  $\text{TiO}_x/\text{MAPbI}_3$  and  $\text{MAPbI}_3/\text{spacer}$  interfaces. In the dark, the hole density in the depleted  $\text{MAPbI}_3$  is too low to be represented within the same scale.



In addition, the SPV is computed in comparison with the experimental data of the Surface Photovoltage Spectroscopy (SPS)<sup>101</sup>, as shown in Figure 3:7 a). The  $E_g$  of MAPbI<sub>3</sub> around 1.55 eV is deduced from the SPV edge and consistent with that from the absorption spectrum<sup>122</sup>. Furthermore, the SPV is calculated as a function of the MAPbI<sub>3</sub> layer thickness and presented in Figure 3:7 b). When the intrinsic MAPbI<sub>3</sub> layer is thinner than 100 nm, the surface WF is close to the surface WF of the underneath TiO<sub>x</sub> layer (4.5 eV) (Stage I). The  $V_{CPD}$  under light is found to be almost constant due to photo-generated holes accumulated at the free surface. However, the  $V_{CPD}$  in the dark progressively decreases, and leads in turn to a variation of SPV (Stage II). When the thickness of the MAPbI<sub>3</sub> layer is very large (Stage III), the saturation value of the surface WF is consistent with that of an individual MAPbI<sub>3</sub> layer. In other words, the influence of the TiO<sub>x</sub> layer is screened by the thick MAPbI<sub>3</sub> layers. When the thickness of the MAPbI<sub>3</sub> layer is 10<sup>4</sup> nm, the surface WF increases up to 5.06 eV.

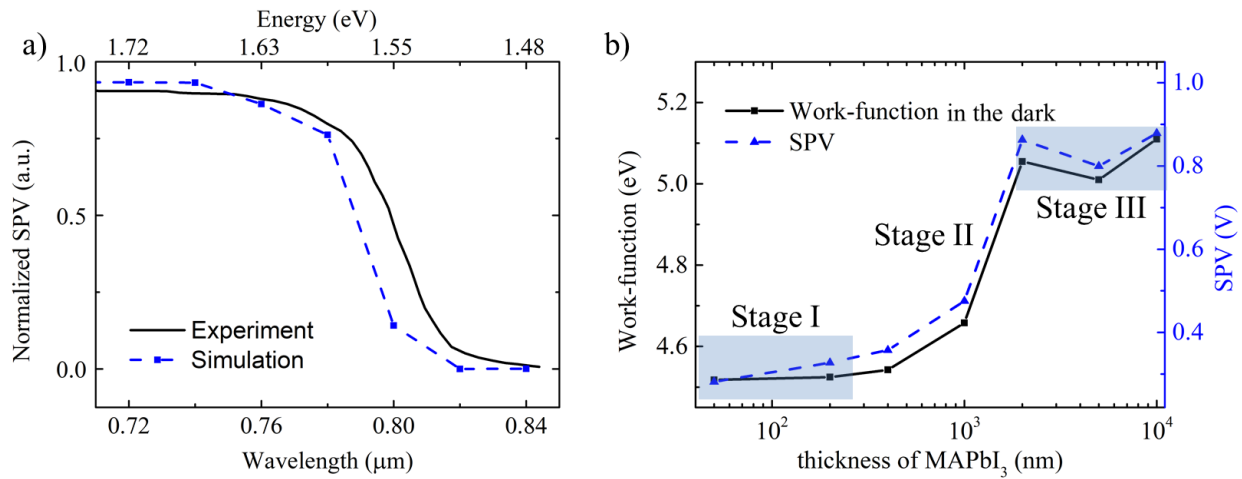


Figure 3:7 Surface photovoltage spectrum

a) Experimental and simulated SPS. The simulated laser power is 1 W/cm<sup>2</sup>. b) Computed surface WF and SPV as a function of the MAPbI<sub>3</sub> layer thickness. The light source corresponds to one sun in b).

### 3.2.6 Conclusion

A new approach to the modelling of KPFM for hetero-structures in the dark and under illumination has been presented. The approach has been evaluated for the FTO/TiO<sub>x</sub> and the FTO/TiO<sub>x</sub>/MAPbI<sub>3</sub> structures. Unexpected surface states on the top of the TiO<sub>x</sub> layer are inferred by the comparison of the theoretical computation and the experimental results. Basic applications of KPFM under illumination are analysed as well. Due to its sensitivity to surface conditions, to photo-generated charges



and to shallow interfaces, the KPFM technique might be helpful to monitor fabrication of planar hetero-structures and devices. Further investigation by combining the KPFM and the modelling on diffused junctions of the silicon (section 3.3), the meso-porous  $\text{TiO}_x$  based HTM-free PSCs (section 3.4) and the  $\text{WO}_x$  based PSCs (section 4.1.2) will be presented in the next sections. The method could be also useful for the study of carrier transport through tunnel junction in tandem solar cells (Chapter 5) and to evaluate the carrier distribution in III-V QDs layers (Chapter 6).

### 3.3 C-V and KPFM on silicon based diffused junctions

#### 3.3.1 Introduction

In silicon based solar cells<sup>123</sup>, the device performance is dominated by the dopant distribution, which is essentially associated with the location of the junction and the depletion width. Hence, to improve the device performance, experimental methods with high resolution in depth, to accurately study the doping profile and the related properties inside solar cells are helpful. Secondary ion mass spectrometry is widely used to profile various kinds of dopant elements, but it cannot pinpoint the active dopants<sup>124</sup>, and is not suited for devices with intentionally-made texture surface to enhance light trapping<sup>125</sup>. Scanning capacitance microscopy and secondary electron detection in scanning electron microscope are sensitive to the carrier concentration and consequently the junction location, but they cannot profile the real density of the active dopants either<sup>125</sup>. The capacitance-voltage (C-V) technique is also not well suited for rough surface<sup>126</sup>, however this method can yield precise net active dopant distribution and built-in potential ( $V_{bi}$ ) on planar structures<sup>127</sup>. By varying the external bias ( $V_b$ ), a dopant density profile can be extracted deep into the structure, anyway the characterization depth is limited by the instrument and/or material stability under electrical pressure. KPFM may yield the potential profile along the cross section of samples with a two-dimensional resolution<sup>128</sup>, while the techniques mentioned before can only lead to a one-dimensional characterization. The sample preparation steps (cleavage, polishing and cleaning) are crucial to achieve accurate measurements<sup>129</sup>, due to the sensitivity of the KPFM to the surface condition (section 3.2.4). In principle, nevertheless, it is hard to avoid the effect of surface terminations, no matter how carefully the samples are prepared. Therefore, the surface potential measured by KPFM is generally discussed qualitatively rather than to yield quantitative information on the potential profile inside the



device. The combination of the experiments and the modelling is proposed here based on the KPFM technique. It is applied along the cross section of a silicon-based diffuse junction.

### 3.3.2 Sample preparation and C-V and KPFM measurements

Collaboration with L. Joseph (ISC-konstanz, Germany) and C. Marchat (GeePs, France).

A first experimental study was performed recently. Planar silicon wafers with diffused  $p^+$ - $n$  junctions are prepared. A lightly  $n$ -doped Silicon layer is symmetrically sandwiched by the heavily  $p$ -doped regions. The doping profile measured by C-V is presented as a black line in Figure 3:8, indicating the  $p$ -doped region near the surface. In addition, the very surface of the silicon wafer is supposed to be covered by non-intentional thin oxide layers after exposing in the air.

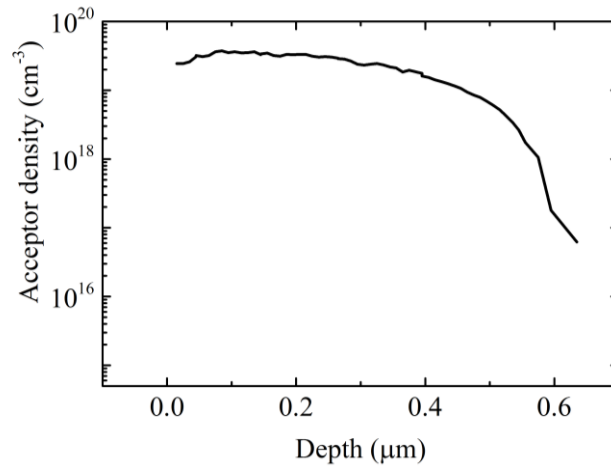


Figure 3:8 Acceptor doping profile of the silicon wafer deduced from C-V measurements

For KPFM measurements, the samples are cleaved down to around  $5 \times 5 \text{ mm}^2$ , and the  $p^+$ - $n$  junctions are exposed, as illustrated in the Figure 3:9. The silicon layer is  $160 \text{ μm}$  thick and the oxide layer is assumed as  $15 \text{ nm}$  thick. The  $V_{CPD}$  along the cross section are measured under different conditions and presented in Figure 3:10. Two  $V_{CPD}$  curves measured on different locations are found to be similar in dark, while  $V_{CPD}$  significantly shifts down around  $0.13 \text{ V}$  under illumination. The effective electric field ( $E_{field}'$ ) is calculated as a derivative of  $V_{CPD}$  in the static case, as shown in Figure 3:11, to find out the location of the  $p$ - $n$  junctions<sup>128</sup>. Two electric fields with the same direction and one electric field with a reverse direction are found, referring to three junctions. It was expected an electric field with a unique direction from the surface to the bulk, similar to the report of SSCs<sup>128</sup>. The



reverse electric field of the junction 3 is unexpected in the present work. With an opposite electric field, the junction 3 is harmful for the hole collection, if SSCs were doped with the same diffusion procedures and had the same device structure near the hole collector.

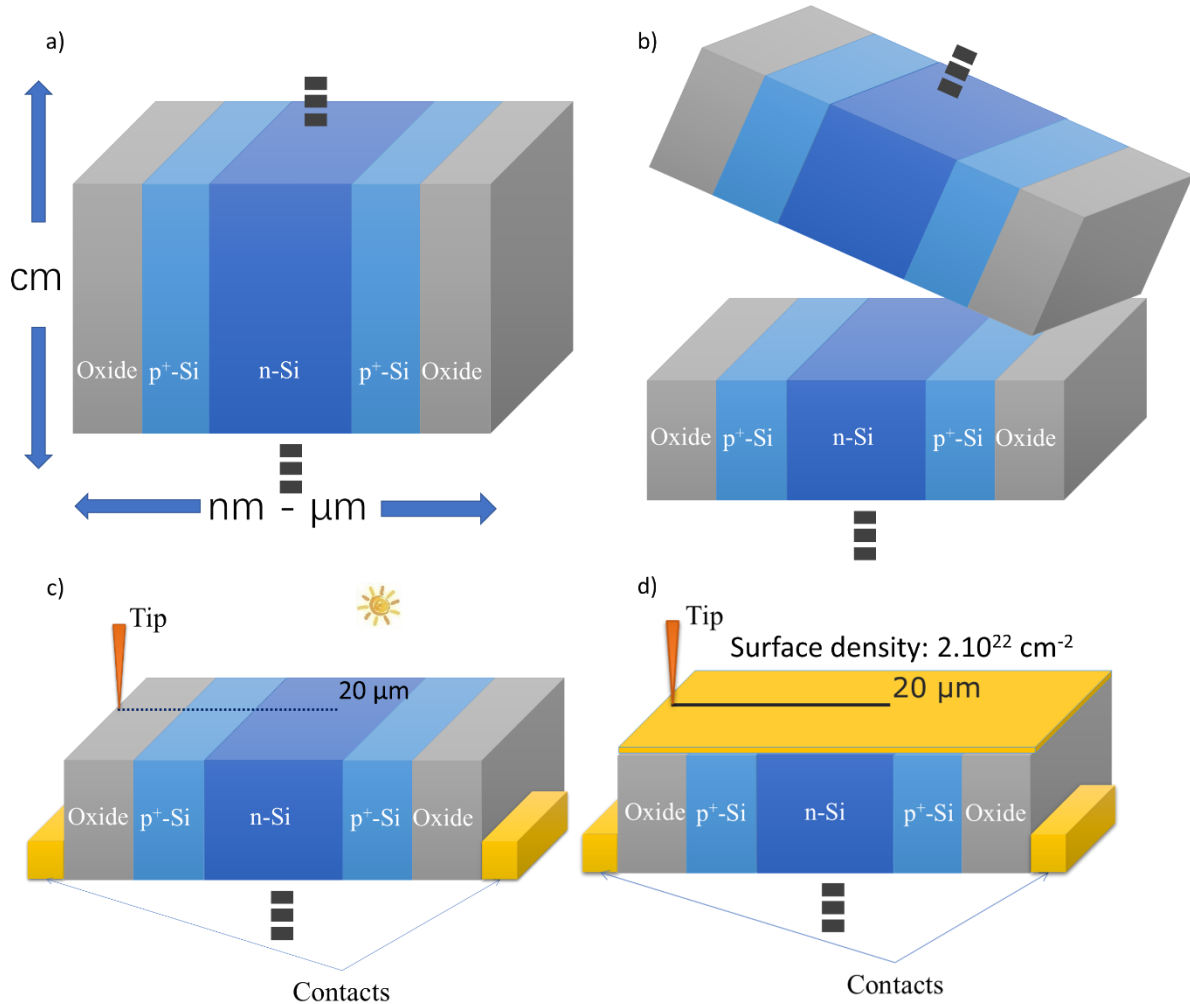


Figure 3:9 Schematic representation of the silicon layer.

Silicon wafer a) before and b) after the cleavage. The thickness of the sample is much thinner in comparison to the surface area. The silicon structure analysed by KPFM is illustrated c) without and d) with surface states. The scan begins at the interface between the contact and the oxide layer on the left, then goes along the cleaved cross section until 20  $\mu\text{m}$  depth.  $p^+$  and  $n$  indicate heavily p-doped and lightly n-doped regions, respectively. Oxide is short for the silicon oxide. Two contacts are connected to the ground.



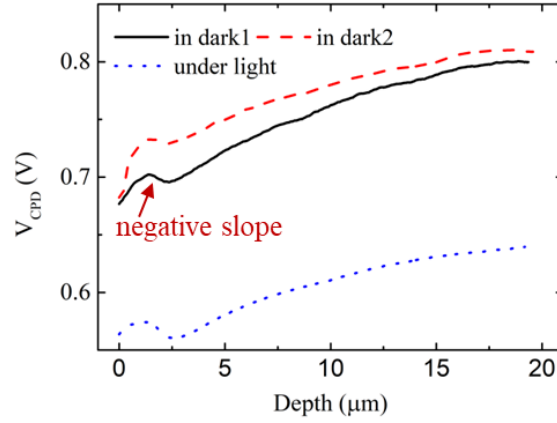


Figure 3:10  $V_{CPD}$  along the cross section of the silicon wafer  
dark1 and dark2 are referring to measurements on two different regions of the same silicon wafer in the dark. The negative slopes refer to the junction 3 in Figure 3:11, and black one of them is indicated by the arrow, for example.

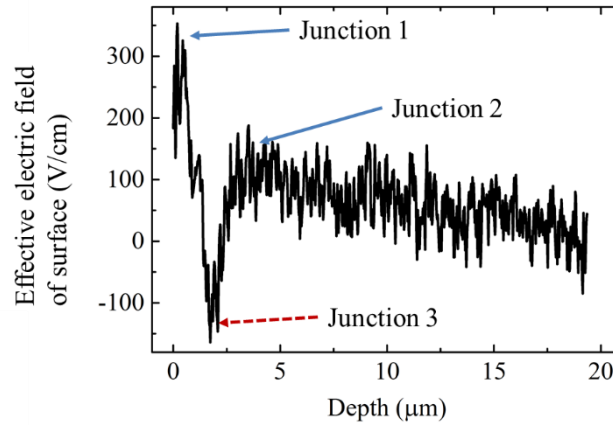


Figure 3:11 Effective electric field extracted as a derivative of the  $V_{CPD}$  in the dark.  
Two junctions have the electric fields with the same direction (indicated by solid blue arrows). One junction has an opposite electric field (indicated by dash red arrow).

### 3.3.3 Preliminary discussion

To perform a first analysis of the KPFM experimental data, two hypotheses of the doping profiles inside the silicon wafer are introduced (Figure 3:12). The hypothesis 1 assumes that the density of acceptors has a steep decrease from the surface to the bulk, while the hypothesis 2 arbitrarily introduces a smoother decrease. Then, the  $V_{CPD}$  is computed along the cross section (Figure 3:13), using the approach in section 3.2.2. The modelled tip WF is set as 5.05 eV to be consistent with the practical situation.



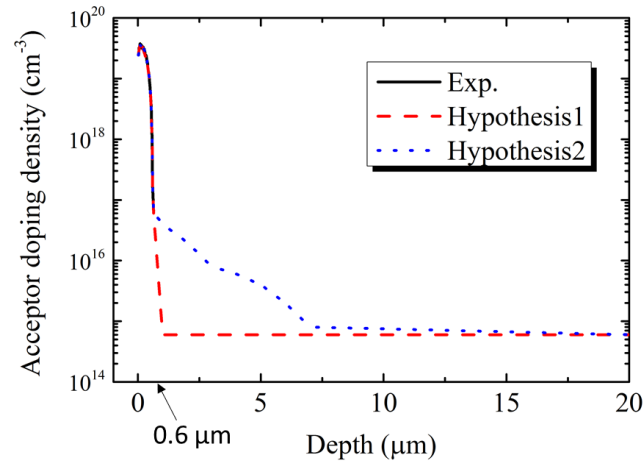


Figure 3:12 The C-V measured and the assumed doping profiles. The hypothesis 1 for the doping profile assumes that the density of acceptors has a steep decrease, while the hypothesis 2 introduces a smoother decrease.

The computation related to hypothesis 1 without surface states is drawn as the red dot line in Figure 3:13 a). A large difference of  $V_{CPD}$  is found near the surface. The experimental  $V_{CPD}$  fall is 0.13 V and that of the simulation is 0.8 V, indicated by the open arrow. The simulated  $V_{CPD}$  then becomes like the experimental one as presented on Figure 3:13 b), considering the surface states on the cross section of the silicon layer. It is necessary to consider a uniform surface density of  $2 \cdot 10^{22} \text{ cm}^{-2}$  of surface states confined in a 2 nm-thick layer at the surface (Figure 3:9 d). The surface states are assumed to be the deep traps, and they favor rather carrier capture than carrier emission. However, the very high surface states density considered here for the computation deserves further investigations in the future. The influence of surface states on the  $V_{CPD}$  profile is found to be limited in the lightly doped silicon region, in comparison to that in the heavily doped region. As a result, few carriers are caught near the lightly doped region and few traps are ionized; plenty of holes are captured near the heavily doped silicon, where the traps become positively ionized, neutralizing the negative acceptors nearby. As shown as the blue dot line in Figure 3:13 b), the depletion width is extended and close to the experiment after introducing the doping profile of the hypothesis 2. Thus, rather than surface states, the shape of the doping profile appears to be the main reason leading to a wider depletion region and the unexpected negative slope of the  $V_{CPD}$  curve. To confirm this hypothesis, analyzing the deeper doping profile from C-V measurements or other techniques might be interesting. Additionally, the light-induced variation of the  $V_{CPD}$  curves agrees between the experiments and simulations (Figure S3). The light source in the simulation is set as a laser source with a wave-



length of 448 nm and an output power of 1 W/cm<sup>2</sup>. More investigations are necessary with realistic illumination conditions.

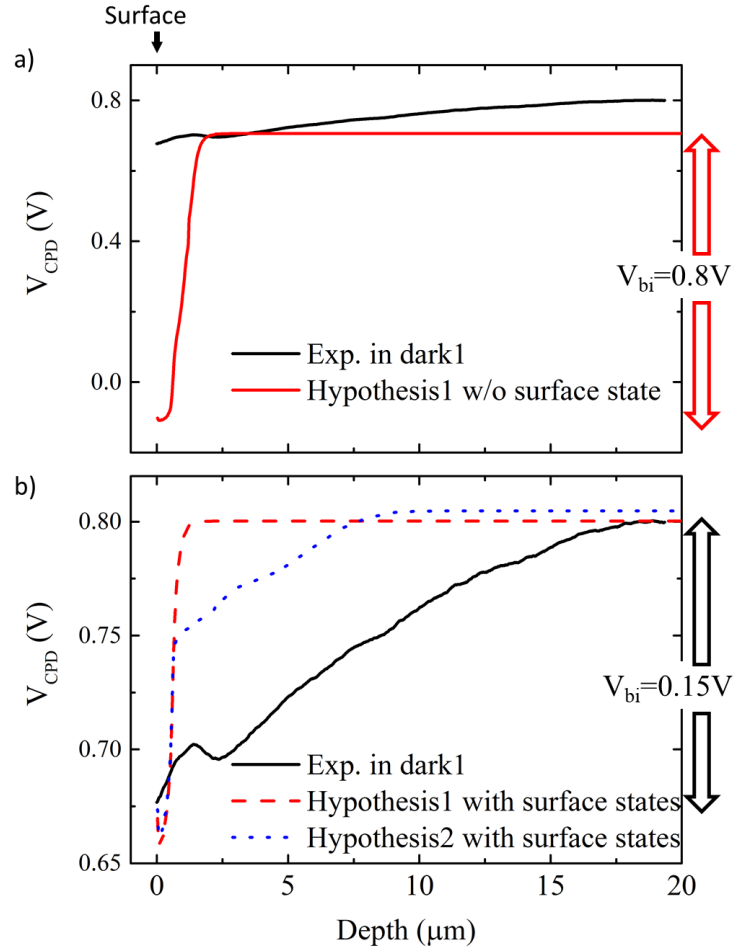


Figure 3:13 Experimental and simulated  $V_{CPD}$  in the dark and under illumination. The scanning is performed from the surface of the oxide layer (pointed by the arrow) down to 20  $\mu m$  depth of the silicon wafer. The experimental  $V_{bi}$  in comparison with the simulation a) without and b) with the surface states. The  $V_{bi}$  differences are indicated by the open arrows.



## 3.4 C-V and KPFM on meso-porous HTM-free PSCs

Collaboration with L. Etgar and S. Aharon (Hebrew University of Jerusalem, Israel)

### 3.4.1 Introduction

ZnO nanorods<sup>130</sup> or phenyl-C61-butyric acid methyl ester (PCBM)<sup>131,132</sup> ETM are able to minimize the band offset at the conduction band minimum (CBM) and allow building almost ideal contacts at the ETM/LHM interface. However, HTM very often present large band offset at the VBM and low carrier mobilities<sup>133–136</sup>. Alternatively, PSCs without an HTM layer were put forward as a solution towards high efficiency. Etgar and coworkers early directly deposited gold on MAPbI<sub>3</sub> and demonstrated that the MAPbI<sub>3</sub> material can be simultaneously used as a light harvester and a hole conductor<sup>137</sup>, leading to PCE of 8%. Then porous carbon film was used<sup>138</sup> as a contact for fully printable HTM-free PSCs with efficiency of 12.8%, and PSCs with single-walled carbon nanotubes<sup>139,140</sup> as a hole collector achieved efficiency of 15%. In such a case, solar cells benefit from fewer interfaces, and, the optical and electrical losses in the HTM layer are removed as well. In Figure 3:14, the architecture of an HTM-free MAPbI<sub>3</sub> PSC is schematically represented by comparison to that of a classical PSC. Gold for example, is directly connected with MAPbI<sub>3</sub> as a hole collection electrode and a Schottky contact is formed<sup>141</sup>.

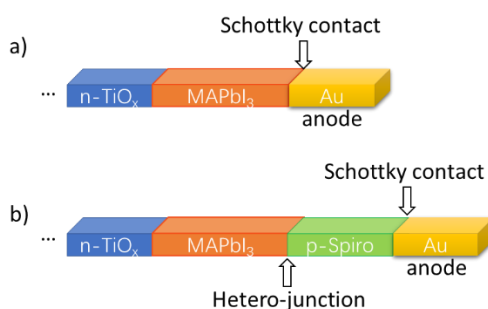


Figure 3:14 Schematic representations of HTM-free and classic PSCs

a) an HTM-free PSC with a Schottky contact between MAPbI<sub>3</sub> and Au, b) a classic PSC with a Schottky contact between HTM and Au. Spiro is short for Spiro-OMeTAD.

In the following subsections, numerical models are built to reproduce the basic J-V and C-V characteristics of TiO<sub>x</sub>/MAPbI<sub>3</sub>/Au solar cells. The comparison of built-in potential measured by C-V and KPFM are discussed in the end.



### 3.4.2 Basic properties of HTM-free PSCs

A basic modeling of HTM-free PSCs experimentally studied by Etgar's group<sup>27</sup>, relies on the  $\text{TiO}_x/\text{MAPbI}_3/\text{Au}$  architecture. ETM anatase  $\text{TiO}_x$ <sup>105,109,142</sup> is heavily n-type doped ( $10^{19} \text{ cm}^{-3}$ ). The doping type of  $\text{MAPbI}_3$ <sup>71,143,144</sup> is fit as a n-type layer ( $4 \cdot 10^{16}$ ) or p-type layer ( $8 \cdot 10^{16} \text{ cm}^{-3}$ ), which will be mentioned in section 3.4.3. The thicknesses of  $\text{TiO}_x$  and  $\text{MAPbI}_3$  layers are both equal to 300 nm. The WF of gold<sup>141,145</sup> is 5.1 eV. Ohmic contact is considered on the left of the  $\text{TiO}_x$  layer. The properties of the materials used for the simulation are summarized in Table S1. Figure 3:15 presents the band alignment under thermal equilibrium and short circuit condition, based on the simplified architecture. The Fermi-level ( $E_f$ ) remains constant as a reference through the device, and the band offsets at each interface yield two potential barriers on two band edges. It is shown that the major potential drop is in the  $\text{MAPbI}_3$  layer. Therefore, the major part of the electrical current is assumed to originate from carrier drifting rather than carrier diffusion.

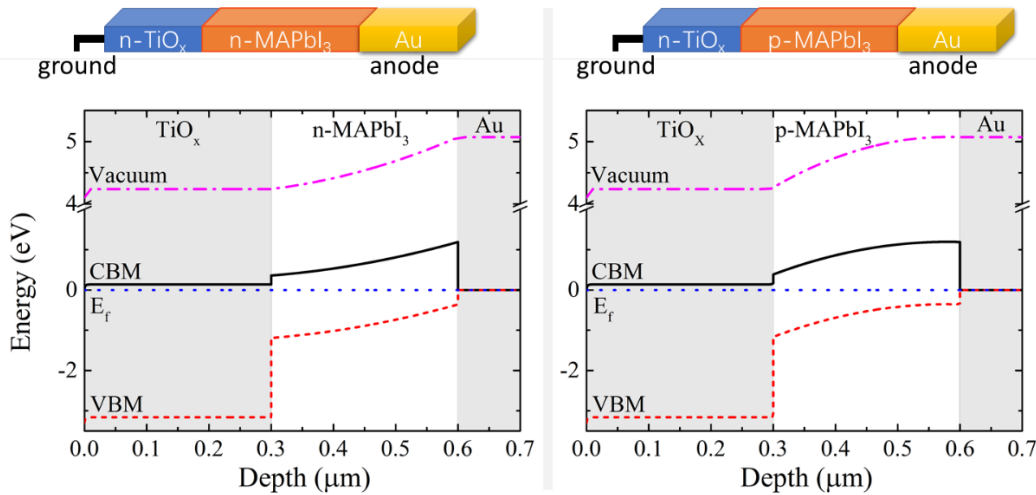


Figure 3:15 Real and modeled architectures along with the static band diagram of left) n-doped and right) p-doped  $\text{MAPbI}_3$  based HTM-free PSCs.

### 3.4.3 Capacitance characteristics

In order to obtain efficient energy conversion in solar cells with low mobility absorbers, a high built-in potential ( $V_{bi}$ ) is necessary in order to prevent significant losses due to carrier recombination processes competing with charge extraction processes<sup>146</sup>. Due to the Schottky contact<sup>147</sup> formed at the  $\text{MAPbI}_3/\text{Au}$  interface (Figure 3:14), the  $V_{bi}$  can be extracted from a well-known Mott-Schottky capacitance analysis. The capacitance expression is given by:



$$\frac{1}{C^2} = f\left(V_{bi} - V_b + \frac{k_B T}{q}\right)$$

Equation 3–2 Capacitance-voltage expression

where  $C$  is the junction capacitance and is  $f$  a linear function. The circuit for C-V measurements and the device architecture in the modelling are illustrated in Figure 3:16. A small signal analysis<sup>148</sup> is used to simulate C-V characteristics of the HTM-free MAPbI<sub>3</sub> PSCs. The signal frequency is fixed at 1 kHz for the simulation, as in the practical case. Compared to the available experimental data<sup>27</sup>, the C-V theoretical characteristics is presented in Figure 3:17. As the bias reversely increases, the extension of the depletion region starts at the MAPbI<sub>3</sub>/Au interface, then goes through the MAPbI<sub>3</sub> and finally into the TiO<sub>x</sub>. Because of the different doping level and  $\epsilon_r$  values in MAPbI<sub>3</sub> and TiO<sub>x</sub> layer, the C-V curves under reverse bias are bent into two stages. Similar phenomena were observed for III-V semiconductors<sup>149,150</sup>. The roughly constant capacitance at stage II is due to the heavy doping level in TiO<sub>x</sub>, while the slope in stage I is related to the light doping level in MAPbI<sub>3</sub>. The doping level of MAPbI<sub>3</sub> is fitted to the slope of the C-V curve. The point A on Figure 3:17 corresponds to the transition point of the depletion region from stage I to stage II. The fluctuations of experimental data at stage II could be explained by non-uniform doping in the TiO<sub>x</sub> layer. Because of the huge effective surface area of nano-porous TiO<sub>x</sub><sup>151–153</sup> and the rough surface of MAPbI<sub>3</sub> layer<sup>153</sup>, it is difficult to directly extract the precise doping level,  $\epsilon_r$  or layer thickness of MAPbI<sub>3</sub> or junction area from the classic parallel plate capacitance Equation 3–3. In the model, the effective junction area of capacitance interface is indeed theoretically found equal to two times the active area of the gold electrode. If a uniform growth of material layers could be achieved in the future, it would be possible to extract more quantitative informations from the C-V measurements, related to the doping level,  $\epsilon_r$ , junction area or layer thickness of the MAPbI<sub>3</sub> layer.

According to Equation 3–2, the  $V_{bi}$  of the MAPbI<sub>3</sub> layer can be extracted from the intersection with the horizontal x-axis. The experimental  $V_{bi}$  is 0.6 V from C-V analysis. However, the theoretical  $V_{bi}$  is generally expected to be 0.9 V. The porosity<sup>151</sup> of meso-porous TiO<sub>x</sub> is around 50%. According to the previous modelling, the doping level of TiO<sub>x</sub> is supposed to be large ( $10^{19}\text{cm}^{-3}$ ). If half of the TiO<sub>x</sub> volume is replaced by MAPbI<sub>3</sub> with a low doping level, the net doping level within the meso-porous TiO<sub>x</sub> might be around  $5.10^{18}\text{cm}^{-3}$  corresponding to WF of 4.2eV. Then the theoretical poten-



tial drop between Au and  $\text{TiO}_x$  should be equal to the difference of their  $\text{WF}/q$ , as  $(5.1-4.2\text{eV})/q = 0.9\text{ V}$ .

To numerically fit the experimental  $V_{\text{bi}}$ , an effective interfacial layer (IF) was introduced into the architecture for each type of  $\text{MAPbI}_3$ . In n-doped  $\text{MAPbI}_3$ , the IF of 8.5 nm is heavily n-doped and located between Au and  $\text{MAPbI}_3$  (Figure 3:16 b)). In p-doped  $\text{MAPbI}_3$ , the IF of 3.4 nm is heavily p-doped and located between  $\text{TiO}_x$  and  $\text{MAPbI}_3$  (Figure 3:16 c)). The doping level of each IF is set equal to  $2 \cdot 10^{19}\text{ cm}^{-3}$ . Such a high density of charges in the IF leads to a reduction of the  $V_{\text{bi}}$  from 0.9 to 0.6 V, in good agreement with the experimental value (Figure 3:17). The influence of IF is furthermore discussed in the following sections, in comparison with J-V characteristics and KPFM measurements.

$$C = \frac{\epsilon_r \epsilon_0 A_{\text{eff}}}{d}$$

Equation 3–3 Classic parallel plate capacitance expression

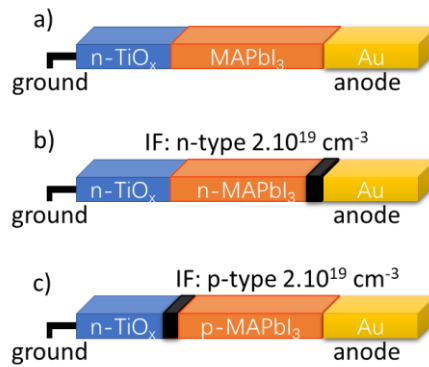


Figure 3:16 Circuit and architectures used for C-V and J-V characteristic. a) is a classic architecture, while structures on b) and c) have IF (thin black layer) at the  $\text{MAPbI}_3/\text{Au}$  interface and the  $\text{TiO}_x/\text{MAPbI}_3$  interface, respectively.



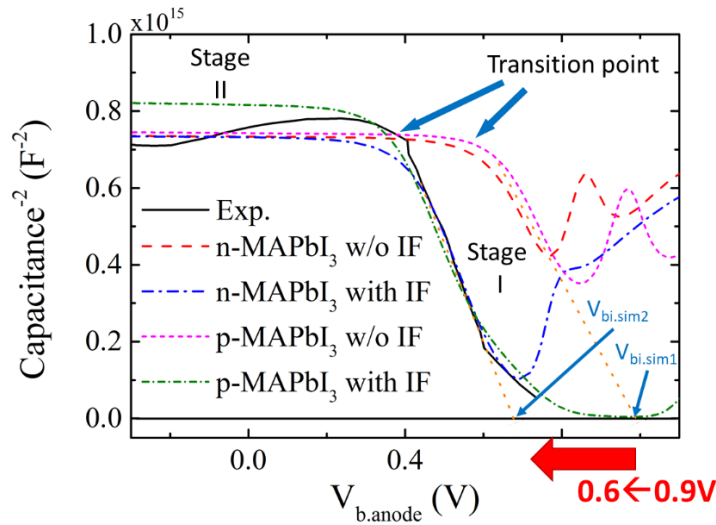


Figure 3:17 The computed and experimental (solid line) C-V characteristics. n-doped MAPbI<sub>3</sub> with (without) a n-doped IF at Au/MAPbI<sub>3</sub> interface is indicated as dash dot (dash) line. p-doped MAPbI<sub>3</sub> with (without) a p-doped IF at TiOx/MAPbI<sub>3</sub> interface is indicated as a short dash dot (short dash) line. The  $V_{bi}$  values are extracted from the intersections with the x-axis.

#### 3.4.4 Photovoltaic characteristics

In Figure 3:18, the simulated J-V characteristics under one sun illumination of AM1.5 are presented along with experimental data. A good matching to the experimental J-V curve is obtained assuming n-type MAPbI<sub>3</sub> with doping level based on the fitting of C-V characteristics. Therefore, the present work will now only discuss n-doped MAPbI<sub>3</sub> based HTM-free PSCs.

Based on the comparison of the experimental and the computed C-V characteristics (Figure 3:17), it is necessary to assume that a heavily n-doped IF exists at the MAPbI<sub>3</sub>/Au contact. Alternative hypotheses with layers containing acceptors or surface states, were explored but without success. Indirect evidence of the existence of such an IF can be found in the report of Liu's group<sup>141</sup>. Using ultraviolet photoemission spectroscopy (UPS), the authors indeed showed that during the deposition of the gold contact, the Fermi level undergoes a progressive shift. Noteworthy, the presence of metal nano particles<sup>154</sup> or charged ions<sup>155–157</sup> at the interface was discussed by other groups. This Fermi level shift is simulated in the present work by introducing an effective and heavily n-doped MAPbI<sub>3</sub>-based IF at MAPbI<sub>3</sub>/Au interface. The static band alignment and the potential profile with and without IF are computed and represented in Figure 3:19 a) and b), to have an insight into the device operation. Even though the band offset on the top of MAPbI<sub>3</sub> is pinned by the gold contact, the ef-



fective potential drop across the MAPbI<sub>3</sub> layer is lowered due to the presence of the IF. Therefore, the losses of PSCs due to carrier recombination processes increase and the efficiency decreases from 11% to 8% (Figure 3:18). Thus, a thick IF is assumed to have a detrimental effect on the photovoltaic performance. Furthermore, an investigation of the potential in the structure is performed by using KPFM on the same cell structure in the next section.

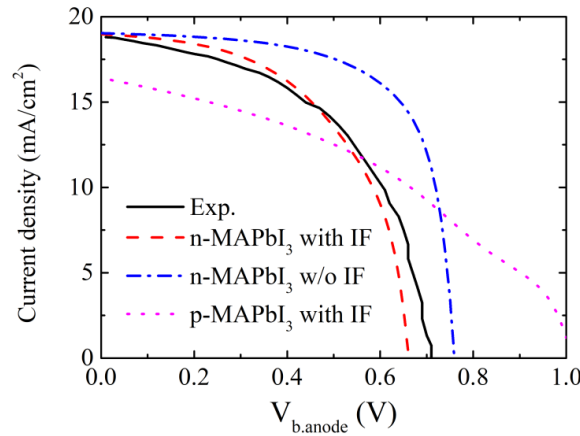


Figure 3:18 Experimental and simulated J-V characteristics under one sun illumination of n-doped MAPbI<sub>3</sub> based HTM-free PSCs with (dash line) and without (dash dot line) IFs.

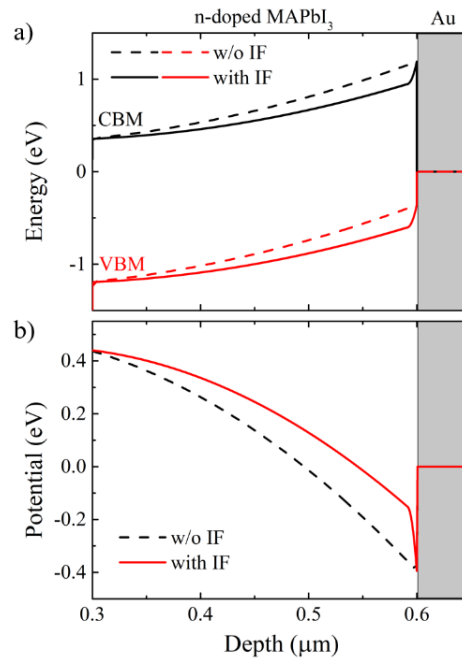


Figure 3:19 a) Static band alignments and b) potential profiles with and without IF. The IF-induced potential variation is observed near the Au contact.



### 3.4.5 Preliminary discussion of $V_{CPD}$ along the cross section of HTM-free PSCs

Samples of  $TiO_x/MAPI_3/Au$  HTM-free structure were deposited on a silicon substrate and then cleaved for the KPFM measurements, to probe the potential profile along the cross section. First, the phase mapping is used to distinguish different regions (Figure 3:20 a). The  $Au/MAPI_3$  interface is found to be smoother than the  $TiO_x/MAPI_3$  interface. And the freckle pattern in the  $TiO_x$  layer indicates an existence of pores filled with  $MAPI_3$ . As shown in Figure 3:20 b), the variation of the  $V_{CPD}$  within the meso-porous layer is weak (around 0.05 V) close to the resolution of the KPFM set-up, while the variation through the whole  $MAPI_3$  layer is larger (around 0.2 V). It indicates that the doping level of the meso-porous layer is heavy, and the doping level of  $MAPI_3$  is light. The depletion region in such architecture is found to be 300 nm, over the whole  $MAPI_3$  layer. An unexpected  $V_{CPD}$  variation within the Au near the Schottky contact is observed under illumination, which might be alternatively due to a displacement of the sample holder. No photovoltaic effect is expected in the Au conductor.

The variation of the experimental  $V_{CPD}$  profile (the surface  $V_{bi}$ ) in the dark is 0.4 V (Figure 3:20 b), smaller than the  $V_{bi}$  deduced from C-V analysis. The gold is unaffected by surface states, while the increase of the  $TiO_x$  WF could be related to the influence of surface states (section 3.2.4), leading to a smaller surface  $V_{bi}$ .

Under illumination, a downshift of the  $V_{CPD}$  profile is mainly observed in the meso-porous region and the  $MAPI_3$  nearby. According to the previous modelling (section 3.2.5), this SPV effect might be due to the interaction between the surface states and the electron accumulation. The unexpected heavily n-doped IF (section 3.4.3) and the VBM discontinuity at  $Au/MAPI_3$  interface might lead to an accumulation of holes. However, this effect is not so visible in this KPFM measurement. Without carrier accumulation under illumination, the  $V_{CPD}$  profiles are expected to be the same as that in the dark<sup>70</sup>. Nevertheless, an advanced modelling is needed to perform better simulations of meso-porous structures, to reproduce and interpret KPFM measurements.



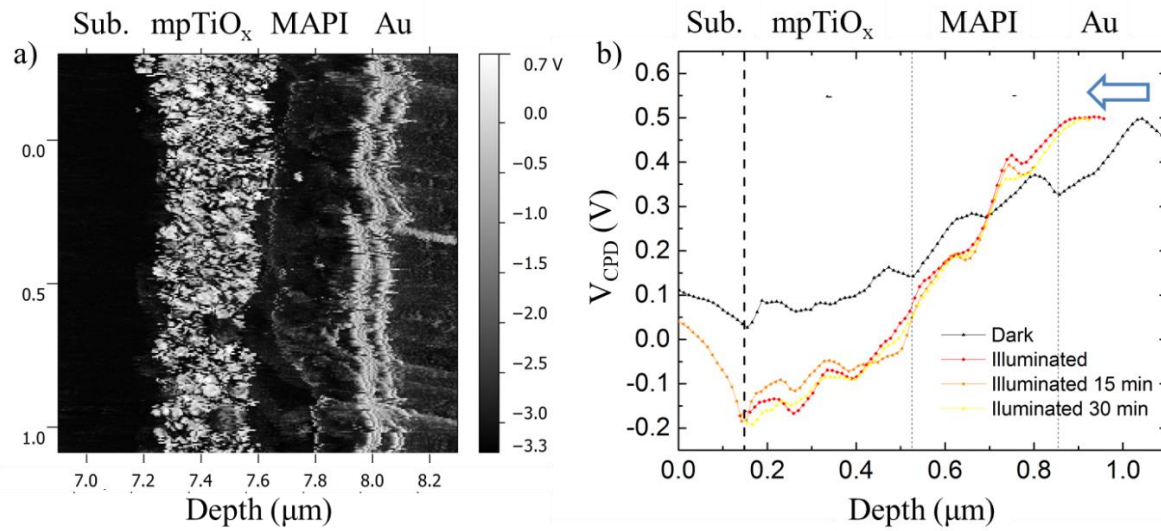


Figure 3:20 a) Phase mapping and b)  $V_{CPD}$  profile on the cross section of  $TiO_x/MAPbI_3/Au$  structure. Sub. is short for silicon substrate, mpTiO<sub>x</sub> is meso-porous TiO<sub>x</sub>. MAPI is MAPbI<sub>3</sub>. The open arrow in the Au region of figure b) indicates a displacement of the sample holder.

### 3.5 Summary

The depletion region width is sometimes a qualitative one for C-V measurements in the case of a rough junction, while it can be a quantitative property for KPFM measurements.  $V_{bi}$  is a quantitative property from C-V measurements, while it is generally a qualitative one from KPFM measurements when surface states are important. The doping level in the depletion region can be deduced from C-V measurements for 1D structures. From a combination of C-V, KPFM measurements and modelling, the doping profile of multi-dimensional structures is supposed to be accessible.







## Chapter 4 Investigation of PSCs

### 4.1 $\text{TiO}_x$ and $\text{WO}_x$ based PSCs

Collaboration with A. Gheno, S. Vedraïne and J. Bouclé (XLIM laboratory, Limoges)

#### 4.1.1 Introduction to flexible and printable PSCs

Nowadays most photovoltaic (PV) research and development activities are dedicated to bulky silicon solar cells,<sup>158</sup> while economical and flexible PV devices are desirable for future integration into mobile electronic productions, or inside and outside buildings. Many types of materials for flexible solar cells have been considered, such as polythiophenes organic semiconductors<sup>159</sup>, ruthenium-based polypyridines<sup>160,161</sup>, semiconductors with a chalcogen element (sulfur, selenium or tellurium)<sup>162</sup> or halide perovskites<sup>163</sup>. At 130°C without any post-treatments, a solution-derived  $\text{NiO}_x$  film was deposited by Xingtian Yin et al<sup>164</sup> as a HTM, leading to a flexible PSCs with PCE of 16.47%. Dong Yang et al<sup>165</sup> proposed to use solid-state ionic-liquids as ETM after annealing at 70°C for 10 min and obtain a PCE of 16.09%. Moreover Ma's group<sup>166</sup> introduced Nb-doped  $\text{WO}_x$  (ETM) processed at 120°C to obtain flexible PSCs with PCE of 15.65% in 2016, while the nanostructured  $\text{WO}_x$  was firstly employed as ETM in PSCs by Mahmood et al two years ago<sup>167</sup>. Recently, A. Gheno and his colleagues from XLIM<sup>168</sup> were successful in making printed  $\text{WO}_x$  PSCs with PCE > 10%. Now most PSCs suffer from  $V_{OC}$  losses, and  $\text{WO}_x$  based ones are not an exception. In this section,  $\text{WO}_x$  are deposited using spin coating technology under different temperatures to study the surface influence of  $\text{WO}_x$  on the PSC performance.

#### 4.1.2 Experiments and characterizations of $\text{WO}_x$ PSCs

Eight pieces of a transparent glass with a layer of conductive Indium Tin Oxide (ITO) on the top were prepared as substrates.  $\text{WO}_x$  was used as an ETM in a n-i-p configuration;  $\text{WO}_x$  nanoparticle 2-isopropanol solution (Nanograde, product P-10) was spincoated directly on ITO. The samples were divided into two groups and separately annealed at 110°C and 80°C during 10 min. The



group with the annealing temperature of 110°C are the control, referring to the previous report<sup>102</sup>. One of the four samples in each group was dedicated to surface WF measurement by KPFM, while the MAPbI<sub>3-x</sub>Cl<sub>x</sub> perovskite was deposited using a one-step deposition procedure on top of the rest samples. The perovskite was prepared with 40 wt% of PbCl<sub>2</sub> and MAI (molar ratio = 1:3), 59 wt% of DMF and 1% of diiodooctane. Finally, spiro-OMeTAD (HTM) was deposited on top of the perovskite layer, before a thermal evaporation of a 100 nm thick gold electrode. The HTM layer is made from a precursor solution containing Spiro-OMeTAD (73.2 mg, from Sigma-Aldrich), 4-tert-Butylpyridine (28.8 µl, from Sigma-Aldrich) and Bis(trifluoromethane)sulfonamide lithium salt solution (17.5 µl, previously diluted at 530 mg/ml in acetonitrile, from Sigma-Aldrich) in chlorobenzene (1 ml). Schematic procedures are illustrated in Figure 4:1, along with the real WO<sub>x</sub> based PSC. HD-KPFM measurements<sup>102</sup> were performed on the surface of the WO<sub>x</sub> slabs. During the J-V characterization<sup>102</sup>, the sweeping speed was set to 0.25 mV/ms, with a precondition stage under 1.5 V bias and one-sun illumination for 20 s.

Along with the surface WF of the WO<sub>x</sub> layers, the performance of the cells under illumination are presented in Figure 4:2, including V<sub>OC</sub>, J<sub>SC</sub>, the efficiency and FF. The middle of the error bar is the mean value. The data in the dash frames refer to the samples with WO<sub>x</sub> annealed at 80°C. The data obtained during forward scans are presented in black color (left), while data characterized during backward scans are presented in red (right). A considerable improvement is observed, if the annealing temperature of WO<sub>x</sub> layer decreases from 110 to 80°C. The V<sub>OC</sub> increases, the J<sub>SC</sub> increases, the efficiency increases and the FF increases. The surface WF of WO<sub>x</sub> also decreases from 4.93 to 4.74 eV. In the following sections, a theoretical modelling is proposed for TiO<sub>x</sub> and WO<sub>x</sub> based PSCs, to interpret the V<sub>OC</sub> loss and the PCE enhancement induced by the WO<sub>x</sub> surface modification.



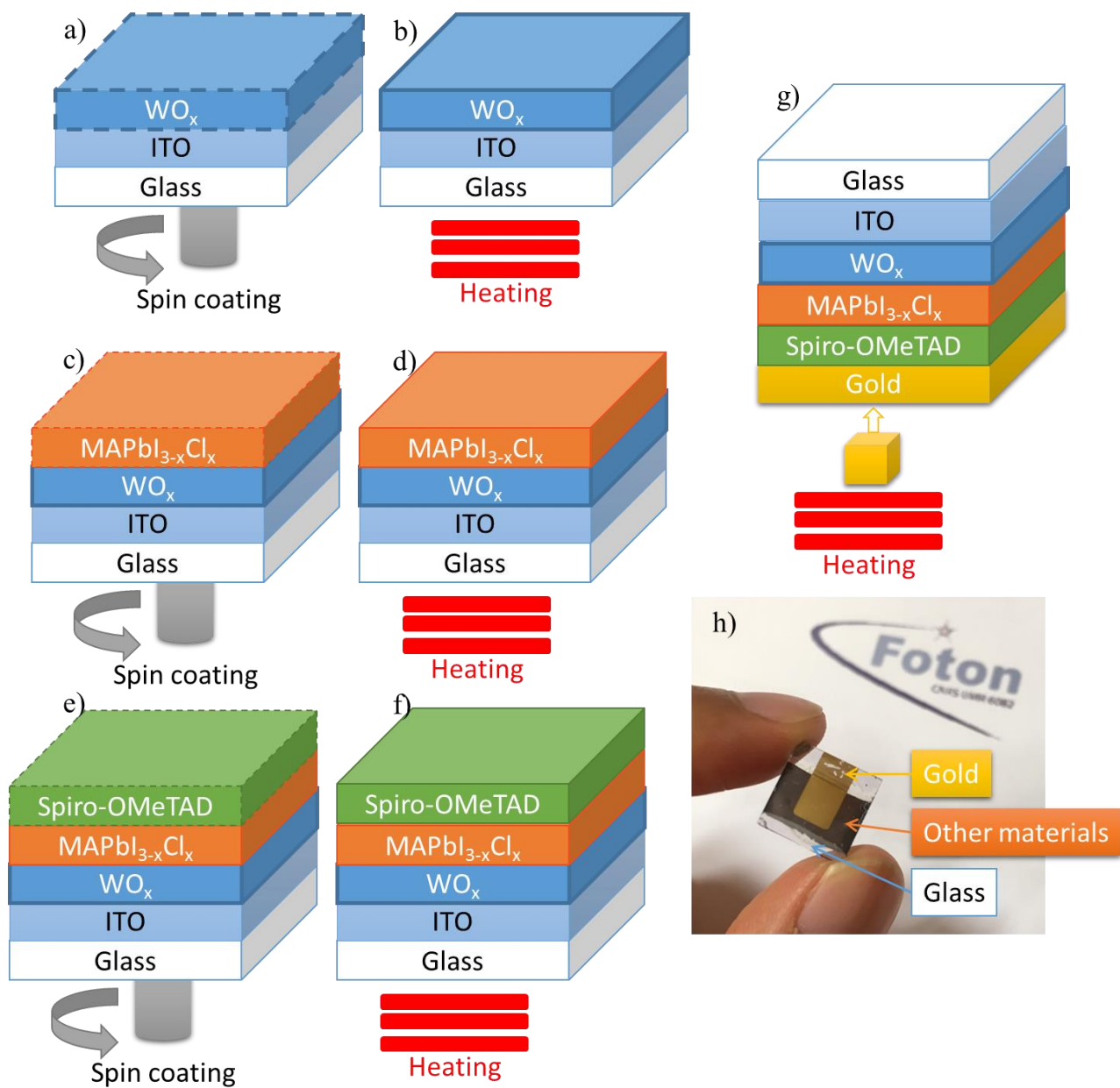


Figure 4:1 a-g) Schematic procedures of WO<sub>x</sub> based PSC fabrication and h) a real device



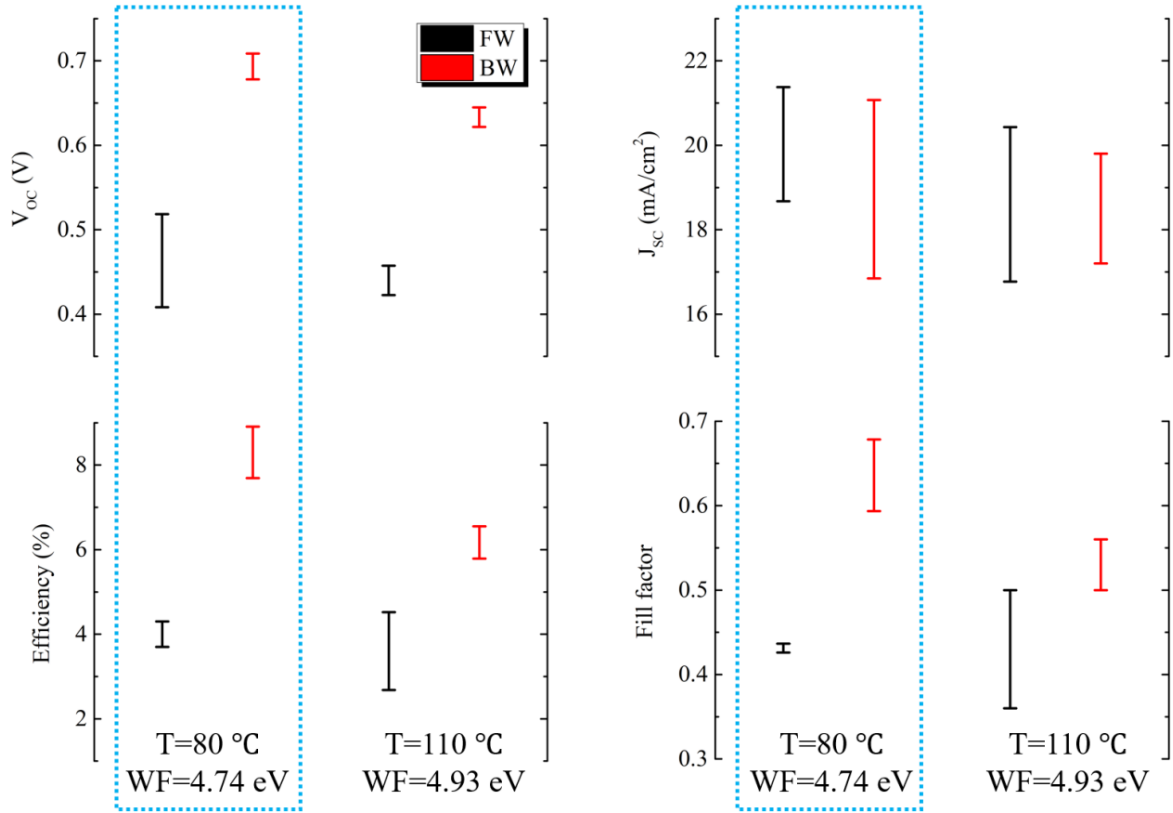


Figure 4:2 Statistics of the performance of PSCs  
 $WO_x$  is deposited under different annealing temperatures. Left (right) column refers to annealing temperature of 80 (110) °C and the related surface WF of  $WO_x$  layer is 4.74 (4.93) eV. Characteristics under forward (backward) sweeping are black (red).

#### 4.1.3 Experimental comparison between $WO_x$ based and classic $TiO_x$ based PSCs

Printable  $WO_x$  based and classic  $TiO_x$  based PSCs were prepared and characterized by A. Gheno and his colleagues<sup>102</sup> for comparison purposes. Same growth procedures are used after the deposition of the oxide ETM layers. It results in a significant difference of the perovskite quality and photovoltaic properties of the devices. The carrier lifetimes  $\tau$  in  $MAPbI_{3-x}Cl_x$  measured by Time-Resolved PhotoLuminescence (TRPL) are 10 and 16 ns on the top of  $WO_x$  and  $TiO_x$ , respectively. The  $V_{OC}$  of the  $WO_x$  based PSC is 0.1 V smaller than that of the  $TiO_x$  based PSC. The difference of the cell performances is discussed in the next sections along with the numerical modelling.



#### 4.1.4 Modelling of $\text{TiO}_x/\text{MAPbI}_3/\text{Spiro-OMeTAD}$ cells

The structure considered for modelling<sup>65</sup> is shown in Figure 4:3. Ohmic contacts are directly set on both sides without considering the metal/semiconductor interfaces to save computational resources. The cathode is grounded, while the anode is biased. The experimental porosity of the meso-porous  $\text{TiO}_x$  layer is 45% as determined by ellipsometry, and its thickness is about 300nm. To enable one-dimensional modelling, the meso-porous  $\text{TiO}_x$  layer was simply replaced by two compact layers in the simulation. One with pure  $\text{TiO}_x$  and the second with pure  $\text{MAPbI}_3$ . The thickness of the effective compact  $\text{TiO}_x$  layer was 165nm, while the remaining volume of the meso-porous layer (133nm) was supposed to be filled with  $\text{MAPbI}_3$ , leading to a total thickness of the effective  $\text{MAPbI}_3$  layer as 335nm. As before (section 3.2.5), the bulk properties of  $\text{MAPbI}_3$  are used for  $\text{MAPbI}_{3-x}\text{Cl}_x$ . The properties of the materials are summarized in Table S1. The related static band alignment with a constant Fermi level ( $E_f$ ) is illustrated on Figure 4:3 b), along with the vacuum level as a sum of the electron affinity and the CBM. Due to the high doping level, the CBM of  $\text{TiO}_x$  and the VBM of Spiro-OMeTAD are close to  $E_f$ . A large built-in potential  $V_{bi}$  is found in the non-intentionally doped  $\text{MAPbI}_3$  layer. A uniform electric field ( $\vec{E}$ ) is generated inside  $\text{MAPbI}_3$  (Figure 4:3 c)) according to the Equation 2–5. As a result, electrons and holes are driven to the opposite collectors.

Trap centers lying at about 0.6 eV above the VBM have been suggested<sup>120</sup> to exist in  $\text{MAPbI}_3$  with a density  $N_t$  roughly equal to  $10^{16} \text{ cm}^{-3}$ , leading to a carrier lifetime ( $\tau$ ) of about 100 ns for electrons. The  $v_{th}$  of  $\text{MAPbI}_3$  is deduced as  $2.3 \cdot 10^7 \text{ cm/s}$  from the effective mass<sup>169</sup>. Then the SIG of  $\text{MAPbI}_3$  is calculated as  $4.3 \cdot 10^{-17} \text{ cm}^2$ , according to the equation 2-14. A  $\tau$  of 16 ns is observed by TRPL on the  $\text{MAPbI}_3$  layer of the present work<sup>102</sup>. Therefore, a  $N_t$  value of  $6.25 \cdot 10^{16} \text{ cm}^{-3}$  is considered in the TR simulation. Nevertheless, Interface Trap State (ITS) may form at the oxide/perovskite interface<sup>170</sup> due to the oxygen vacancy, according to the density functional theory (DFT). Very short  $\tau$  of few ps is measured at oxide/perovskite interface.<sup>171</sup> In this study, the ITS are simply considered as deep traps with  $E_t = E_i \approx E_g/2$  and short  $\tau$ .



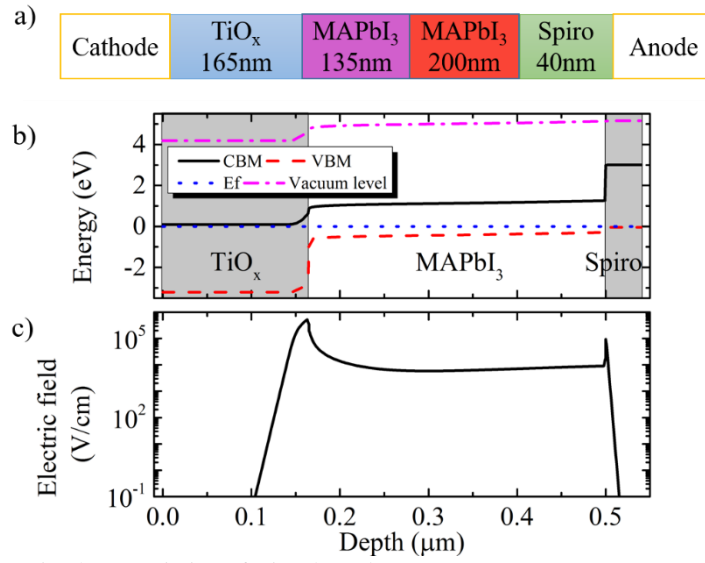


Figure 4:3 Static characteristics of  $\text{TiO}_x$  based PSCs

a) Schematic architecture, b) band alignment and c) static electric field. Spiro is short for Spiro-OMeTAD. The 300 nm mesoporous  $\text{TiO}_x$  layer was replaced by a 165 nm compact layer of  $\text{TiO}_x$  and a 135 nm layer of  $\text{MAPbI}_3$ .

The effects of bimolecular recombinations (BR) and trap-assisted recombinations (TR) on J-V characteristics are illustrated in Figure 4:4. The one sun spectrum we used is AM1.5G (Figure S2). In the ideal case, only radiative BRs are involved, and the computed  $V_{OC}$  equals to 1.1 V. When local bulk traps are additionally induced ( $\tau = 16$  ns),  $V_{OC}$  decrease to 1 V. ITS was further considered at the  $\text{TiO}_x/\text{MAPbI}_3$  interface. It is necessary to have  $\tau$  values as small as 1 ps, to obtain sizeable effects on the  $V_{OC}$  (reduced to 0.95 V) and on the  $J_{SC}$  (becoming less than  $20 \text{ mA/cm}^2$ ). Following the pioneering works and static model of Tress<sup>64</sup>, we propose a dynamical model taking into account the BR and the TR and mobile ions. The aim of this model is to reproduce the hysteresis effect and to understand charge accumulations. We consider negative charged ions with a density of  $3 \cdot 10^{17} \text{ cm}^{-3}$  and a mobility<sup>172,173</sup> of  $4 \cdot 10^{-10} \text{ cm}^2/\text{Vs}$ , while positive ions have opposite characteristics. These ions might be related to defect sites at the Oxide/ $\text{MAPbI}_3$  interface and start to move after lattice relaxation or under built-in electric field. The sweep rate and precondition stage are defined following the literature<sup>102</sup>. The computed J-V curves including mobile ions are shown in Figure 4:4 b) from 0 to 1.2 V and in c) from 0.8 to 1.5 V, along with the experimental data. A good fitting is observed up to high positive biases, where the FW and BW curves come closer. It indicates the formation of a stationnary state. The computed  $V_{OC}$  of forward (FW) and backward (BW) are 0.85 and 0.95 V, respectively; the  $J_{SC}$  shifts back to more than  $20 \text{ mA/cm}^2$ . The difference between experi-



mental and computed  $J_{SC}$  might be due to the somewhat arbitrary thickness of the MAPbI<sub>3</sub> layer, or the crude modelling of the meso-porous layer, or the modelling of ITS. Further investigations will be performed in the future.

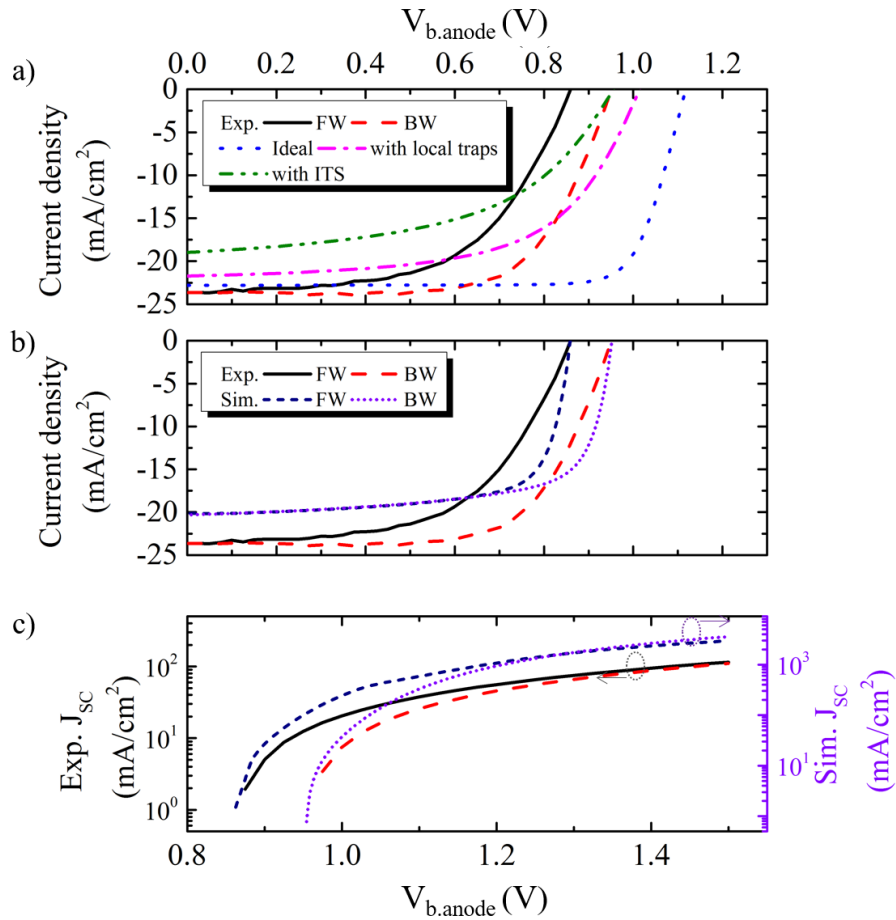


Figure 4:4 Experimental and simulated J-V characteristics of TiO<sub>x</sub> based solar cells.

a) black solid and red dash lines correspond to experimental data under forward and backward scans, respectively. The ideal case with only the BR for the computation is drawn as blue dots. The violet dash dot line corresponds to the local TR, and the case with the ITS corresponds to the green dot dot dash line. b-c) Experiment data compared with a simulation including the BR, TR, ITS and mobile ions. The tick labels for a) and b) are on the top. c) presents the J-V curves in the range from 0.8 to 1.5 V.



Figure 4:5 shows an insight into device operation under no bias and no light or with a bias of 1.5 V under illumination. In the short circuit (Figure 4:5 a), the bias on the anode ( $V_{b,anode}$ ) is smaller than the  $V_{bi}$ , leading to few carriers accumulate in the MAPbI<sub>3</sub>. And negatively-charged ions migrate towards the positively-ionized donors of TiO<sub>x</sub>. When the  $V_{b,anode}$  is larger than  $V_{bi}$ , for example with a bias equal to 1.5 V (Figure 4:5 b), the depletion region disappears and is refilled with photo-generated carriers, and the negative-charged ions migrate towards to the positive biased anode. The ion distribution during FW and BW scans can result in different potential profile under a bias of 0.9 V (Figure 4:6). Before sweeping, the devices are stabilized under 1.5V bias and one-sun illumination for 20 seconds. Then a bias is applied from 0 to 0.9 V (forward scan). Some negative charged ions migrate close to the TiO<sub>x</sub> layer, while the others stay close to the Spiro-OMeTAD. As mentioned in the last section, the negative ions can play the role of acceptors, which can form a p-n junction with n-doped TiO<sub>x</sub>. It leads to potential profile flatter than during the BW scan. This effect can impede the photo-generated electrons transport at TiO<sub>x</sub>/MAPbI<sub>3</sub> interface. A worse situation occurs at the interface, when interface  $\tau$  is very short due to ITS. When the device is biased back from 1.5 to 0.9 V, the  $V_{b,anode}$  dominates and the ions stay near the Spiro-OMeTAD layer. In such a case, MAPbI<sub>3</sub> is p-doped near the hole collector, and the built-in electric field ( $\vec{E}$ ) is enhanced, referring to a steeper potential profile inside the MAPbI<sub>3</sub> layer; the photo-generated carrier collection become more efficient and a larger  $V_{OC}$  is obtained. During the sweeping, the  $\tau$  is constant and controlled by the local trap states, while the  $V_{OC}$  may change because of the interface trap states and ion migration. Thus, the general expression for the equivalent circuit<sup>63,174</sup>, does not seem to be suited to yield a proper description of the hysteresis effect in PSCs. These mobile ions may be halide vacancies or interstitial defects<sup>157,175</sup> or MA cations<sup>54,55</sup>. Based on the Equation 2–20, further investigations on temperature dependent properties of mobile ions would be fruitful.



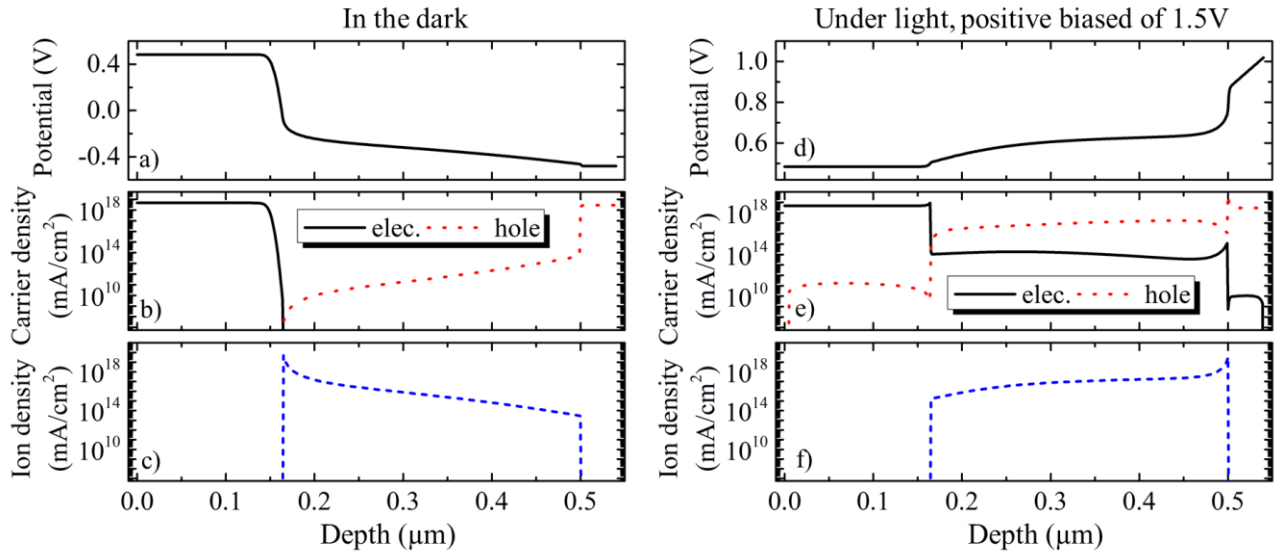


Figure 4:5 Computed potential, carrier and ion distribution in the dark (left) and under one-sun illumination (right).

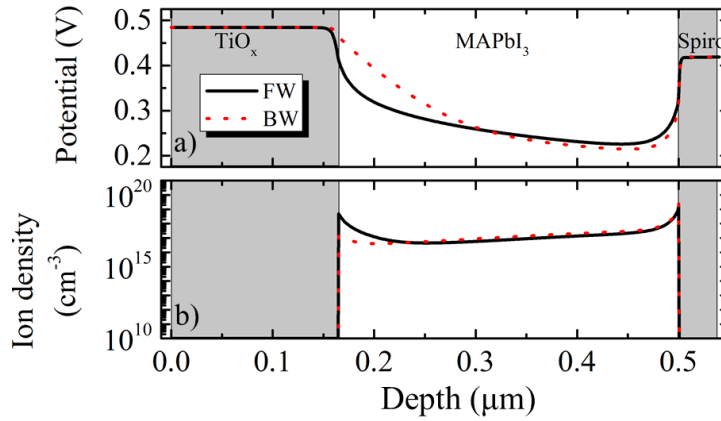


Figure 4:6 Computed a) potential profile and b) ion distribution under bias of 0.9V during forward (FW) (solid line) and backward (BW) (dot line) scan, respectively.

#### 4.1.5 Modelling of WO<sub>x</sub>/MAPbI<sub>3</sub>/Spiro-OMeTAD cells

The main properties of WO<sub>x</sub> based PSCs are listed in Table S1. Based on the previous modelling and conclusions on TiO<sub>x</sub> based PSCs, the weakness of WO<sub>x</sub> based PSCs is firstly due the bulk value of  $\tau$  (10 ns) within the perovskite on top of WO<sub>x</sub><sup>102</sup>. Secondly, the maximum achievable J<sub>SC</sub> is reduced, due to a thinner perovskite layer<sup>117</sup>; the thickness of the WO<sub>x</sub> meso-porous layer is 50nm and the porosity is measured to be equal to 30%, thus the effective thickness of MAPbI<sub>3</sub> in the porosity is reduced, leading to a total thickness of MAPbI<sub>3</sub> of only 215nm. According to the simulation (Figure 4:7), the performance losses also come from worse interface conditions between WO<sub>x</sub>



and MAPbI<sub>3</sub>. It was necessary to consider an ultrashort interface  $\tau$  (0.1 ps) and a density of mobile ions of  $5.10^{17} \text{ cm}^{-3}$  to reproduce the experimental results. The interface condition might be monitored by KPFM as illustrated in section 4.1.2 and improved by varying the annealing temperature of the WO<sub>x</sub> layer or doping WO<sub>x</sub> with Niobium (Nb)<sup>166</sup>. Further theoretical investigations, at the atomic level using DFT would be helpful for these hetero interfaces.

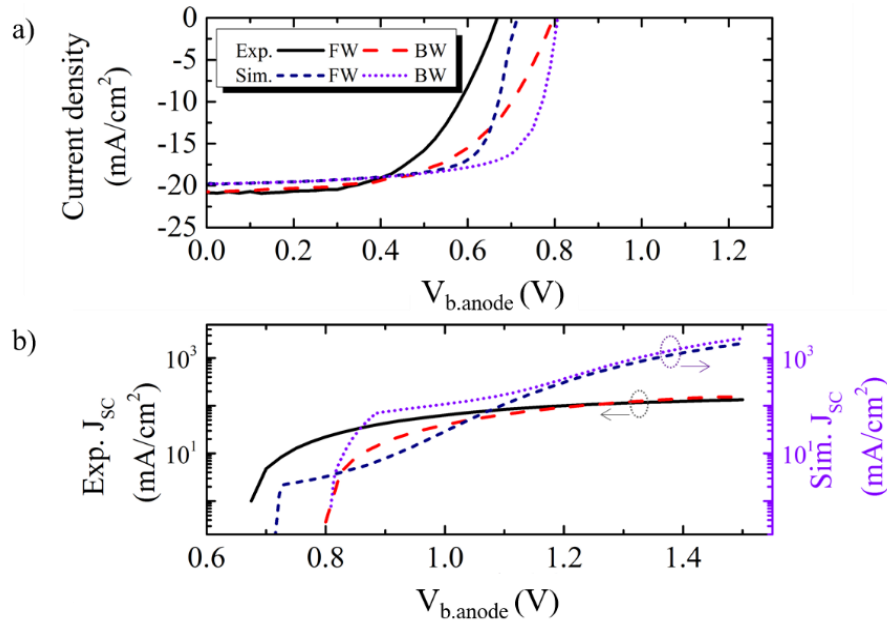


Figure 4:7 Experimental and simulated J-V characteristics of WO<sub>x</sub>-based PSCs

Moreover, the capacitance-voltage (C-V) characteristics of WO<sub>x</sub> based PSCs were simulated and compared to experimental data<sup>166</sup> (Figure 4:8). The mobile ions are assumed to be the main reason of the V<sub>bi</sub> loss between experimental (0.8 V) and ideal case (1 V), rather than the local bulk traps or the ITS. It is consistent with the previous report<sup>126</sup>, in which an effective layer of fixed donors was assumed at the MAPbI<sub>3</sub>/gold interface resulting in a reduction of V<sub>bi</sub> (section 3.4). For the simulation of the C-V characteristics, the device is pre-stabilized in the dark for 200 s. Mobile charged ions might be characterized using simulations of C-V characteristics in addition to the J-V sweeping under different scan rates, especially for the case of non-intentionally doped halide perovskite materials.



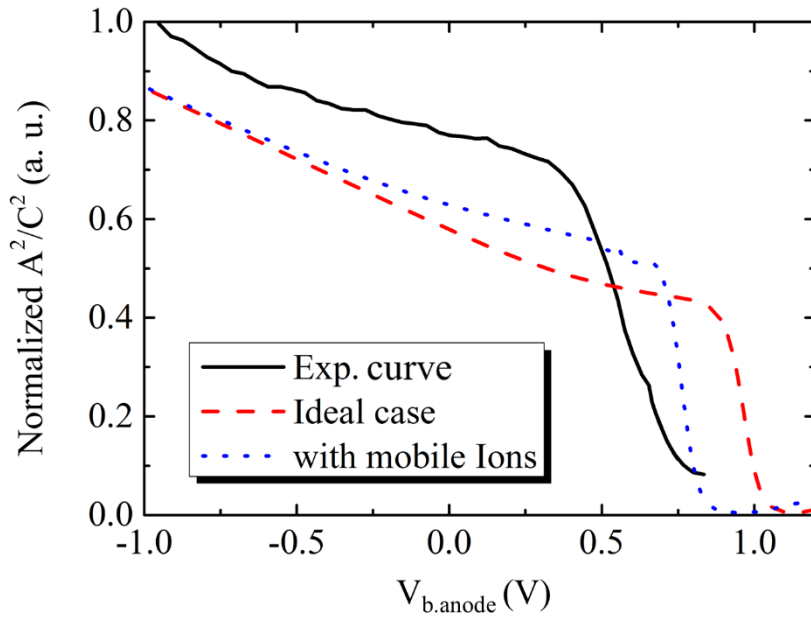


Figure 4:8 C-V characteristics of  $\text{WO}_x$  based PSCs from experiments<sup>166</sup> (solid line), simulation of ideal case (dash line) and with mobile ions (dot line) after stabilizing in dark for 200s. A is the device area.

#### 4.1.6 Discussion

The tolerance limit of halide perovskites to local traps is expected to be high, but it is not possible to remove the effect of traps completely. According to the study, the  $V_{OC}$  loss of PSCs is supposed to be mainly due to the local TR in the case of  $\text{TiO}_x$  and/or  $\text{WO}_x$  based PSCs for example, rather than the band structure difference. The annealing temperature-dependent performance of the  $\text{WO}_x$  based PSCs is attributed to the interface condition. In addition, the hysteresis effect is found to be strongly related to the ITS and mobile ions. Therefore, nowadays, the interface condition is also a crucial factor besides the bulk quality, which determines the further enhancement of the PSC performance.

## 4.2 Modelling of light-induced $J_{SC}$ degradation on inverted PSCs

Nie et al<sup>31</sup> have proposed a solution-based hot-casting technique to grow continuous, pinhole-free thin films of organometallic perovskites with millimeter-scale crystalline grains in 2015. Using this technology, PCBM/MAPbI<sub>3</sub>/PEDOT:PSS based PSCs<sup>40</sup> are realized without noticeable hysteresis effect. However, during light soaking, a reversible degradation of  $J_{SC}$  is observed as a function of time (Figure 4:9). The degradation of  $J_{SC}$  is suggested to be associated with local MA-induced me-



ta-stable deep-level traps states, while the increase of  $J_{SC}$  at the beginning of J-V characteristics under light might be related to an annihilation of  $V_I^+/I_i^-$  Frenkel pairs<sup>176</sup>, which are relatively abundant in polycrystalline MAPbI<sub>3</sub> and act as deep trap centers. For the application of PSCs on a longer term, cells biased below  $V_{OC}$  are suggested to be more stable and powerful<sup>16,40</sup>.

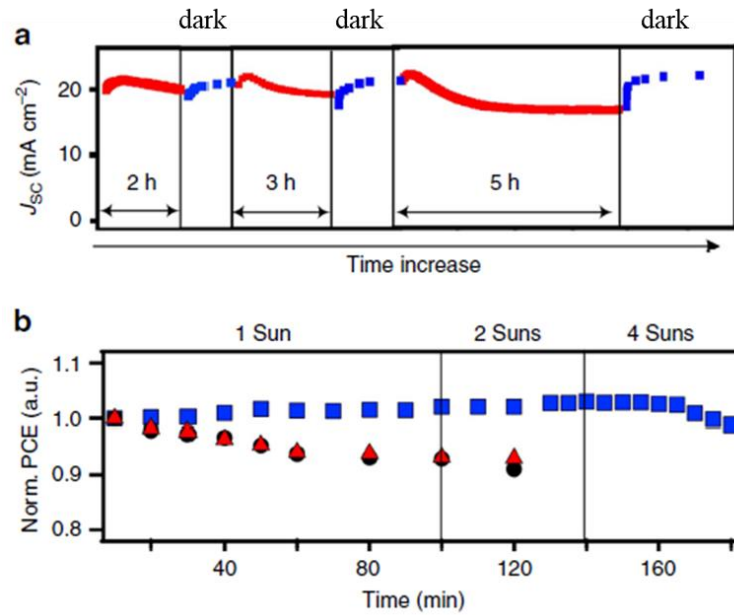


Figure 4:9 a) Reversible degradation of  $J_{SC}$  under light soaking and b) influence of light power<sup>40</sup>

In this section, the C-V and J-V characteristics of PCBM/MAPbI<sub>3</sub>/PEDOT:PSS based inverted PSCs are simulated and compared with experiments to support the hypothesis of local trap-induced  $J_{SC}$  degradation. PCBM is the ETM and PEDOT:PSS is the HTM in a p-i-n configuration (Figure 4:10). The related main parameters can be found in Table S1.

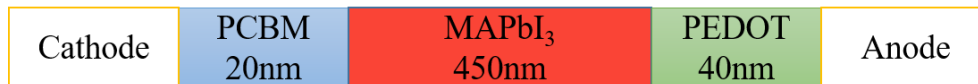


Figure 4:10 Schematic of inverted PSCs.

Figure 4:11 a) shows a C-V consistency between the experiments and the simulation, in which  $N_t$  is  $4.10^{16}$  cm<sup>-3</sup>,  $E_t$  is 0.6 eV above VBM<sup>120</sup> and  $\tau$  is 7.5 ns<sup>40</sup>. The  $J_{SC}$  degradation as a function of time can be reproduced by increasing the local  $N_t$  (Figure 4:11 b). The  $V_{OC}$  shifts from 1.1 to around 0.9



V at the beginning. Then, the further increase of  $N_t$  mainly causes the degradation of  $J_{SC}$ , while the variation of  $V_{OC}$  is limited. According to the simulation, the  $N_t$  at  $t=0$  min,  $t=15$  min and  $t=2$  hours are supposed to be  $6.10^{16}$ ,  $4.10^{16}$  and  $1.5.10^{17} \text{ cm}^{-3}$ , respectively.

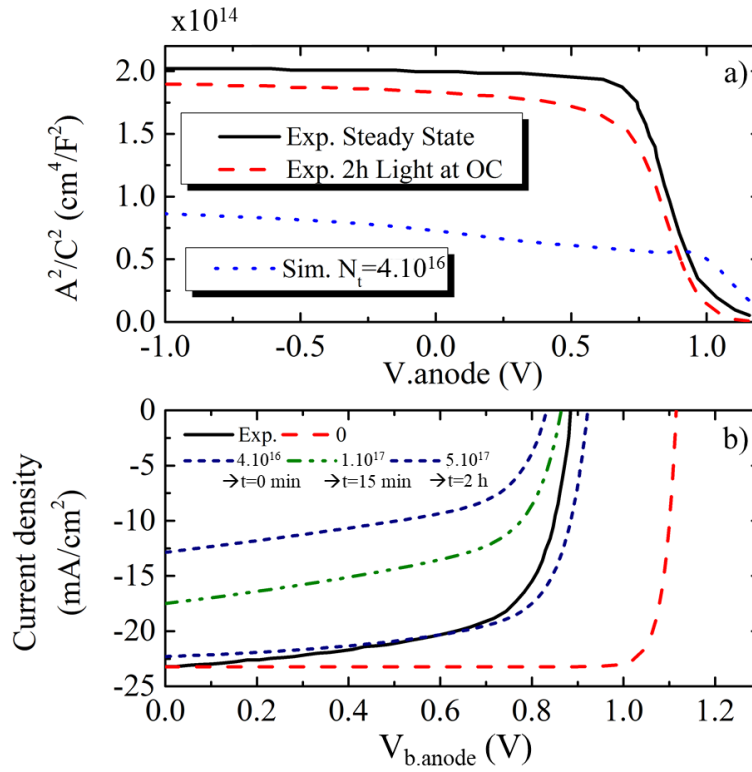


Figure 4:11 Experimental and simulated a) C-V and b) J-V characteristics with different density of local traps; the unit is  $\text{cm}^{-3}$ . A is the device area.

To explain the operation condition dependent  $J_{SC}$  degradation<sup>16,40</sup>, a hypothesis is proposed based on the interaction between metastable trap and photo-generated carriers. As shown in Figure 4:12, the photo-generated carrier distributions are different in the short and the open circuit conditions; under light, few carriers stay in the MAPbI<sub>3</sub> in the short circuit case, while considerable carriers stay in the MAPbI<sub>3</sub> in the open circuit case. Like in the case of the photoelectronic effect suggested by Staebler and Wronski<sup>177</sup> in 1977, the metastable trap states might interact with photo-generated carriers and transform to stable deep recombination centers<sup>178</sup>, leading to a reduction of carrier lifetime and  $J_{SC}$  degradation in this study. The abundant photo-generated carriers in the open circuit condition might be a booster for stable deep trap state formation. A schematic of the transition mechanism of metastable and stable traps in the MAPbI<sub>3</sub> is illustrated in the Figure 4:13. On the



right, it is the transition between stable and metastable local traps, indicated by green solid arrows. The  $k_t$  is the reaction rate from metastable traps to stable ones. The reverse reaction rate ( $k_{\text{meta}}$ ) from stable to metastable traps is assumed to hold a constant  $J_{\text{SC}}$  after soaking light more than 2h. The stable traps can capture and emit carriers, resulting in charged ions as shown on the left (solid blue arrows). But the emission rate is nearly zero for the deep traps as mentioned in section 2.3.2. By capturing photo-generated carriers, the Frenkel pairs of  $\text{V}_I^+/\text{I}^-$  might be annihilated and generate mobile charged ions<sup>176</sup> as well (blue open arrows). This process is also supposed to be reversible after recovering in the dark<sup>40</sup>. The annihilation and generation rate of the Frenkel pairs are labeled as  $a_F$  and  $g_F$ , respectively.

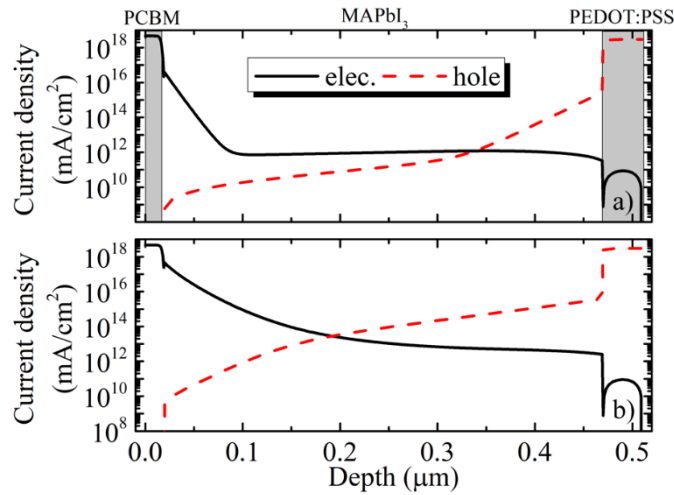


Figure 4:12 Carrier distribution under light in a) the short circuit and b) the open circuit.  $N_t$  is  $4.10^{16} \text{ cm}^{-3}$ .

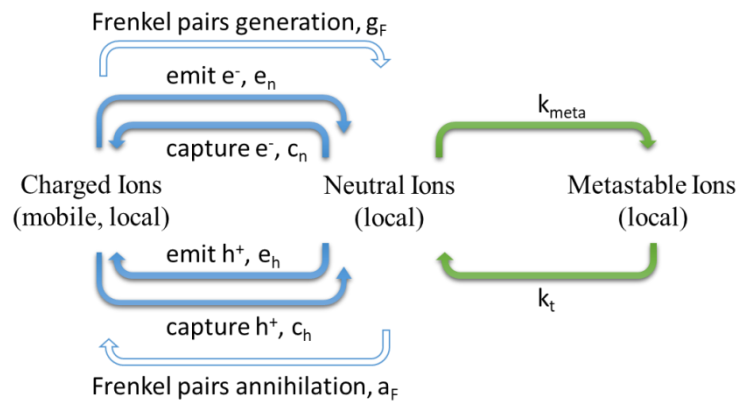


Figure 4:13 Schematic operation mechanism of metastable and stable traps



### 4.3 Summary

The  $V_{OC}$  losses of  $TiO_x$  and  $WO_x$  based PSCs are simulated and compared to experimental data. The local TR in the perovskite is the major contributor to the losses. The anomalous hysteresis effect of J-V curve is proposed to result from the cooperation between the interface traps and the mobile ions. The annealing temperature-dependent performance of the  $WO_x$  based PSCs is attributed to the interface condition. In the end, PCBM based PSCs are simulated as well. The simulated J-V and C-V characteristics are in good agreement with the experiments. The origin of the light-induced  $J_{SC}$  degradation is proposed to be the local metastable traps rather than mobile ions. The comparison of the C-V characteristics between  $WO_x$  and PCBM based PSCs could further confirm this conclusion; the ion migration could lead to the  $V_{bi}$  reduction of  $WO_x$ -based PSCs, while no  $V_{bi}$  variation is observed after the PCBM-based PSCs under 2-hour illumination.







## Chapter 5 Tunnel junctions in 2T-tandem PSC/SSCs

### 5.1 Introduction

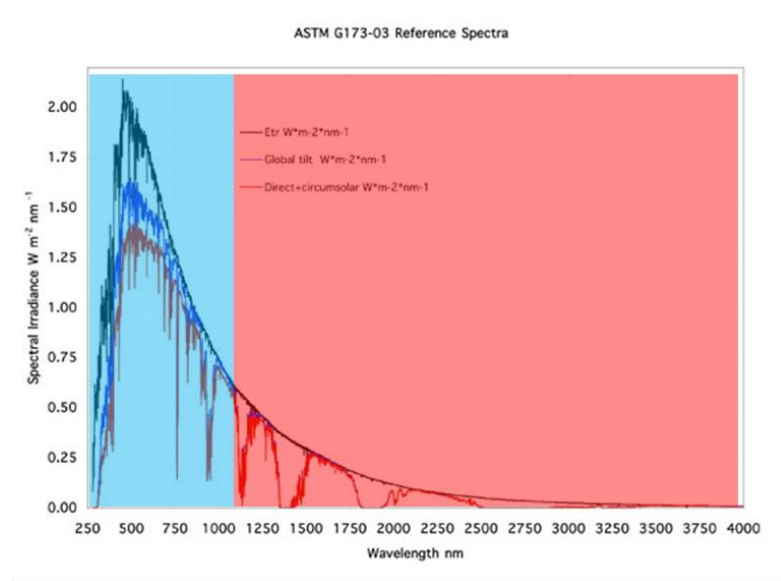
Physically limited by the hole-electron pair BR and the  $E_g$  of absorbers, a theoretical upper limit for the efficiency of p-n junction solar energy converters is well-known since 1961 and the seminal work of W. Shockley and H. J. Queisser, namely the Shockley-Queisser limit<sup>179</sup>. The maximum efficiency is predicted to be 30% for an energy band gap ( $E_g$ ) of 1.1 eV. Fortunately, this band gap corresponds to the abundant silicon material. However, as shown in Figure 1:3, after 40 years, silicon based solar cells have not yet reached the upper limit (26%). To reach higher efficiency and make a better use of the solar energy, it is possible using multijunctions to divide the absorption of the sun spectrum into several fractions. Multijunction devices combine materials with different values of  $E_g$ . Figure 5:1 shows the case of a tandem solar cell with two different sub cells in serial, for example. The photocurrent generated by each cell depends on its absorbed fraction of solar spectrum. And the absorption edge is related to the value of  $E_g$  of the absorber material in each sub cell. Hence, the resulting photocurrent of a whole tandem solar cell can be optimized by tuning the energy bandgap of the absorbers. The number of electrode terminals leads to a classification of tandem solar cells. Four terminal (4T) configuration refers to two solar cells independently connected; both cells are required to be complete devices (fabricated with front and rear contacts), which are then connected externally to combine the top and the bottom cell power output. 4T configuration requires at least three transparent electrical contacts, which reduce the total collected power due to unavoidable parasitic absorption. Two terminal (2T) configurations are solar cells connected in series and monolithically grown. They allow simpler electrical connection and less unexpected absorption. However, challenges to fabricate efficient 2T devices include i) the optical management within the tandem, ii) the fabrication of a recombination layer between the top and the bottom cells, allowing the current matching like in a series circuit. 3T – three terminals configuration is promising as well<sup>180</sup>, but this chapter will focus on the most desirable 2T configuration at this moment.



The record of 2T research-cell efficiencies is more than 40%, based on GaAs monolithic multi-junction solar cells as shown in Figure 1:3. However, they are currently developed with expensive processes and require high-quality materials. More economic alternatives have been proposed based on Si bottom cell<sup>32</sup>, targeting terrestrial applications. Theoretically predicted<sup>181</sup> in 1990, an absorber with the  $E_g$  of 1.7 eV is optimum for the top cell in the case of silicon based 2T tandem solar cells with a maximum efficiency of 37%. The first challenge is to find an absorber with a band gap of 1.7 eV. As far as we know, III-V<sup>182</sup>, CIGS<sup>183</sup> and perovskite<sup>184</sup> materials can be candidates for that purpose. The top sub-cell can consist in methyl ammonium mixed bromide-iodide lead perovskite,  $\text{MAPbI}_{3(1-x)}\text{Br}_{3x}$  ( $0 \leq x \leq 1$ ). By changing the bromide ratio, we can tune the bandgap of the perovskite absorber<sup>184</sup>. Focusing on the target of the cost competition, perovskites seems to be the most promising top cell absorbers<sup>43,180,185–187</sup>. However, a layer with a high recombination rate is needed to enable a current matching. Band to band tunneling realized with a  $p^+/n^+$  junction is one solution<sup>185</sup>, in which electrons and holes stay close to the junction, having a chance to go through the energy bandgap and recombine. However, dopants in halide perovskites are hard to control, and might be even mobile as mentioned in section 4.1.4. Thus, the current-matching between the top and the bottom cells may be rather realized within Si<sup>188–190</sup>. This solution is numerically investigated and discussed in the following sections.



a)



b)



Figure 5:1 a) solar spectrum is splitted into two parts and absorbed by b) a tandem solar cell

## 5.2 Device structure and simulation

### 5.2.1 Silicon tunnel junction

To grow the tunnel junction, the diffusion technology is typically used (section 3.3) and might have a neutralization effect: the heavy n- and p-type dopants can thermally diffuse into each other at high temperature, leading to net zero doping levels or reduced doping levels without tunnelling effect. Therefore, the knowledge of the minimum doping level of the  $n^+$  and  $p^+$  regions of this junction is mandatory. For computational purpose, a silicon junction with  $n^+$  and  $p^+$  doped regions (each 20 nm thick) was studied. The doping level was assumed to be the same on both sides of the junction. Figure 5:2 shows the computed variation of the tunnel junction peak current and the negative differential resistance, which is representative of the peak-valley current ratio. Variations of six orders of magnitude are observed for a doping level increasing from  $3 \cdot 10^{19}$  to  $10^{20}\ cm^{-3}$ .



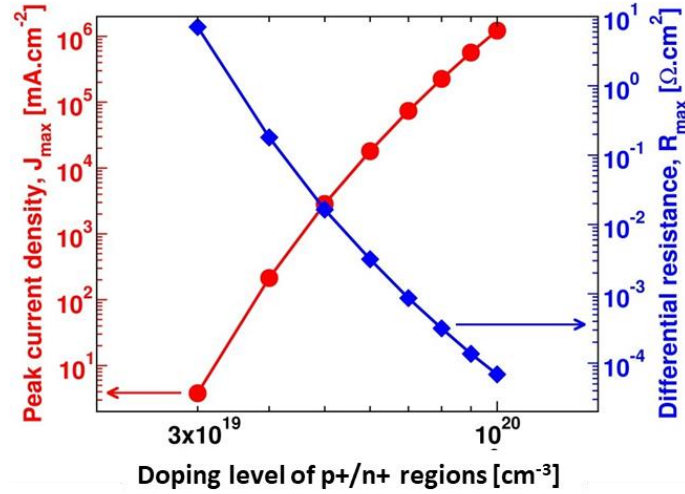


Figure 5:2 Characteristic of the tunnel junction as a function of the doping level. The peak current density  $J_{max}$  [mA.cm<sup>-2</sup>] and the differential resistance  $R_{max}$  [Ω.cm<sup>2</sup>] are marked by red circles and blue squares, respectively.

### 5.2.2 Modelling of perovskite/silicon tandem solar cells

Tandem cells were simulated with different values of the doping levels in the tunnel junction and different thicknesses of the MAPbI<sub>3(1-x)</sub>Br<sub>3x</sub> perovskite layer. Figure 5:3 shows a scheme of the perovskite tandem solar cell monolithically integrated on an *n*-doped silicon substrate. A 280 μm thick *n*-type Si substrate with *n*-type 10<sup>16</sup> cm<sup>-3</sup> dopants is used. Deep trap states are considered with  $E_t$  at 0.5 eV above the VBM, and a diffusion length of 600 μm. On the bottom of the Si substrate (the left part of Figure 5:3), a 100 nm thick *n*<sup>+</sup> Si layer is added to make an Ohmic back contact. For the top cell, a MAPbI<sub>3(1-x)</sub>Br<sub>3x</sub> absorbing layer is sandwiched by TiO<sub>x</sub> (as ETM) and spiro-OMeTAD (as HTM) layers. The  $A_\alpha$  prefactor for the perovskite here is set as 2.5.10<sup>5</sup> cm<sup>-1</sup>eV<sup>-1/2</sup> in Equation 2–10 to compute the absorption spectrum. Between the top and the bottom cells, a p+/n+ silicon-based tunnel junction is inserted.



Figure 5:3 Schematic architecture of a 2T perovskite/silicon tandem solar cell  
Spiro is a short name for spiro-OMeTAD.

The optimum doping level of the tunnel junction is found to be around 5.10<sup>19</sup> cm<sup>-3</sup>, to ensure an efficient tunneling probability while preserving a good material quality. Lower doping levels can lead to a wider distance between the CBM and the VBM and a weaker tunneling effect. Higher dop-



ing levels could result in material degradation. The computation of different thicknesses of the perovskite layer are summarized in Figure 5:4, in addition to different bromide ratio. The optimized structure with current matching is found for a 350 nm-thick perovskite layer, with 20% bromide ratio. The related value of  $E_g$  of  $\text{MAPbI}_{2.4}\text{Br}_{0.6}$  is 1.7 eV, which is consistent with a previous report<sup>181</sup>.

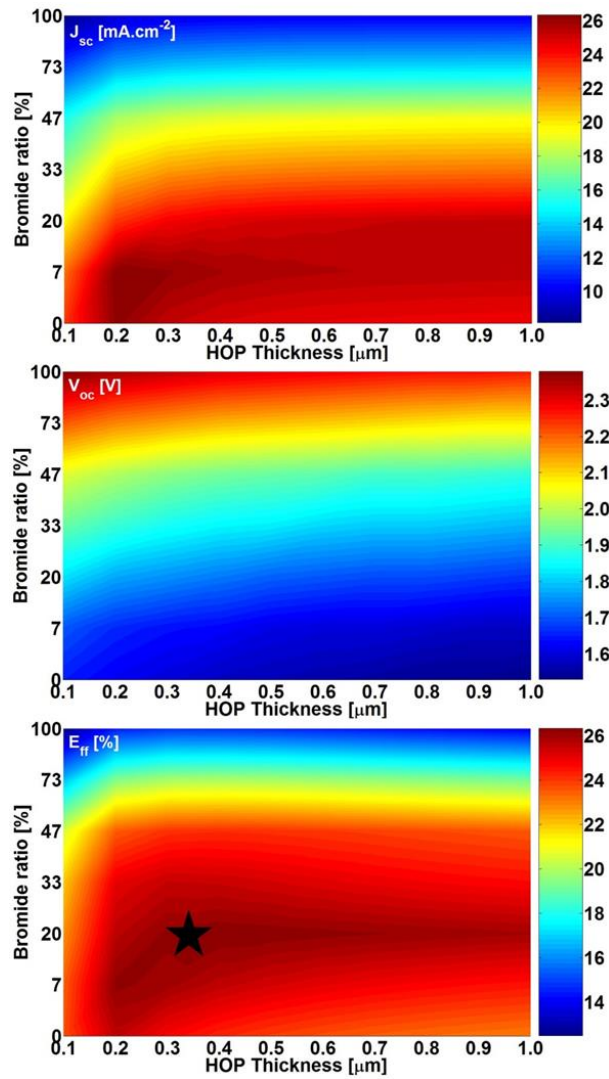


Figure 5:4 Simulated photovoltaic properties of tandem cells  
a)  $J_{sc}$ , b)  $V_{oc}$ , and c) efficiency ( $E_{ff}$ ). The black star in c) marks the maximum efficiency 27% obtained for a thickness of the perovskite layer of 350 nm and a bromide ratio of 20%, referring to an energy bandgap of 1.7 eV.

The simulated static band alignment of the optimized structure is presented in Figure 5:5. The constant  $E_f$  goes through the VBM (CBM) in the  $p^+$  ( $n^+$ ) region of the tunnel junction, indicating a high



density of holes (electrons). Along the growth direction (the x-axis in Figure 5:5), the distance between the regions presenting high densities of holes and electrons is small, leading to a strong band to band tunneling effect. In the simulation, electrons in the  $n^+$  region of the tunnel junction go through the energy bandgap and occupy equivalent vacancies (holes) in the VBM of  $p^+$  region. A recombination rate expression for the tunnelling effect is used into the current continuity equations (Equation 2–2) to ensure a good electrical connection in between. The J-V characteristics of individual cells and of the tandem cell are summarized in Figure 5:6. The optimized efficiency of the tandem solar cell is 27%, while the efficiencies are 17.3% and 17.9% for the individual silicon based and perovskite based solar cells, respectively.

### 5.3 Perspective

For more realistic simulations, it will be necessary to go beyond the approximation of abrupt doping regions in the tunnel junction. This difference might bring variations of the J-V characteristics. For future investigations, KPFM might be a well-suited characterization technique to study the carrier accumulation, recombination and band alignment around the tunnel junction, leading to optimized growth of the tunnel junction.

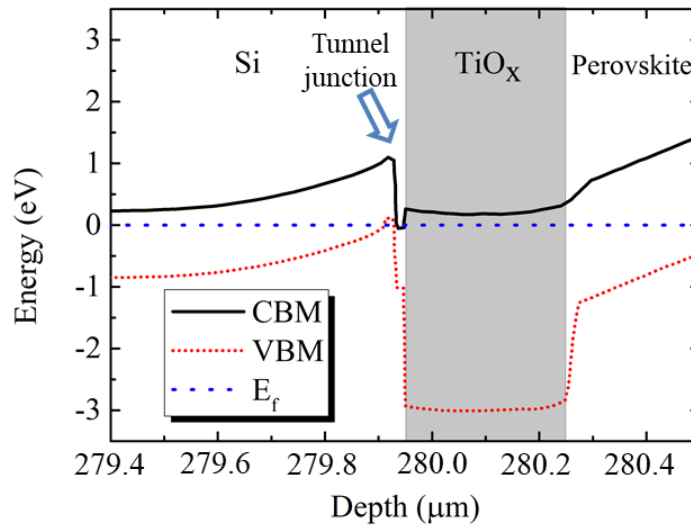


Figure 5:5 Static energy band alignment of a tandem solar cell  
The  $n^+$  and  $p^+$  doping levels in the tunnel junction are equal to  $5 \cdot 10^{19} \text{ cm}^{-3}$ . The open arrow indicates the location of the silicon-based tunnel junction.



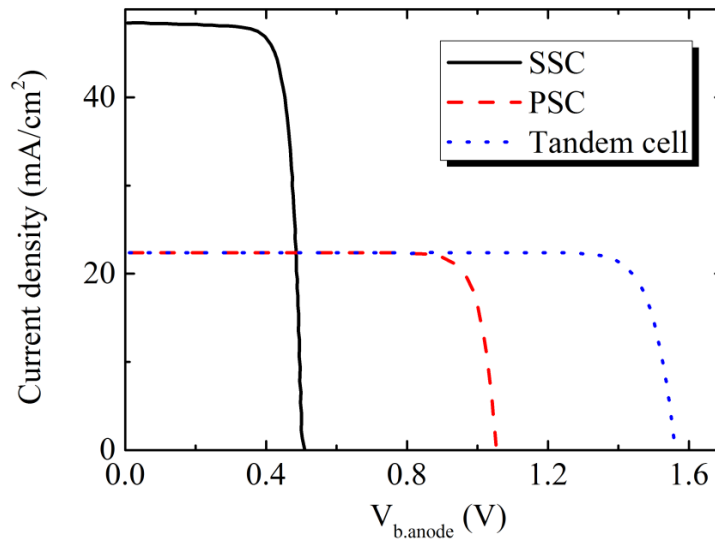


Figure 5:6 J-V characteristics of the individual cells and the tandem one. SSC and PSC are short names for the silicon and the perovskite-based sub solar cells, respectively.







## Chapter 6      Electrical properties of III-V/GaP QD structures on silicon for light emission

### 6.1 Introduction

To meet the growing demand of data transmission and to reduce energy consumption in the field of optical telecommunication, the integration of a laser<sup>191</sup> on silicon has attracted much interest in the past decade, especially the hybrid integration with III-V materials<sup>192</sup>. Different approaches have been proposed<sup>193</sup>: wafer-bonding based heterogeneous integration, transfer printing and monolithic integration. The last one is expected to better match with very large-scale integration on a longer term. Unfortunately, crystalline defects generated during the III-V/Si hetero-epitaxy are known to limit nowadays laser device performances; a thick buffer layer and super lattices<sup>194</sup> or V-grooved surface<sup>195,196</sup> are usually needed to avoid the emergence of these structural defects. However, these technologies limit the optical coupling solutions on silicon chips. Recently, it was proposed by several groups to use a pseudomorphic GaP/Si template, benefiting from the low lattice mismatch between GaP and Si (0.37% at room temperature) to limit the formation of structural defects<sup>197</sup>. In this approach, the structural benefit is, however, counterbalanced by the limited optical properties of most GaP-based materials. GaP is indeed an indirect bandgap material. One of the solution is to introduce dilute nitrides into the GaAsP quantum wells<sup>198</sup>, whose efficiency is, however, intrinsically limited by a pseudo direct bandgap optical transition<sup>199</sup>. III-V monolithically integrated on silicon became promising after the demonstration of a true band to band light emission: room temperature PL<sup>200</sup> and EL from structure containing high densities (In,Ga)As/GaP quantum dots (QDs)<sup>201</sup>. PL<sup>200,202,203</sup>, EL<sup>204</sup> and laser<sup>205</sup> of low indium (In,Ga)As/GaP based structures have been reported at about 1.8 eV. The bandgap of the active layers is thus much larger than more classical (In,Ga)As-based structures<sup>206</sup>. The large  $E_g$  is induced by strain and was firstly noticed by Fukami et al from a simple model-solid theory approach<sup>207</sup>. Later, empirical tight-binding calculations<sup>90</sup> additionally proposed that the CBM of strained GaAs QDs on GaP is rather  $X_{xy}$ -like than  $\Gamma$  like. More, the



strain-induced band splitting of X valley in GaP layer may result in a potential well near the GaP layer and the QDs, leading to a possible type II transition from the GaP CBM to the QD VBM. The strained GaP region is named as sGaP for short in the present work. Aiming at future integration on silicon wafers and electrical injection, the carrier transport and recombination in the (In,Ga)As/GaP structure are important but experimental results are scarce. EL characteristics of a 5 layers structure of InGaAs/GaP QDs with low Indium content are investigated in the present chapter. Based on the previous experimental<sup>90</sup> and theoretical<sup>208</sup> investigations on the band structure of (In,Ga)As/GaP QDs, drift-diffusion simulations are used to study the transport of carriers inside the structure.

## 6.2 Architecture and EL characteristics of devices

The epitaxial growth of the samples was performed using the solid source molecular beam epitaxy on GaP substrates<sup>209</sup>. These substrates are n-doped of  $4.10^{18} \text{ cm}^{-3}$ . As shown in Figure 6:1 a), active regions are sandwiched by n- and p-doped AlGaP layers<sup>210</sup>, which could be used to afford optical confinement<sup>211</sup> for future laser application. Heavily doped GaP layers are added to realize Ohmic contacts for the anode and the cathode<sup>212</sup>. The thickness and the doping level of each layer are indicated on Figure 6:1 a). Generally, the QDs have a pyramidal or truncated core shape<sup>208</sup>, as illustrated in Figure 6:1 b). We considered an approximated cylindrical shape for the Silvaco simulations.

Pulsed electrical waves are used to characterize the EL characteristics under low electrical injection. The peak power is  $0.5 \text{ kA/cm}^2$  and the cycle ratio is  $2.10^{-3}$ , corresponding to an effective current density of  $1 \text{ A/cm}^2$ . As presented in Figure 6:2 a), the EL characteristics are studied as a function of temperature, and a clear redshift is observed. Following the Equation 2–21, the Varshni parameters are extracted as the  $\alpha$  of  $0.5 \text{ meV/K}$  and the  $\beta$  of  $-50 \text{ K}$ , if we assume that the emission peak energy is equal to  $E_g$  and that the emission peak at  $0\text{K}$  is the same as in a previous report<sup>90</sup>. In addition, a thermal quenching of the EL intensity is noted. This issue will be discussed with the help of the simulation in the following sections.

## 6.3 Modelling of electrical properties of QDs

To minic the real architecture of the devices but also to keep the numerical model simple, cylindrical architectures with one cylindrical QD on each wetting layer were considered. In the simulation,



the QDs have a height of 3.5 nm and are divided into two parts. The top and the bottom parts are labeled as QDtop and QDbot, respectively. Due to the indium atoms redistribution<sup>202</sup>, the indium contents are assumed to be different in the top and bottom parts of the QDs:  $\text{In}_{0.2}\text{Ga}_{0.8}\text{As}$  at the top and GaAs at the bottom, leading to an average indium content of 10% for each QD. The QDs layers are labelled 1<sup>st</sup> to 5<sup>th</sup> along the growth direction (y direction). The wetting layer (WL) with a thickness of 0.5 nm is assumed to be filled with  $\text{In}_{0.1}\text{Ga}_{0.9}\text{As}$ . Around the (In,Ga)As QDs and WLs, sGaP layers are taken into account with an effective thickness of 2 nm. This thickness was estimated from atomic positions obtained from a TB model of supercell<sup>90</sup>. The main material properties can be found in Annex III, including the band edge positions and the effective masses used to solve Schrodinger's equation and to calculate bound states energies<sup>92</sup>.

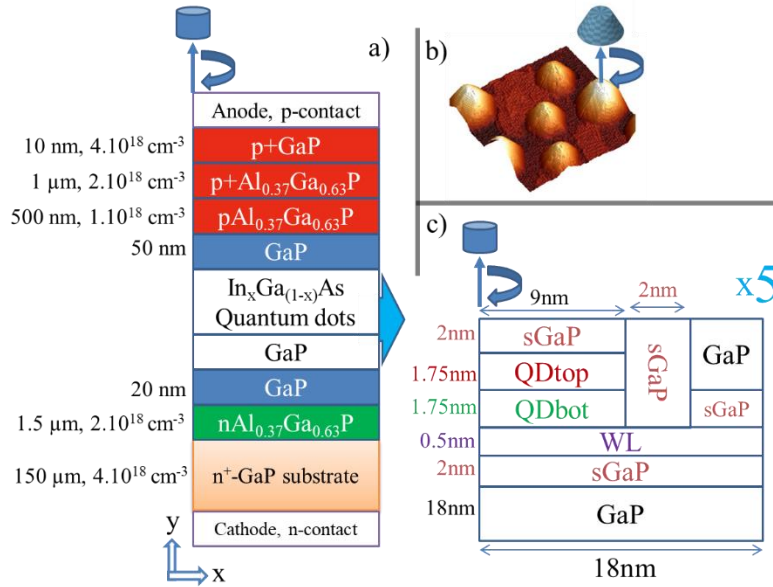


Figure 6:1 Schematic representation of the QD device architecture

- a) Overview. n and p indicate the doping types. Plus sign means heavily doped. b)  $75 \times 75 \text{ nm}^2$  STM 3D plane view of (In, Ga)As QDs. c) the structure details for one layer of QD. sGaP stands for strained GaP. WL corresponds to the wetting layer of  $\text{In}_{0.1}\text{Ga}_{0.9}\text{As}$ . The QD is separated into two parts; QDtop is the top part ( $\text{In}_{0.2}\text{Ga}_{0.8}\text{As}$ ) and QDbot is the bottom part (GaAs). The QD region in c) is repeated five times referring to five layers of QDs. The QD shape is approximated as a cylinder.



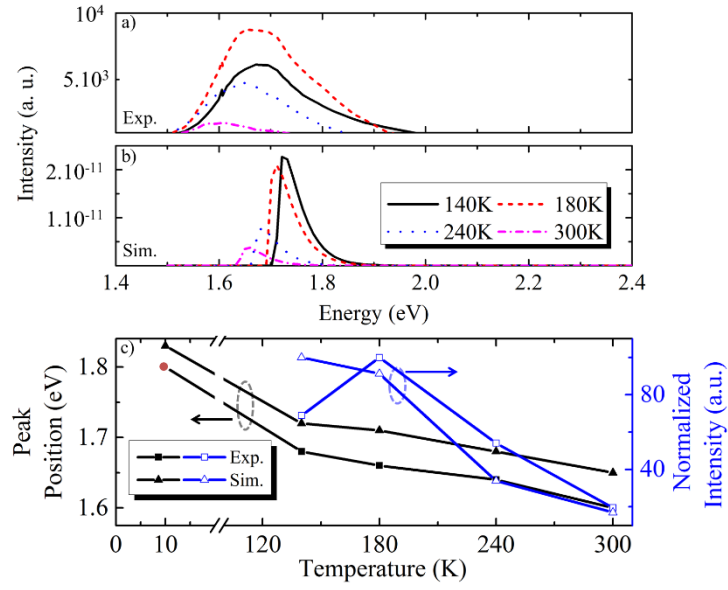
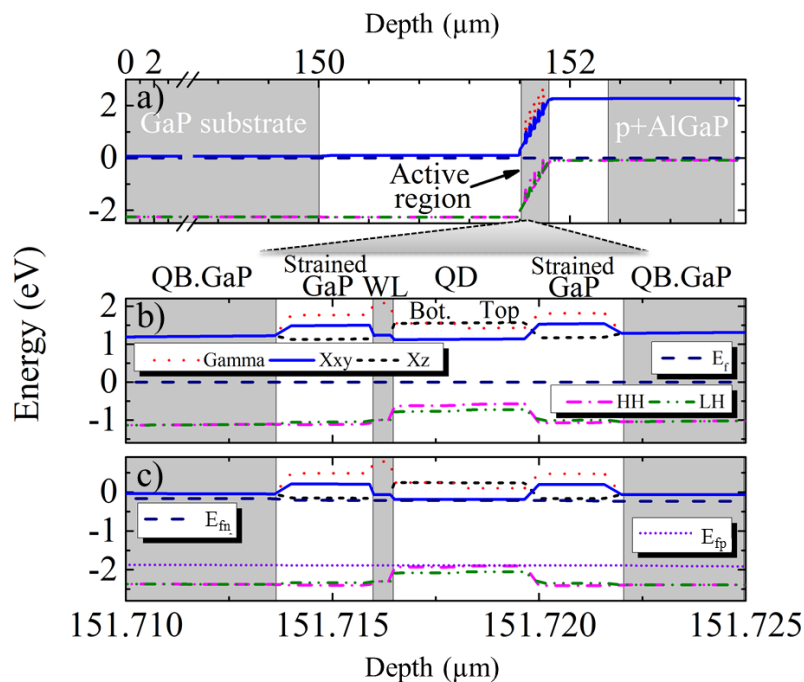


Figure 6:2 a) Experimental and b) computed EL spectra under low electrical injection. The injection current density is  $1 \text{ A/cm}^2$ . c) Summary of the emission peak position and normalized intensity as the function of the temperature of the thermal contact. The red dot relates to the report of emission peak energy at 10 K for (In, Ga)As/GaP QDs<sup>208</sup>.

Six bound state energies in the conduction band and one in the valence band were obtained from the present simulation, and then used to compute the spontaneous radiative recombination rate of the strained QDs active layers. Noticably, in the present work, the Schrödinger and Poisson coupled equations are only solved along the growth direction, due to the limitations of the computational resources. Thus, the calculated radiative recombination rate is rather related to (In, Ga)As quantum wells, while the calculated carrier transport properties are more closely related to cylindrical QDs. The computed static band alignment is represented in Figure 6:3 a) and the 1st QD layer is zoomed out in b). The CBM of the QD and the sGaP material are  $X_{xy}$  and  $X_z$ , respectively<sup>90</sup>. Thus, a competition between the transitions from the  $X_{xy}$  of the QD and the  $X_z$  of the sGaP material may exist. The  $\Gamma$  valley of QD is located between  $X_{xy}$  and  $X_z$  valleys in the QDtop region, where the indium content is large (20%). Figure 6:3 c) shows the computed band alignment under bias and the Fermi level  $E_f$  is splitted into two quasi Fermi levels ( $E_{fn}$  and  $E_{fp}$ ) to describe the carrier distributions in the conduction band and valence band. The VBM of the QDs is related to a heavy hole state (HH), while the one of sGaP is related to a light hole state (LH).



According to previous analytic modelling<sup>213</sup>, the thermal quenching of EL intensity might be caused by the carrier thermal escape and trap-induced recombination in the active region. In the present work within the drift-diffusion framework, a similar approach is implemented considering the temperature dependent carrier mobilities and trap states (see Equation 2–23 - 24). The total trap density is set to  $2.10^{17} \text{ cm}^{-3}$ ,  $E_{\text{at}}$  to 0.34 eV and  $\alpha_t$  to  $1.10^{-7}$ . The physical meaning of  $E_{\text{at}}$  refers to an abrupt increase of the active trap density for temperature larger than 180 K. The influence of traps in the active region on the EL intensity is found to be much more detrimental than carrier escape. Traps in the WLs and quantum barriers are found to be less harmful. Due to the electric fields induced by the band offsets at heterojunctions, injected carriers are captured by the QDs before recombining in the WL and quantum barriers. The origin of the traps in the QDs might be indium vacancies; indium atoms in the QDs are indeed found to migrate and accumulate at the top of the QDs during the post annealing.<sup>202</sup>





carrier capture rate associated to this process is large, the transition from the QD  $X_{xy}$  and the sGaP  $X_z$  to the QD VBM might have similar weights. However, due to computational limitations, this more elaborate capture process can not be considered.

The mapping of the carrier distributions in dark and under light is presented in Figure 6:4, along with the Radiative Recombination Rate (RRR) profile in the active regions. Few electrons are in the active region in the static case (Figure 6:4 b), while plenty of holes are found in the 5th QD layer closed to the p-doped region (Figure 6:4 c). Generally, the intrinsic region in a p-i-n configuration is depleted in the static case. However, as deep wells exist in the VBM of the QDs in the present work<sup>90</sup>, lots of holes are trapped in the VBM well near the p doped region. Under low electrical injection, injected electrons with small effective masses are attracted by the accumulation of holes with large effective masses. On the right of Figure 6:4, the blue and red arrows indicate the electron and the hole flowing directions, respectively. Intriguingly, the incoming electrons are found to flow through paths outside the QDs and to recombine with holes in the 4th QD layer, leading to an increase of RRR in the 4th QD. The path through QDs exhibits more interfaces and barriers than the one going through GaP layers and WLs. In addition, the effect of the potential well related to sGaP  $X_z$  states is observed, leading to electrons trapping.

## 6.4 Perspective

The EL characteristics of devices based on (In,Ga)As/GaP QDs with low Indium content are investigated by the experiments. The thermal quenching of the EL intensity is mostly attributed to trap-induced recombination in the active regions, in addition to carrier thermal escape. The computations of the carrier transport and recombination in static condition and low electrical injection are presented. The intriguing carrier accumulation phenomenon deserves further experimental and theoretical investigations in the future.



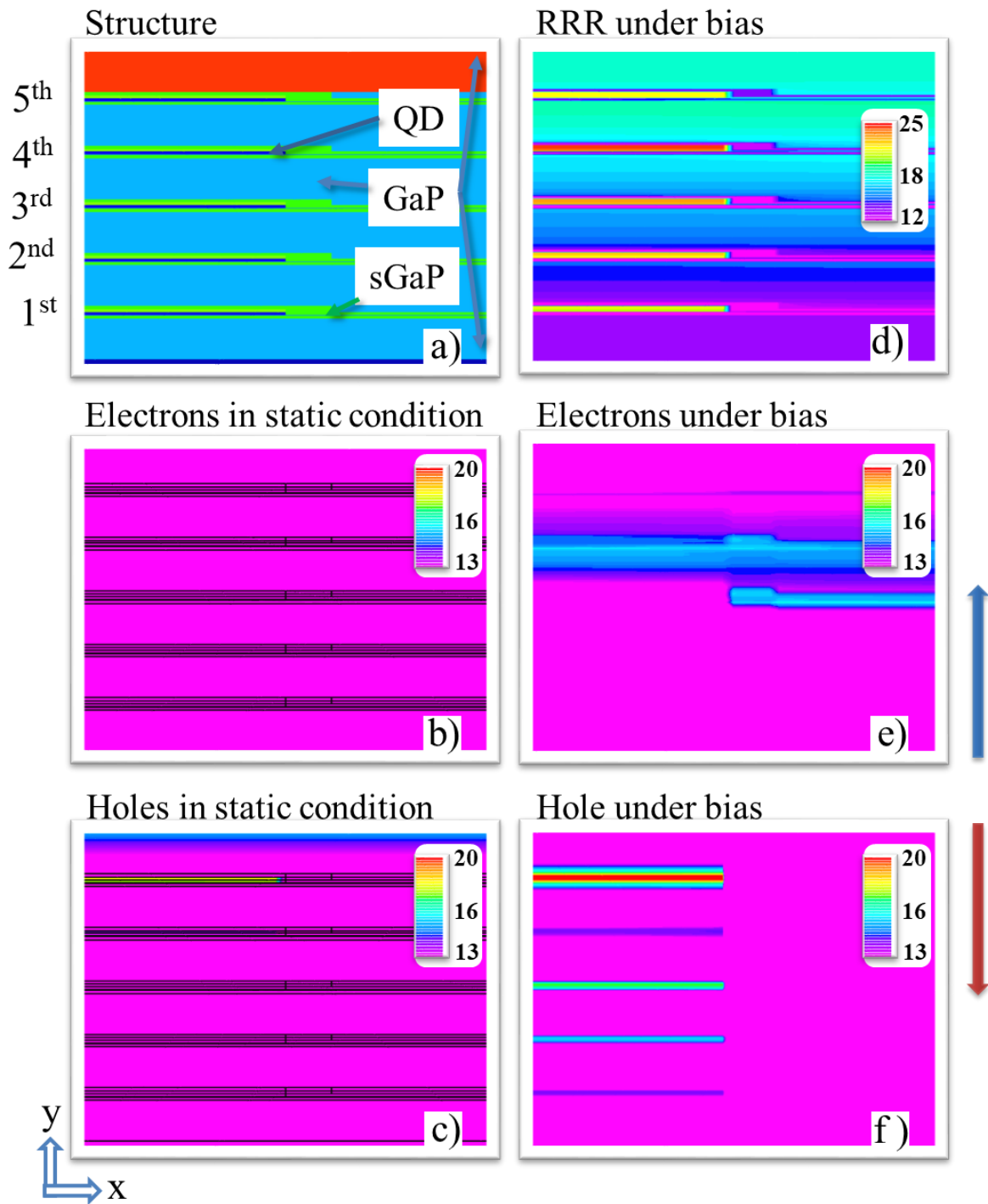


Figure 6:4 Carrier distribution and RRR profiles

a) Presentation of the active regions. Data for b-f) are presented in log scale with the unit of  $\text{cm}^{-3}$  and  $\text{cm}^{-3}\text{s}^{-1}$  for carrier densities and RRR, respectively. The labels of QDs are listed on the left. b) Electron and c) hole distributions in static conditions. For the figures in the left column, the configuration lines are drawn as eye guide. Under low electrical injection, d) RRR profile, e) electron and f) hole distributions are illustrated. The arrows on the right indicate the flowing directions of electrons (blue) and holes (red) under electric injection.







## Annex I Material properties for perovskite modelling

Table S1 Main properties for the materials associated with PSCs

	$E_g$ (eV)	$\chi$ (eV)	$m_e^*$ ( $m_0$ )	$m_h^*$ ( $m_0$ )	$\epsilon$ ( $\epsilon_r$ )	$\alpha_{rad}$ ( $\text{cm}^3/\text{s}$ )	$\mu_e$ ( $\text{cm}^2/\text{Vs}$ )	$\mu_h$ ( $\text{cm}^2/\text{Vs}$ )
TiO <sub>x</sub>	3.3	4.1	1	1	31	/	2	2
MAPbI <sub>3</sub>	1.55	3.88	0.23 (214)	0.29	70	$10^{-10}$ (97,98)	0.4	0.05
Spiro	2.85	2.15	0.06	0.8	3	/	$2 \cdot 10^{-4}$	$2 \cdot 10^{-4}$
WO <sub>x</sub>	3.55	4.2	1.3	1.3	100	/	2	2
PCBM	2	3.8	1	1	4	/	0.087	0.087
PP	3.54	1.76	0.82	0.82	38	/	0.02	0.02
Si	1.12	4.05	0.36	0.81	11.7	$10^{-14}$	1000	500

Note: spiro is spiro-OMeTAD; PP is PEDOT:PSS. The  $E_g$  of Spiro is artificially increased to 2.85eV referring to a WF of 5.2eV of lithium-doped Spiro<sup>215</sup>, while the absorption properties<sup>117</sup> and affinity<sup>216</sup> are kept the same as intrinsic Spiro. The MAPbI<sub>3</sub> radiative recombination coefficient comes from the report<sup>98</sup>

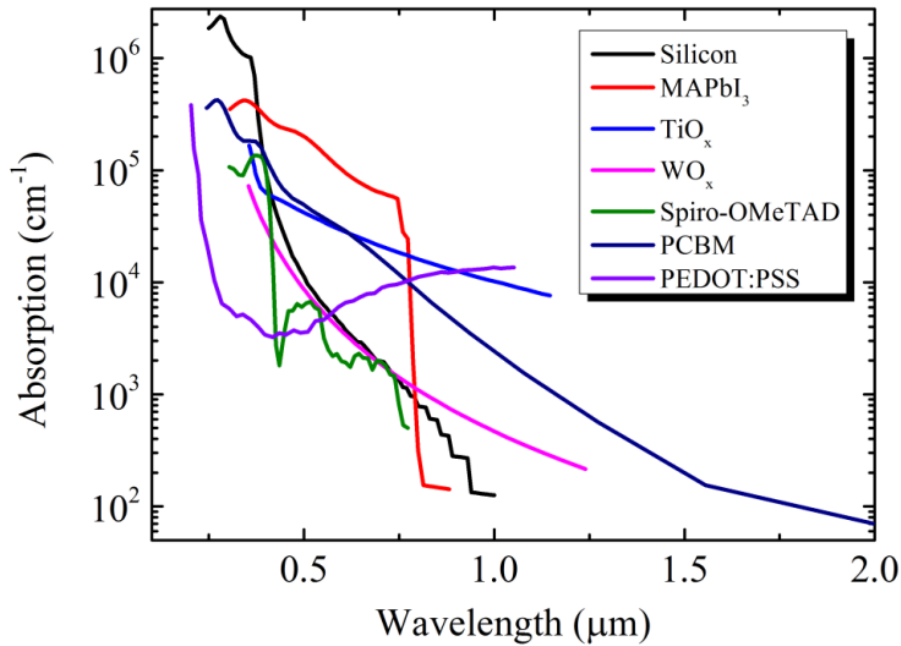


Figure S1 Absorption spectrum of various materials



# ASTM G173-03 Reference Spectra

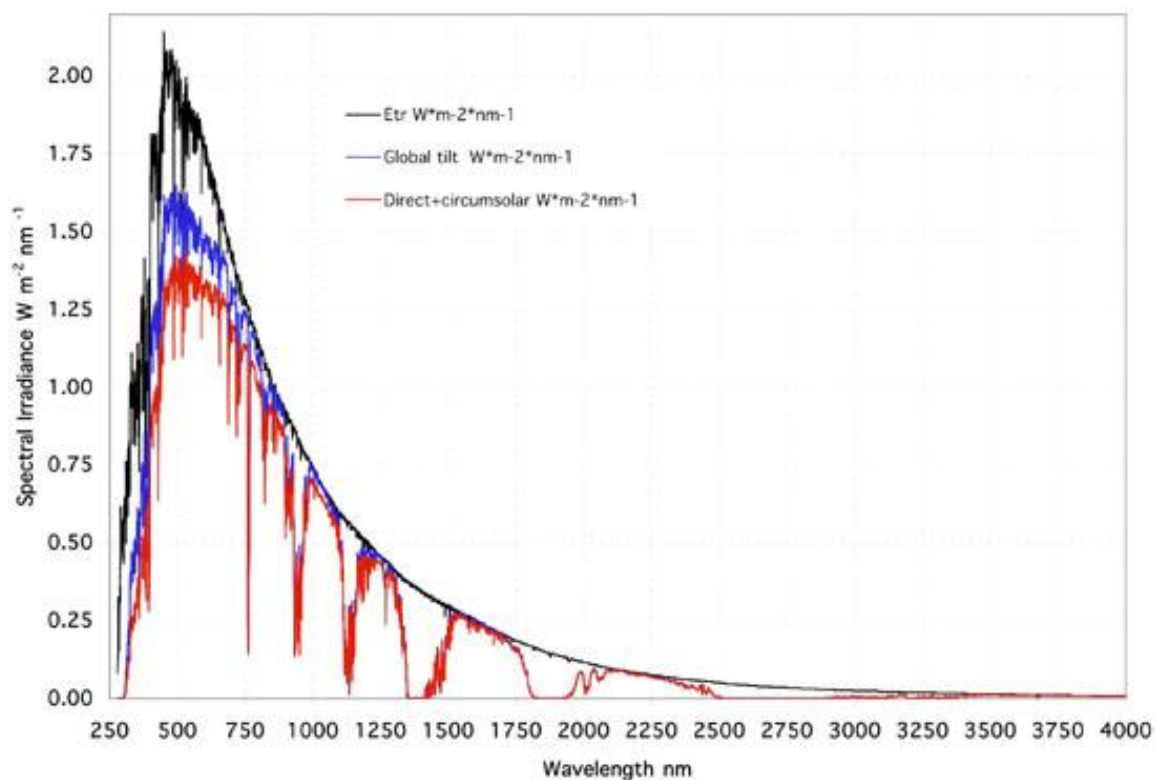


Figure S2 Reference Solar Spectral Irradiance.  
Global tilt (AM1.5G) is used in the study.



## Annex II KPFM on silicon-based junctions under light

The illumination leads to a downshift of the  $V_{CPD}$  from black line to the dash red line, as shown in Figure S3. Similar trend is observed in the simulation. The light source in the simulation is set as a laser source with a wavelength of 448 nm and an output power of  $1 \text{ W/cm}^2$ . More investigations are possible with realistic illumination conditions and doping profiles inside silicon layers.

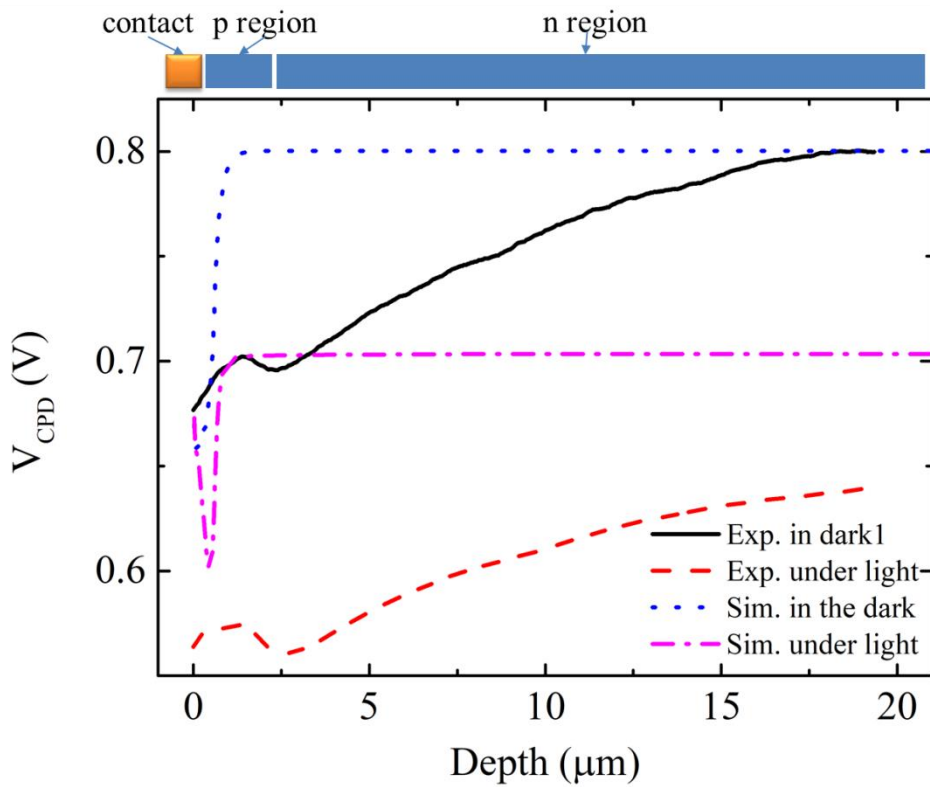


Figure S3 Experiments and simulation of  $V_{CPD}$  in the dark and under illumination.







## Annex III Material properties for III-V QDs modelling

The band properties of GaP and AlGaP are taken from Vurgaftman et al.<sup>182</sup>, while that of the strained (In,Ga)As and GaP are refined according to the experimental and theoretical investigations of C. Robert et al.<sup>90,208</sup>. The  $\Gamma$ -HH bandgap at 0K ( $E_{g0}$ ) of the top part of QDs is deduced from the PL spectrum<sup>90</sup> at 10K using Varshni law. The  $\Gamma$ -HH  $E_g$  of the strained GaAs in the bottom part of QDs is calculated using the variation as a function of indium composition obtained from a TB model<sup>208</sup>. The affinity of the  $X_{xy}$  valley at 0K is set as a constant in QDs, while the HH energy position changes as a function of indium content. The  $X_z$  valley is assumed to be at the same level than the  $\Gamma$  valley of strained GaAs in QDs. The strain-induced splitting of valence band, namely the difference of HH and LH in the QDs is extracted from TB model<sup>208</sup>. In the GaP closed to the (In,Ga)As region, a shallow potential well is introduced for the  $X_z$  valley. The difference between the minimum of  $X_z$  valley in sGaP and the HH in the bottom of QDs is set to fit the TB computation<sup>90</sup>. The  $X_{xy}$  valley of sGaP is arbitrarily set above the X valley of bulk GaP, referring to a reverse variation of X valley splitting in QDs. The  $\Gamma$  valley of sGaP is simply assumed to be the one of bulk GaP. The static band alignment is presented as Figure 6:3. The Auger coefficient is set to be the same of  $1.10^{-30} \text{ cm}^6/\text{s}$  for all the materials.



Table S2 Band structure of III-V for QDs device

Material	Valence band	Eg0	$\alpha$	$\beta$
	(eV)	(eV)	(meV/K)	(K)
GaP	VBM 6.06	X 2.35	0.5771	372
Al <sub>0.37</sub> Ga <sub>0.63</sub> P	VBM 6.23	X 2.38	0.5771	372
	HH 6.08	X <sub>xy</sub> 2.56		
strained GaP	LH 6.01	X <sub>z</sub> 2.20	0.5	-50
		$\Gamma$ 2.84		
Wetting Layer	HH 5.97	X <sub>xy</sub> 2.35		
In <sub>0.1</sub> Ga <sub>0.9</sub> As	LH 5.97	X <sub>z</sub> 2.35	0.5405	204
		$\Gamma$ 3.11		
Bottom of QD	HH 5.60	X <sub>xy</sub> 1.85		
GaAs	LH 5.75	X <sub>z</sub> 2.28	0.5	-50
		$\Gamma$ 2.28		
Top of QD	HH 5.57	X <sub>xy</sub> 1.85		
In <sub>0.2</sub> Ga <sub>0.8</sub> As	LH 5.72	X <sub>z</sub> 2.28	0.5	-50
		$\Gamma$ 2.14		

Table S3 Effective mass and dielectric constants

Material	Valence band	Valley	Relative per-	Radiative
	(m <sub>0</sub> )	(m <sub>0</sub> )	mittivity ( $\epsilon_0$ )	recombination
GaP	VBM 0.83	X 0.79	11.1	$\alpha_{\text{rad}}=1\text{E-}13 \text{ cm}^3/\text{s}$
Al <sub>0.37</sub> Ga <sub>0.63</sub> P	VBM 0.83	X 0.79	10.6	$\alpha_{\text{rad}}=1\text{E-}13 \text{ cm}^3/\text{s}$
strained GaP	HH 0.79	X <sub>xy</sub> 2		
	LH 0.14	X <sub>z</sub> 0.253	11.1	M <sub>b</sub> =31.4
		$\Gamma$ 0.13		
Wetting Layer	HH 0.51	X <sub>xy</sub> 1.3		
In <sub>0.1</sub> Ga <sub>0.9</sub> As	LH 0.082	X <sub>z</sub> 0.23	13.1	M <sub>b</sub> =28.8
		$\Gamma$ 0.067		
Bottom of QD	HH 0.51	X <sub>xy</sub> 1.3		
GaAs	LH 0.082	X <sub>z</sub> 0.23	12.9	M <sub>b</sub> =28.8
		$\Gamma$ 0.067		
Top of QD	HH 0.51	X <sub>xy</sub> 1.3		
In <sub>0.2</sub> Ga <sub>0.8</sub> As	LH 0.082	X <sub>z</sub> 0.23	13.2	M <sub>b</sub> =28.8
		$\Gamma$ 0.067		

M<sub>b</sub> is energy parameter for spontaneous radiative recombination calculation.

Table S4 General mobility of carriers in GaP and AlGaP

	$\alpha_{\text{rad}}$ (cm <sup>3</sup> /s)	Mobility of electron (cm <sup>2</sup> /Vs)	Mobility of hole (cm <sup>2</sup> /Vs)
GaP	10 <sup>-13</sup>	50	50
AlGaP	10 <sup>-13</sup>	50	10

For active region, mobilities are defined according to Equation 2–23 with  $v_{\text{th}}=10^7$  cm/s

Table S5 Temperature dependent trap density in AlGaP

Tem. (K)	Density (cm <sup>-3</sup> )	Active Energy (eV)
140	4.10 <sup>14</sup>	0.96
180	5.41.10 <sup>15</sup>	0.75
240	6.22.10 <sup>15</sup>	0.56
290	3.16.10 <sup>16</sup>	0.45

Table S 6 Temperature dependent trap density in the bottom of QDs

$\alpha_t$	10 <sup>-7</sup>
E <sub>a</sub> (eV)	0.34
Total trap density, D <sub>t,total</sub> (cm <sup>-3</sup> )	2.10 <sup>17</sup>



## Annex IV Experimental set-ups

For the KPFM measurements in section 3.2 and 4.1.2, HD-KPFM mode is enabled on a Nano-observer AFM microscope from CSInstruments (XLIM Lab.). HD-KPFM is an optimized single-pass mode using a second lock-in amplifier for topography and surface potential mapping in the same time.

For the KPFM measurements in section 3.3, a CombiScoop™ 1000 AFM is used, and the KPFM use a 2-pass technique in frequency modulation mode (GeePs Lab.). The tip is coated with Pt-Ir and has a radius below 25 nm, positioned by a laser of wavelength of 1300 nm. The set-up of AFM is shown in Figure S4.

For the J-V characterization, a solar simulator “Solarconstant PV275, ORIEL class A” and a Keithley 24XX were used in section 4.1 (XLIM Lab.). AM1.5G (IEC 60904-9 Edition 2) solar spectrum with  $100 \text{ mW/cm}^2$  was set using a certified monocrystalline silicon calibration. Solar cells were individually masked with an open area of  $0.2 \text{ cm}^2$ .

For the C-V measurements, a HP4192A ImpedanceMeter is used with 5 Hz to 13MHz frequency range and -35 to 35 V bias ranges (FOTON Lab.). The oscillator level was set to 30 mV.



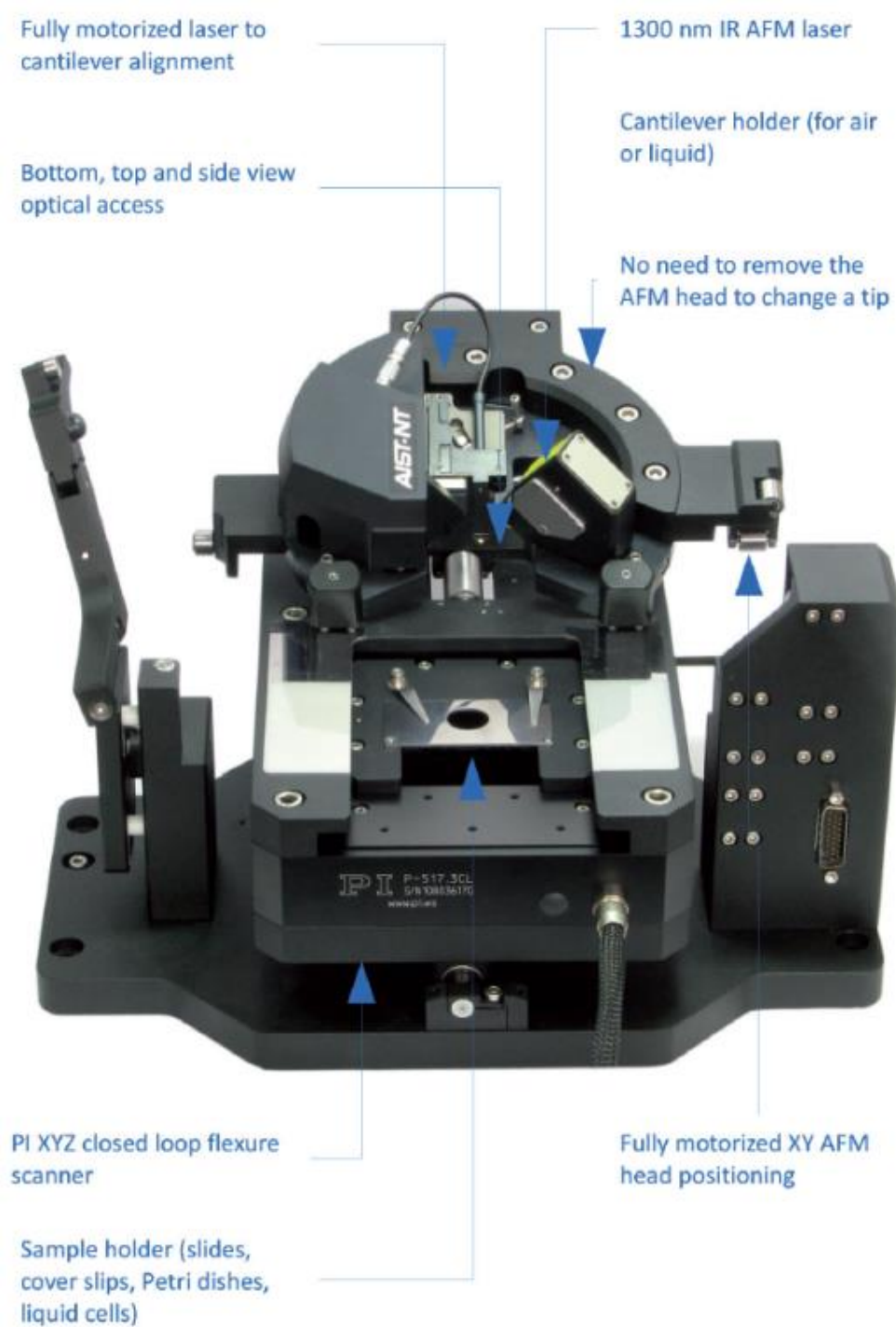


Figure S4 KPFM set-up (GeePs Lab.)



## Annex V Simulation of mobile MA ions

The MA cation migration reported by Yuan<sup>54</sup> is simulated in this section, by considering equivalent MA vacancy migration. Mobile ions redistribute under electrical poling, leading to a potential decrease of 320 meV in agreement with the experimental  $V_{CPD}$  variation<sup>54</sup> (Figure S5). The electrical field is 1.6 V/ $\mu\text{m}$  over a 47  $\mu\text{m}$ -wide MAPbI<sub>3</sub>. The poling electrodes are made of gold, corresponding to the contacts of WF of 5.1eV in the simulation. And the mobility of ions is fit as  $4 \cdot 10^{-10} \text{ cm}^2/\text{Vs}$ , which is closed to the reported value<sup>172</sup>. The ion density is fit as  $8 \cdot 10^{15} \text{ cm}^{-3}$ . Noticeably, some MA<sup>+</sup> ions, like donors gather at the gold/MAPbI<sub>3</sub> interface in static conditions, but the variation of potential here is not considerable. It is consistent with the previous hypothesis<sup>126</sup> of an effective n-type doping layer near gold in HTM-free PSCs.

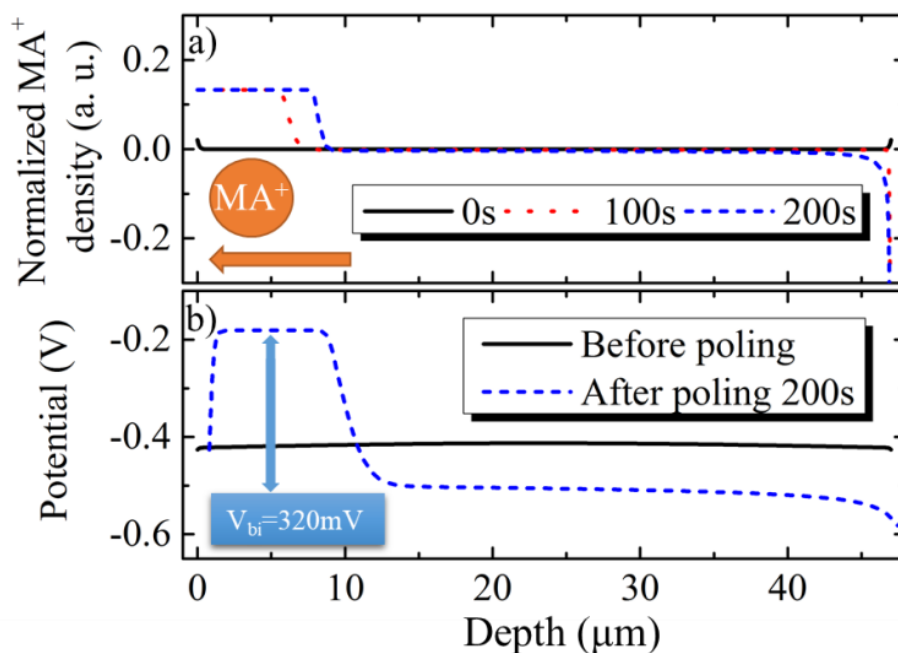


Figure S5 Simulated a) MA ion migration and b) potential profile before and after electrical poling







## Annex VI EL of QDs under high electric injection

The main emission peak shifts up to 1.8 eV under high continuous wave electrical injection, as shown in the Figure S6 a) and b). A slight redshift of 0.03eV is noticed, which might be related to an increase of the temperature up to 60 °C. In comparison with the serial resistance of the GaP and AlGaP based p-i-n diodes<sup>212</sup>, the large resistance (Figure S6 c)) in this work suggests that the bias mainly drops over the active regions. Therefore, the self-heating issue might be considerable, when the nano-size active regions work under high electrical injection and large bias. The total heat flux ( $J_{tot}$ ) generated inside the active regions is calculated as:

$$J_{tot} = S_{th}(T - T_{sink})/th_{GaP}$$

where  $th_{GaP}$  is the thickness of the GaP between the active regions and the thermal contact, namely the cathode. The thermal conductivity ( $S_{th}$ ) of bulk GaP is 1.1 W/cm°C. The heating energy is calculated to be  $4.4 \cdot 10^3$  W/cm<sup>2</sup>, which is 25% of the injection power. The self-heating might come from the Joule heating, the recombination or the generation heating. The thermal issue can also be the reason why the efficiency drop become significant when the current is larger than 0.6 kA/cm<sup>2</sup>. Moreover, such high heat energy can be a problem for integrated laser sources on silicon<sup>217</sup>. The origin of the high emission energy in this work is assumed to result from a competition between the transitions from X-like and  $\Gamma$ -like states to the HH VBM. Additional characterizations are needed, such as pressure-dependent EL. The direct  $\Gamma$  -  $\Gamma$  bandgap is indeed expected to blueshift with the increasing pressure, whereas the indirect X-  $\Gamma$  gap shall decrease<sup>218</sup>.



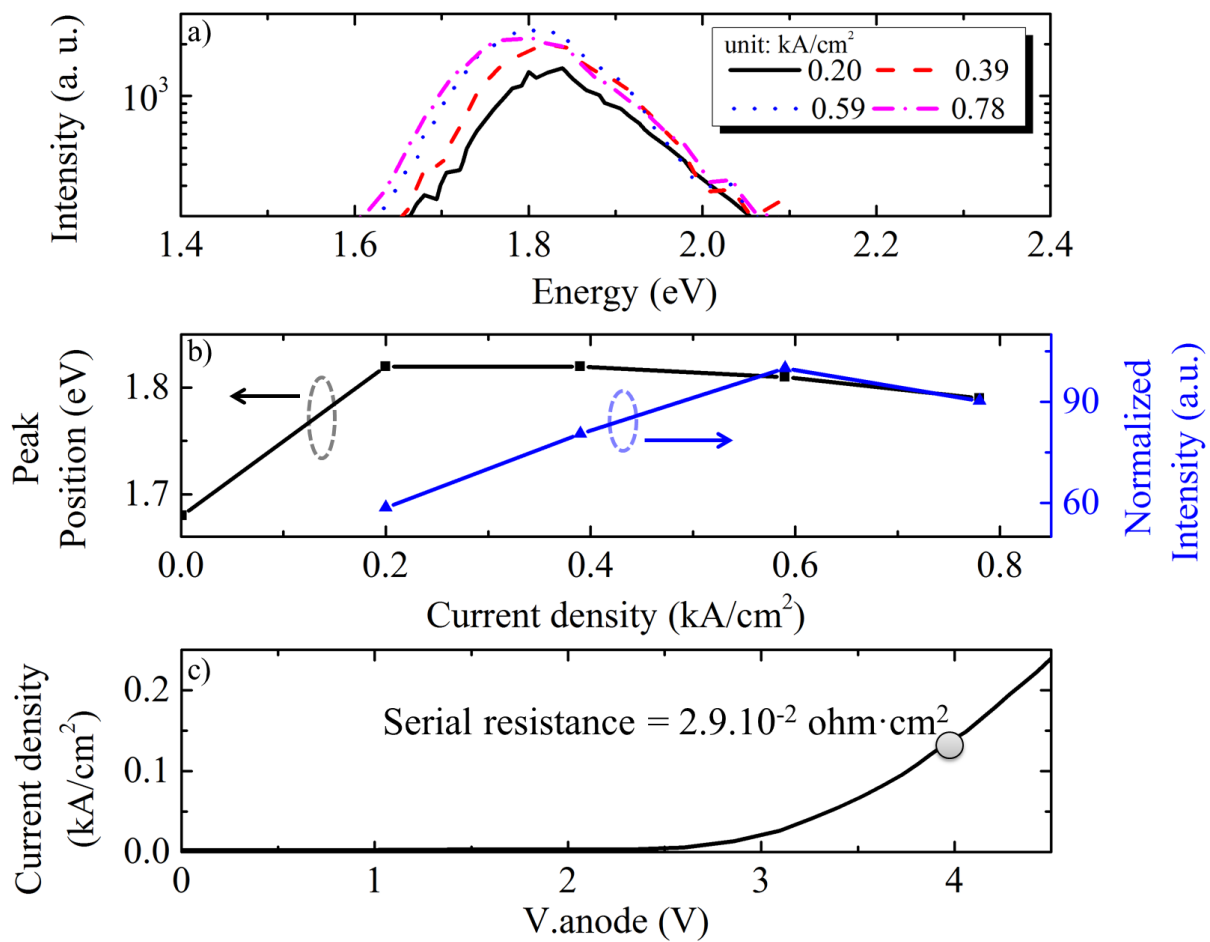


Figure S6 EL characteristics under high continue wave electrical injection.  
a) Experimental spectra and b) summary of the emission peak position and normalized intensity as a function of the injection current density. The peak position under low pulsed injection is added to indicate the emission shift from the low energy (1.6 eV) to high energy (>1.8 eV). c) J-V characteristics with a serial resistance deduced under bias of 3.96 V.





## Resumé

L'énergie solaire<sup>1</sup> est une des solutions qui pourrait satisfaire les besoins en énergie sur la terre<sup>2-4</sup> et dans l'espace<sup>5</sup>. A ce titre, le photovoltaïque (PV) est une branche stratégique des technologies de conversion de l'énergie solaire. C'est une énergie verte<sup>6</sup>, permettant la conversion directe photons-électrons. Dans ce domaine, la recherche sur les nouveaux types de cellules est très active et tend à converger vers des solutions énergétiques rentables, adaptées à une large diffusion sur le marché et à une utilisation efficace dans la société. A ce jour, comme le montre la Figure 1, les cellules les plus efficaces sont des cellules à quatre jonctions à base de GaAs<sup>9</sup> sous concentration avec un rendement de conversion photovoltaïque (PCE) de 46%, mais font appel à une technologie très coûteuse par rapport à la première génération de cellules à base de silicium. Aujourd'hui, l'efficacité record des cellules solaires à base de silicium (SSCs)<sup>10</sup> est de 25%. Ces dernières années ont vu la montée en puissance des cellules solaires à base de matériaux pérovskites (Perovskite Solar Cells : PSCs)<sup>12,13</sup>. Dans cette filière, un rendement de 20% a été obtenu en 2016 pour une cellule à base de FAPbI<sub>3</sub> (FA: formamidinium)<sup>11</sup> et un record de 22,7% a été atteint en novembre 2017. Il est remarquable de noter que le record des PSCs n'était que de 3,8% il y a huit ans<sup>15</sup>, alors qu'il a fallu plus de 40 ans pour que les SSCs monocristallins atteignent le record actuel de 26%.

### *Caractéristiques des cellules solaires pérovskites*

Comme on le voit sur la Figure 2, les matériaux à base de pérovskite aux halogénures (ABX<sub>3</sub>) partagent une structure cristalline similaire à celle de la pérovskite à oxyde minéral classique (ABO<sub>3</sub>). Le site du cation A est typiquement occupé par le cation de méthylammonium MA (ou FA), ou le cation inorganique Cs (ou Rb). Au stade actuel des progrès des PSCs, des alliages cationiques sont proposés pour améliorer la stabilité des absorbeurs de pérovskite<sup>16</sup>. En général, le plomb (Pb) se trouve sur le site B. Le site X est rempli d'atomes d'halogénure I, Br ou Cl. L'un des composés les plus étudiés est MAPbI<sub>3</sub>, qui sera le principal absorbeur de pérovskite considéré dans cette thèse.



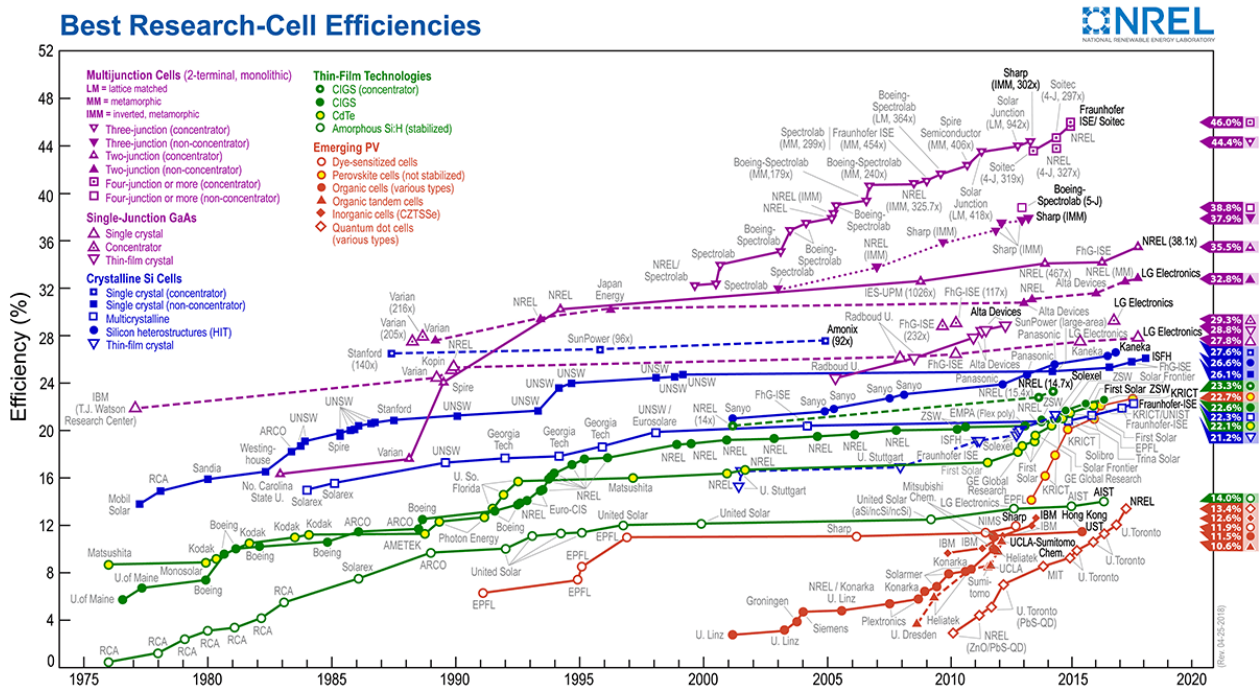


Figure 1 Efficacité des cellules de recherche au fil des années certifiée par NREL (04-25-2018)

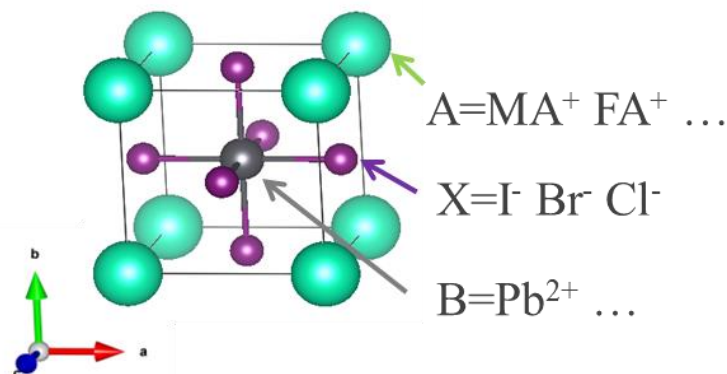



Figure 2 Structure cellulaire analogue à l'ABX<sub>3</sub> des absorbeurs de pérovskite aux halogénures. FA: cation formamidinium, MA: cation méthylammonium)

L'architecture des PSC n'a pas beaucoup évolué depuis l'introduction des premiers dispositifs<sup>25,26</sup> en 2012. En général, le substrat de verre est recouvert d'un oxyde conducteur transparent (TCO) sur lequel sont déposés successivement une couche du matériau de transport d'électrons (ETM) ou de trou (HTM), suivie de la couche absorbante pérovskite, et enfin de la couche HTM ou la couche ETM et un contact métallique; la première configuration (n-i-p) fait référence aux dispositifs standards et la dernière (p-i-n) aux dispositifs inversés. L'épaisseur de la couche de pérovskite est généralement de l'ordre de 350 nm, et la moitié de celle-ci pourrait être enveloppée par les méso-





porosités de  $\text{TiO}_x$  (un ETM classique)<sup>25</sup>. Idéalement, la couche absorbante de pérovskite est dopée de façon non intentionnelle les dopants étant totalement ionisés en régime statique (régime d'épuisement)<sup>27</sup>, ce qui entraîne un transport des porteurs dominé par la dérive. Les PSCs<sup>28,29</sup> déposés par des procédés relativement simples et peu coûteux<sup>31</sup> ont des performances élevées, rivalisant avec d'autres technologies établies telles que Si, CdTe voire même GaAs<sup>32,33</sup>. Les PSCs sont également intéressants en raison des nombreuses combinaisons possibles d'hétérojonctions<sup>34</sup>.


### ***Les défis des cellules solaires pérovskites***

Cependant, les dispositifs à bases de pérovskites montrent des instabilités dont les trois principales sont :

1. la sensibilité à l'humidité<sup>39</sup>;
2. la dégradation du photocourant( $J_{SC}$ ) se dégrade en fonction du temps lors du trempage léger<sup>40</sup>;
3. l'effet d'hystérésis sur la caractéristique courant-tension (J-V) des dispositifs qui dépend de la vitesse du balayage en tension lors de la mesure, du sens de la polarisation ainsi que de ses conditions préalables<sup>41</sup>.

Le premier problème peut être résolu en encapsulant les cellules ce qui empêche les réactions de la pérovskite avec l'eau et l'oxygène<sup>42</sup>. La deuxième source de dégradation de  $J_{SC}$  est supposée être causée par des pièges métastables associés à la MA<sup>40</sup> et peut être considérablement améliorée en utilisant des cations mixtes de pérovskites<sup>16,43-45</sup> et/ou de cellules en fonctionnement à basse température ou à faible polarisation externe<sup>40</sup>. Les performances des PSCs peuvent être restaurées après un repos dans l'obscurité, alors que les SSCs ne peuvent pas l'être après le vieillissement<sup>46</sup>. Le troisième problème, lié au phénomène d'hystérésis, peut être supprimé en remplaçant la couche d'ETM par une couche de PCBM<sup>40,47</sup> et/ou en modifiant l'interface ETM/pérovskite<sup>48-50</sup>, mais le mécanisme sous-jacent n'est à ce jour pas encore vraiment clarifié.





À la lumière des nombreux défis qui subsistent, l'application des PSCs pourrait être remise en question à plus long terme, même si les performances continuent de progresser. Si l'on considère les PSCs à l'échelle nanométrique plutôt que les SSCs à micro-échelle, la caractérisation et la modélisation à l'échelle nanométrique sont encore plus critiques qu'auparavant pour une meilleure compréhension du fonctionnement des dispositifs. De plus, cela pourrait permettre d'ouvrir des voies vers d'autres applications telles que les diodes électroluminescente<sup>72</sup>, les lasers<sup>73</sup>, les dispositifs synaptiques<sup>74</sup>, les dispositifs de mémoire<sup>75</sup> ou les détecteurs<sup>76</sup> de rayons X par exemple.

### ***Besoins en caractérisation et en modélisation à l'échelle nanométrique***

Depuis l'invention du microscope à balayage à effet tunnel (STM) en 1986, une nouvelle famille de techniques de microscopie appelée "Scanning Probe Microscopy" (SPM) se développe. elle permet aujourd'hui d'accéder à des observations précises de surface à l'échelle nanométrique<sup>79</sup>. De ce point de vue, une des techniques les plus attractives est la Microscopie à Force Atomique (AFM), qui utilise les forces entre la pointe sonde et l'échantillon et permet de prendre une photo tridimensionnelle (3D) de la surface du matériau à l'échelle nanométrique. Le mouvement de la pointe AFM est surveillé par un photodétecteur, qui peut enregistrer la réflexion d'un faisceau laser sur la pointe. Comparée à la technique STM, l'AFM n'est pas limitée à la mesure sur une surface électriquement conductrice. Basé sur l'invention de l'AFM en 1986 par G. Binnig, C. Gerber et C.F. Quate<sup>80</sup>, une autre extension très intéressante est apparue et a permis la mesure du potentiel de surface à l'échelle nanométrique en 1991. Cette technique : Kelvin Probe Force Microscopy (KPFM)<sup>81</sup> permet la mesure des profils de potentiels et ainsi les prédictions des performances des cellules solaires<sup>70,82-84</sup> et des lasers<sup>85</sup>, la mesure des niveaux d'énergie<sup>86,87</sup> et des discontinuités de bandes aux hétérojonctions<sup>88,89</sup>. Le principe en est le suivant : après que la topographie de la surface a été étudiée par AFM, la distance entre la pointe et la surface de l'échantillon est maintenue constante pour ressentir la force. Le potentiel de surface ( $\Psi_s$ ) des échantillons peut par conséquent être déduit connaissant le travail de sortie (WF) de la pointe. Cependant, en raison de nombreux artefacts sur la surface, il est difficile d'en déduire une analyse quantitative du potentiel global ( $\Psi$ ). Et ce potentiel est en outre fortement lié au fonctionnement et aux performances du dispositif. De ce fait, la conception de simulations pour interpréter les mesures KPFM est primordial et fait l'objet d'une partie importante de ce mémoire. Les améliorations techniques des mesures KPFM sont toujours en cours et la mo-



délisation à l'échelle nanométrique sera indispensable pour faire progresser dans la compréhension et dans l'analyse de cette technique<sup>90</sup>.

## Théorie et objectifs

La figure 3 montre schématiquement le principe de la simulation numérique mise en œuvre. Les points principaux sont : le calcul du potentiel électrostatique et des pseudo-niveaux de fermi, la prise en compte des phénomènes de génération-recombinaison, la simulation de l'effet tunnel, la prise en compte de la migration éventuelle d'ions mobiles, et enfin l'effet de la température.

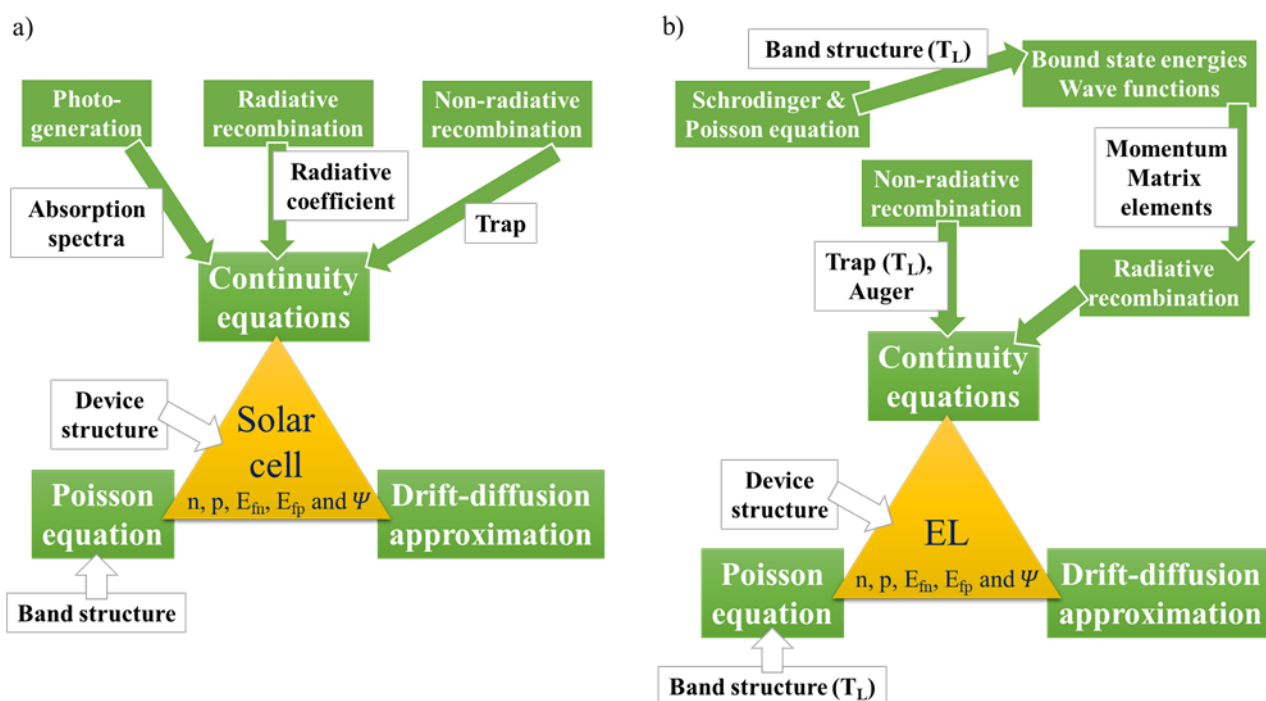


Figure 3 Simulation numérique a) cellules solaires et b) électroluminescence (EL). Les paramètres d'entrée et les résultats sont indiqués respectivement en carrés ouverts et solides.  $T_L$  entre parenthèses indique les paramètres dépendant de la température.

## KPFM et modélisation

Une nouvelle approche de la modélisation de KPFM (Figure 4) pour les hétérostructures dans l'obscurité et sous illumination est développée. La présence d'états de surface au sommet des couches de  $TiO_x$  est mise en évidence en corrélant les calculs théoriques et les résultats expérimentaux. Les caractéristiques de base des mesures KPFM sous éclaircissement, à savoir le photo-potentiel de surface,



sont simulées et permettent de déduire la bande d'énergie interdite. Cette approche est utilisée pour étudier le potentiel le long de la section transversale de jonctions diffusées à base de silicium et des PSCs à base de  $\text{TiO}_x$  méso poreux.

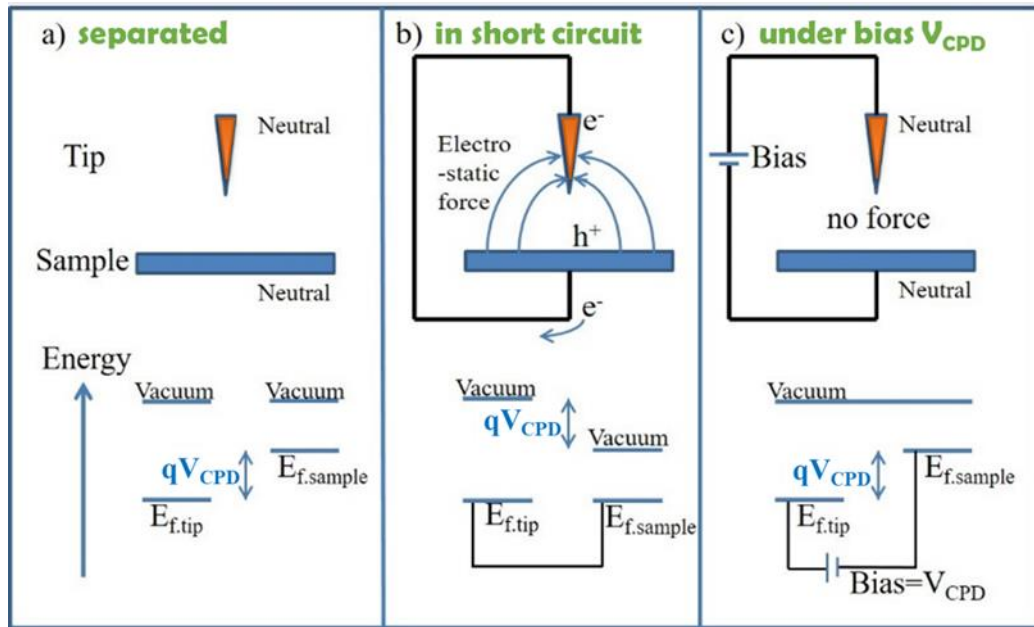


Figure 4 Illustration de la configuration de base de KPFM. CPD est le nom abrégé de la différence de potentiel de contact. La pointe et l'échantillon sont a) séparés, b) connectés en court-circuit et c) sous polarisation externe égale à  $V_{CPD}$ .

### *Etude des PSCs*

Les PSCs sont étudiés expérimentalement et théoriquement dans leur structure classique, ainsi qu'inversée, à base de  $\text{TiO}_x$  et imprimables à base de  $\text{WO}_x$ . Les caractérisations étudiées comprennent les mesures courant-tension (J-V), capacité-tension (C-V) ainsi que KPFM. Ces caractéristiques électriques sont simulées pour analyser les pertes en tension de circuit ouvert  $V_{OC}$  ainsi que l'effet d'hystérésis<sup>102</sup> (Figure 5) et la dégradation réversible du photocourant<sup>40</sup>.



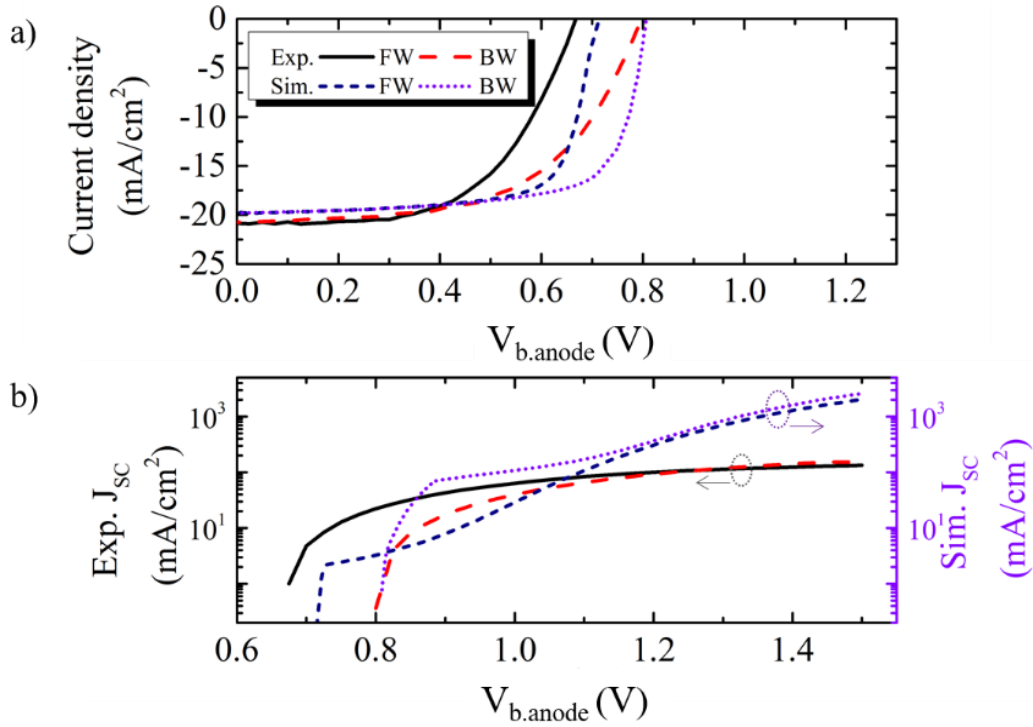


Figure 5 Caractéristiques J-V expérimentales et simulées des cellules solaires en WO<sub>x</sub>/MAPbI<sub>3</sub>/Spiro-OMeTAD.

### *Jonctions tunnel dans des cellules de type tandem PSC/SSCs*

Les jonctions tunnel à base de silicium sont numériquement étudiées pour des cellules solaires à base de pérovskites/silicium de type tandem. En effet dans ce type de cellules, la connexion électrique entre la cellule à base de pérovskite et la cellule silicium se fait par le biais d'une jonction tunnel au niveau de la cellule silicium. L'alignement de bande associé est représenté Figure 6. L'influence du niveau de dopage dans la jonction tunnel est étudiée. Les caractéristiques J-V des cellules solaires à simple jonction et des cellules en tandem sont calculées et présentées figure 7.



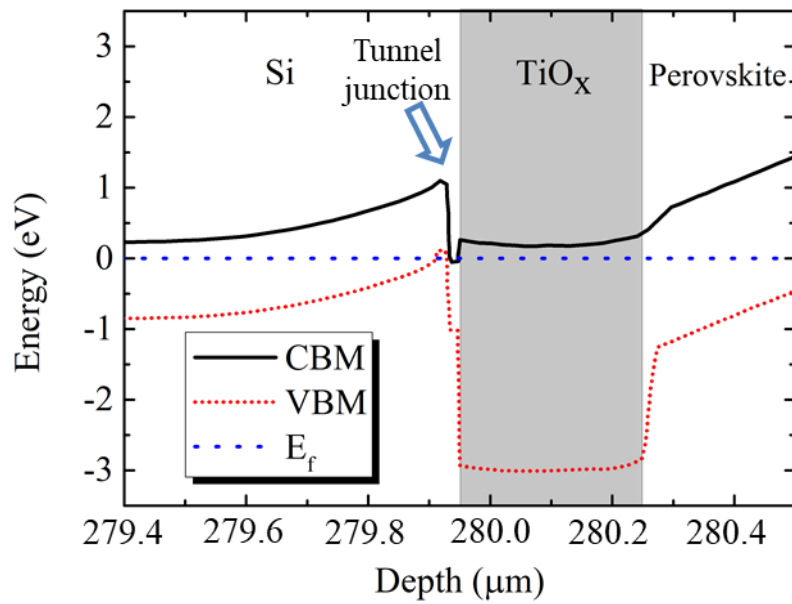


Figure 6 Schéma de bande des cellules solaires de type tandem à l'équilibre thermodynamique. Les niveaux de dopage n+ et p+ dans la jonction tunnel sont égaux à  $5.10^{19} \text{ cm}^{-3}$ .

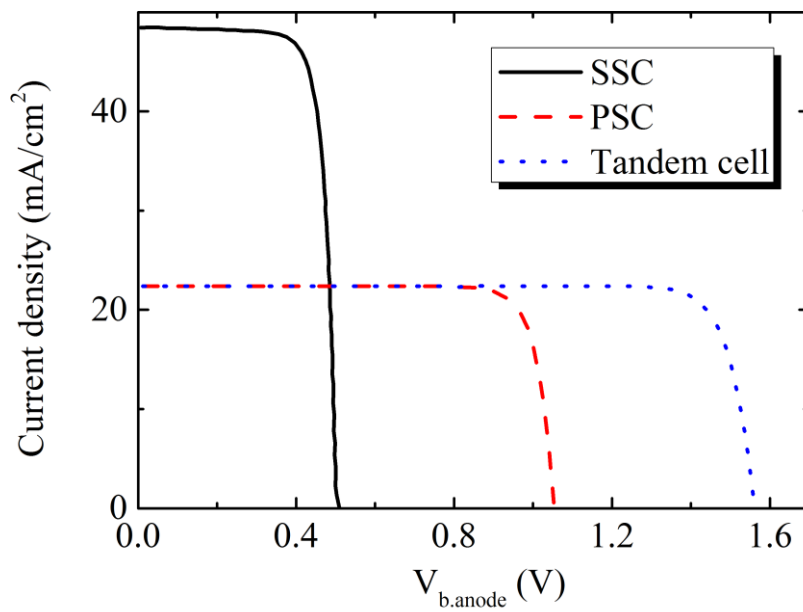


Figure 7 J-V caractéristiques des cellules individuelles : pérovskite (PSC), silicium (SSC) et de la cellule tandem.



## Propriétés électriques de structures à base de QDs III-V/GaP pour l'émission de lumière sur silicium

Des dispositifs basés sur 5 couches de QDs de (In,Ga)As/GaP sont étudiés expérimentalement et théoriquement sous injection électrique. Le décalage vers le rouge du pic d'émission et l'extinction thermique de l'intensité de l'électroluminescence (EL) sont simulés en fonction de la température (Figure 8), en tenant compte de l'alignement de la bande et des pièges dans les régions actives. Le transport la recombinaison des porteurs dans la structure quantique est calculé et discutés.

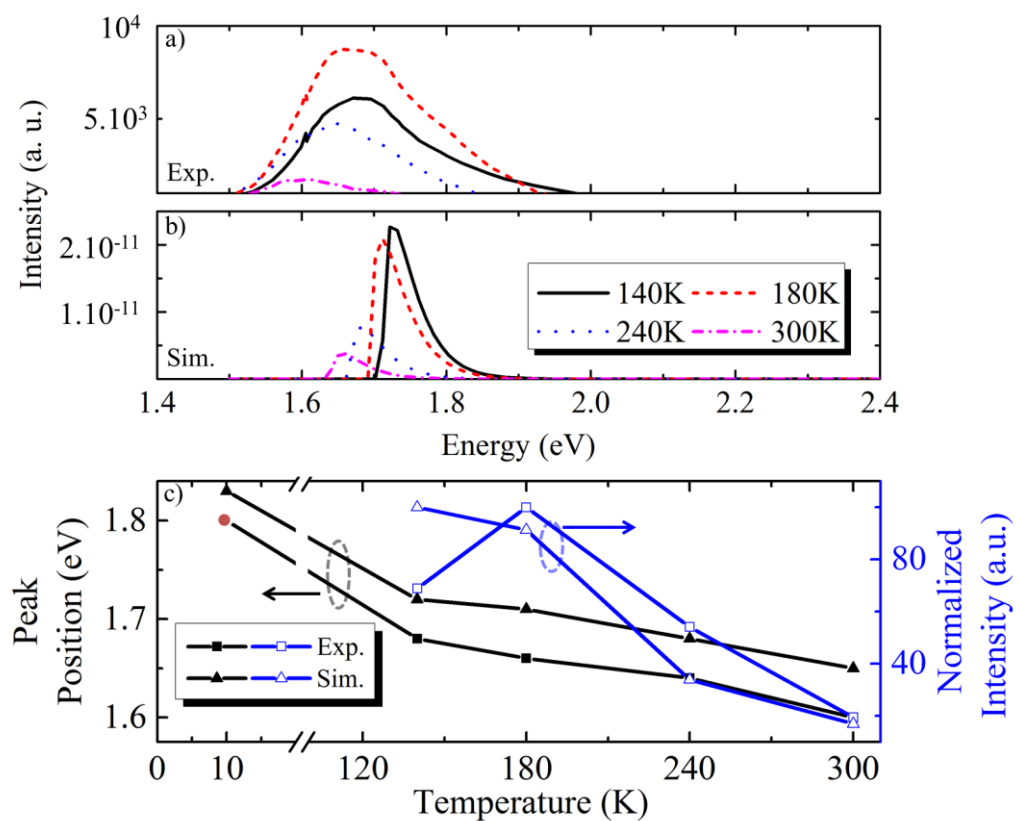


Figure 8 spectres EL a) expérimentaux et b) calculés sous faible injection électrique. La densité de courant d'injection est de  $1 \text{ A/cm}^2$ . c) position du pic d'émission et de l'intensité normalisée en fonction de la température du contact thermique. Le point rouge représente le rapport de l'énergie maximale d'émission à 10 K pour les QDs de (In, Ga)As/GaP<sup>208</sup>.







## References

1. Solargis. GHI Solar Map. (2017). Available at: <http://solargis.com/products/maps-and-gis-data/free/overview/>. (Accessed: 28th November 2017)
2. Sahu, A., Yadav, N. & Sudhakar, K. Floating photovoltaic power plant: A review. *Renew. Sustain. Energy Rev.* **66**, 815–824 (2016).
3. Modi, A., Bühler, F., Andreasen, J. G. & Haglind, F. A review of solar energy based heat and power generation systems. *Renew. Sustain. Energy Rev.* **67**, 1047–1064 (2017).
4. The World Factbook — Central Intelligence Agency. Available at: <https://www.cia.gov/library/publications/the-world-factbook/geos/xx.html>. (Accessed: 28th November 2017)
5. Friedman, L. *Starsailing, solar sails and interstellar travel*. (1988).
6. IPCC Fifth Assessment Report. Available at: <https://www.ipcc.ch/report/ar5/mindex.shtml>. (Accessed: 22nd November 2017)
7. Fritts, C. E. On a new form of selenium cell, and some electrical discoveries made by its use. *Am. J. Sci.* **s3-26**, 465–472 (1883).
8. Hybrid Perovskite Solar Cells: the Genesis and Early Developments 2009-2014 – Fundacio Scito.
9. NREL Efficiency Chart Rev. 11-02-2016. *NREL Efficiency Chart Rev.* (2016). Available at: [http://www.nrel.gov/ncpv/images/efficiency\\_chart.jpg](http://www.nrel.gov/ncpv/images/efficiency_chart.jpg).
10. Cousins, P. J. *et al.* Generation 3: Improved performance at lower cost. in 000275–000278 (IEEE, 2010). doi:10.1109/PVSC.2010.5615850
11. International Energy Agency. World Energy Outlook 2017. Available at: <https://www.iea.org/weo2017/>. (Accessed: 22nd November 2017)
12. Grätzel, M. The Rise of Highly Efficient and Stable Perovskite Solar Cells. *Acc. Chem. Res.* **50**, 487–491 (2017).
13. Zhang, W., Eperon, G. E. & Snaith, H. J. Metal halide perovskites for energy applications. *Nat. Energy* **1**, 16048 (2016).
14. Yang, W. S. *et al.* High-performance photovoltaic perovskite layers fabricated through intramolecular exchange. *Science* **348**, 1234–1237 (2015).
15. Kojima, A., Teshima, K., Shirai, Y. & Miyasaka, T. Organometal Halide Perovskites as Visible-Light Sensitizers for Photovoltaic Cells. *J. Am. Chem. Soc.* **131**, 6050–6051 (2009).



16. Saliba, M. *et al.* Incorporation of rubidium cations into perovskite solar cells improves photovoltaic performance. *Science* **354**, 206–209 (2016).
17. Hauck, M., Ligthart, T., Schaap, M., Boukris, E. & Brouwer, D. Environmental benefits of reduced electricity use exceed impacts from lead use for perovskite based tandem solar cell. *Renew. Energy* **111**, 906–913 (2017).
18. Babayigit, A., Ethirajan, A., Muller, M. & Conings, B. Toxicity of organometal halide perovskite solar cells. *Nat. Mater.* **15**, 247–251 (2016).
19. Chen, P.-Y. *et al.* Environmentally responsible fabrication of efficient perovskite solar cells from recycled car batteries. *Energy Env. Sci* **7**, 3659–3665 (2014).
20. Filip, M. R. & Giustino, F. Computational Screening of Homovalent Lead Substitution in Organic–Inorganic Halide Perovskites. *J. Phys. Chem. C* **120**, 166–173 (2016).
21. Filip, M. R., Hillman, S., Haghighirad, A. A., Snaith, H. J. & Giustino, F. Band Gaps of the Lead-Free Halide Double Perovskites Cs<sub>2</sub>BiAgCl<sub>6</sub> and Cs<sub>2</sub>BiAgBr<sub>6</sub> from Theory and Experiment. *J. Phys. Chem. Lett.* **7**, 2579–2585 (2016).
22. Even, J., Pedesseau, L. & Katan, C. Analysis of Multivalley and Multibandgap Absorption and Enhancement of Free Carriers Related to Exciton Screening in Hybrid Perovskites. *J. Phys. Chem. C* **118**, 11566–11572 (2014).
23. Fang, H.-H. *et al.* Photoexcitation dynamics in solution-processed formamidinium lead iodide perovskite thin films for solar cell applications. *Light Sci. Appl.* **5**, e16056–e16056 (2016).
24. Miyata, A. *et al.* Direct measurement of the exciton binding energy and effective masses for charge carriers in organic–inorganic tri-halide perovskites. *Nat. Phys.* **11**, 582–587 (2015).
25. Lee, M. M., Teuscher, J., Miyasaka, T., Murakami, T. N. & Snaith, H. J. Efficient Hybrid Solar Cells Based on Meso-Superstructured Organometal Halide Perovskites. *Science* **338**, 643–647 (2012).
26. Kim, H.-S. *et al.* Lead Iodide Perovskite Sensitized All-Solid-State Submicron Thin Film Mesoscopic Solar Cell with Efficiency Exceeding 9%. *Sci. Rep.* **2**, (2012).
27. Laban, W. A. & Etgar, L. Depleted hole conductor-free lead halide iodide heterojunction solar cells. *Energy Environ. Sci.* **6**, 3249 (2013).
28. Abanades, J. C., Rubin, E. S., Mazzotti, M. & Herzog, H. J. On the climate change mitigation potential of CO<sub>2</sub> conversion to fuels.



- Energy Environ. Sci.* (2017).  
doi:10.1039/C7EE02819A
29. Needleman, D. B. *et al.* Economically sustainable scaling of photovoltaics to meet climate targets. *Energy Environ. Sci.* **9**, 2122–2129 (2016).
  30. Ball, J. M. & Petrozza, A. Defects in perovskite-halides and their effects in solar cells. *Nat. Energy* **1**, 16149 (2016).
  31. Nie, W. *et al.* High-efficiency solution-processed perovskite solar cells with millimeter-scale grains. *Science* **347**, 522–525 (2015).
  32. Green, M. A. *et al.* Solar cell efficiency tables (version 50). *Prog. Photovolt. Res. Appl.* **25**, 668–676 (2017).
  33. Polman, A., Knight, M., Garnett, E. C., Ehrler, B. & Sinke, W. C. Photovoltaic materials: Present efficiencies and future challenges. *Science* **352**, aad4424–aad4424 (2016).
  34. Gao, P., Grätzel, M. & Nazeeruddin, M. K. Organohalide lead perovskites for photovoltaic applications. *Energy Environ. Sci.* **7**, 2448 (2014).
  35. Dymshits, A., Rotem, A. & Etgar, L. High voltage in hole conductor free organo metal halide perovskite solar cells. *J Mater Chem A* **2**, 20776–20781 (2014).
  36. Dong, P. *et al.* A deep-level transient spectroscopy study of gamma-ray irradiation on the passivation properties of silicon nitride layer on silicon. *AIP Adv.* **7**, 085112 (2017).
  37. *Nanoelectronics and Materials Development*. (InTech, 2016). doi:10.5772/61560
  38. Correa-Baena, J.-P. *et al.* Promises and challenges of perovskite solar cells. *Science* **358**, 739–744 (2017).
  39. Venkatesan, S. *et al.* Moisture-driven phase transition for improved perovskite solar cells with reduced trap-state density. *Nano Res.* **10**, 1413–1422 (2017).
  40. Nie, W. *et al.* Light-activated photocurrent degradation and self-healing in perovskite solar cells. *Nat. Commun.* **7**, 11574 (2016).
  41. Snaith, H. J. *et al.* Anomalous Hysteresis in Perovskite Solar Cells. *J. Phys. Chem. Lett.* **5**, 1511–1515 (2014).
  42. You, J. *et al.* Improved air stability of perovskite solar cells via solution-processed metal oxide transport layers. *Nat. Nanotechnol.* **11**, 75–81 (2016).
  43. Duong, T. *et al.* Rubidium Multication Perovskite with Optimized Bandgap for Perovskite-Silicon Tandem with over 26% Efficiency. *Adv. Energy Mater.* **7**, 1700228 (2017).
  44. McMeekin, D. P. *et al.* A mixed-cation lead mixed-halide perovskite absorber for tandem solar cells. *Science* **351**, 151–155 (2016).



45. Bi, D. *et al.* Efficient luminescent solar cells based on tailored mixed-cation perovskites. *Sci. Adv.* **2**, e1501170–e1501170 (2016).
46. Kwapil, W., Niewelt, T. & Schubert, M. C. Kinetics of carrier-induced degradation at elevated temperature in multicrystalline silicon solar cells. *Sol. Energy Mater. Sol. Cells* **173**, 80–84 (2017).
47. Chiang, C.-H. & Wu, C.-G. Bulk heterojunction perovskite–PCBM solar cells with high fill factor. *Nat. Photonics* **10**, 196–200 (2016).
48. Calado, P. *et al.* Evidence for ion migration in hybrid perovskite solar cells with minimal hysteresis. *Nat. Commun.* **7**, 13831 (2016).
49. Xiao, C. *et al.* Nanometer-scale electrical potential profiling across perovskite solar cells. in 1197–1201 (IEEE, 2016). doi:10.1109/PVSC.2016.7749804
50. Grancini, G. *et al.* One-Year stable perovskite solar cells by 2D/3D interface engineering. *Nat. Commun.* **8**, 15684 (2017).
51. Meloni, S. *et al.* Ionic polarization-induced current–voltage hysteresis in CH<sub>3</sub>NH<sub>3</sub>PbX<sub>3</sub> perovskite solar cells. *Nat. Commun.* **7**, 10334 (2016).
52. Hu, J. *et al.* Photovoltage Behavior in Perovskite Solar Cells under Light-Soaking Showing Photoinduced Interfacial Changes. *ACS Energy Lett.* **2**, 950–956 (2017).
53. Ravishankar, S. *et al.* Surface Polarization Model for the Dynamic Hysteresis of Perovskite Solar Cells. *J. Phys. Chem. Lett.* (2017). doi:10.1021/acs.jpclett.7b00045
54. Yuan, Y. *et al.* Photovoltaic Switching Mechanism in Lateral Structure Hybrid Perovskite Solar Cells. *Adv. Energy Mater.* **5**, 1500615 (2015).
55. Yuan, Y. *et al.* Electric-Field-Driven Reversible Conversion Between Methylammonium Lead Triiodide Perovskites and Lead Iodide at Elevated Temperatures. *Adv. Energy Mater.* **6**, 1501803 (2016).
56. Domanski, K. *et al.* Migration of cations induces reversible performance losses over day/night cycling in perovskite solar cells. *Energy Env. Sci* **10**, 604–613 (2017).
57. Mishra, A. K., Catalan, J., Camacho, D., Martinez, M. & Hodges, D. Evaluation of physics-based numerical modelling for diverse design architecture of perovskite solar cells. *Mater. Res. Express* **4**, 085906 (2017).
58. Alnuaimi, A., Almansouri, I. & Nayfeh, A. Effect of mobility and band structure of hole transport layer in planar heterojunction perovskite solar cells using 2D TCAD simulation. *J. Comput. Electron.* **15**, 1110–1118 (2016).
59. Zhou, Q. *et al.* Two-dimensional device modeling of CH<sub>3</sub>NH<sub>3</sub>PbI<sub>3</sub> based planar hetero-



- p>junction perovskite solar cells.
- Sol. Energy*
- 123**
- , 51–56 (2016).
60. Minemoto, T. & Murata, M. Theoretical analysis on effect of band offsets in perovskite solar cells. *Sol. Energy Mater. Sol. Cells* **133**, 8–14 (2015).
  61. Set, Y. T., Zhang, T., Birgersson, E. & Luther, J. What parameters can be reliably deduced from the current-voltage characteristics of an organic bulk-heterojunction solar cell? *J. Appl. Phys.* **117**, 084503 (2015).
  62. Yang, W., Yao, Y. & Wu, C.-Q. Origin of the high open circuit voltage in planar heterojunction perovskite solar cells: Role of the reduced bimolecular recombination. *J. Appl. Phys.* **117**, 095502 (2015).
  63. Sun, X., Asadpour, R., Nie, W., Mohite, A. D. & Alam, M. A. A Physics-Based Analytical Model for Perovskite Solar Cells. *IEEE J. Photovolt.* **5**, 1389–1394 (2015).
  64. Tress, W. *et al.* Understanding the rate-dependent J–V hysteresis, slow time component, and aging in CH<sub>3</sub>NH<sub>3</sub>PbI<sub>3</sub> perovskite solar cells: the role of a compensated electric field. *Energy Environ. Sci.* **8**, 995–1004 (2015).
  65. Huang, Y. *et al.* Numerical simulation of HTM-free and WO<sub>x</sub> based perovskite cells: Effects of interface conditions. in 29–30 (IEEE, 2017). doi:10.1109/NUSOD.2017.8009975
  66. van Reenen, S., Kemerink, M. & Snaith, H. J. Modeling Anomalous Hysteresis in Perovskite Solar Cells. *J. Phys. Chem. Lett.* **6**, 3808–3814 (2015).
  67. Almosni, S. *et al.* Tunneling-Assisted Trapping as one of the Possible Mechanisms for the Origin of Hysteresis in Perovskite Solar Cells. *Energy Technol.* **5**, 1767–1774 (2017).
  68. Richardson, G. *et al.* Can slow-moving ions explain hysteresis in the current–voltage curves of perovskite solar cells? *Energy Environ. Sci.* **9**, 1476–1485 (2016).
  69. Gottesman, R. *et al.* Dynamic Phenomena at Perovskite/Electron-Selective Contact Interface as Interpreted from Photovoltage Decays. *Chem* **1**, 776–789 (2016).
  70. Bergmann, V. W. *et al.* Local Time-Dependent Charging in a Perovskite Solar Cell. *ACS Appl. Mater. Interfaces* **8**, 19402–19409 (2016).
  71. Jiang, C.-S. *et al.* Carrier separation and transport in perovskite solar cells studied by nanometre-scale profiling of electrical potential. *Nat. Commun.* **6**, 8397 (2015).
  72. Xiao, Z. *et al.* Efficient perovskite light-emitting diodes featuring nanometre-sized crystallites. *Nat. Photonics* **11**, 108–115 (2017).



73. Harwell, J. R., Whitworth, G. L., Turnbull, G. A. & Samuel, I. D. W. Green Perovskite Distributed Feedback Lasers. *Sci. Rep.* **7**, (2017).
74. Xiao, Z. & Huang, J. Energy-Efficient Hybrid Perovskite Memristors and Synaptic Devices. *Adv. Electron. Mater.* **2**, 1600100 (2016).
75. Gu, C. & Lee, J.-S. Flexible Hybrid Organic–Inorganic Perovskite Memory. *ACS Nano* **10**, 5413–5418 (2016).
76. Kim, Y. C. *et al.* Printable organometallic perovskite enables large-area, low-dose X-ray imaging. *Nature* **550**, 87–91 (2017).
77. Zhang, Z. *et al.* Perovskite nickelates as electric-field sensors in salt water. *Nature* **553**, 68–72 (2017).
78. Binnig, G. & Rohrer, H. Scanning tunneling microscopy—from birth to adolescence. *Rev. Mod. Phys.* **59**, 615–625 (1987).
79. Bhushan, B. & Marti, O. Scanning Probe Microscopy—Principle of Operation, Instrumentation, and Probes. in *Nanotribology and Nanomechanics* (ed. Bhushan, B.) 33–93 (Springer International Publishing, 2017). doi:10.1007/978-3-319-51433-8\_2
80. Binnig, G., Quate, C. F. & Gerber, C. Atomic Force Microscope. *Phys. Rev. Lett.* **56**, 930–933 (1986).
81. Rosenwaks, P. Y. *et al.* Kelvin Probe Force Microscopy of Semiconductors. in *Scanning Probe Microscopy* (eds. Kalinin, S. & Gruverman, A.) 663–689 (Springer New York, 2007). doi:10.1007/978-0-387-28668-6\_25
82. Garrett, J. L. *et al.* Real-Time Nanoscale Open-Circuit Voltage Dynamics of Perovskite Solar Cells. *Nano Lett.* (2017). doi:10.1021/acs.nanolett.7b00289
83. Chen, Y.-J. *et al.* Insight into interfaces and junction of polycrystalline silicon solar cells by kelvin probe force microscopy. *Nano Energy* **36**, 303–312 (2017).
84. Challinger, S. E., Baikie, I. D., Harwell, J. R., Turnbull, G. A. & Samuel, I. D. W. An Investigation of the Energy Levels within a Common Perovskite Solar Cell Device and a Comparison of DC/AC Surface Photovoltage Spectroscopy Kelvin Probe Measurements of Different MAPBI3 Perovskite Solar Cell Device Structures. *MRS Adv.* 1–7 (2017). doi:10.1557/adv.2017.72
85. González, Y., Abelenda, A. & Sánchez, M. Surface photovoltage spectroscopy characterization of AlGaAs/GaAs laser structures. *J. Phys. Conf. Ser.* **792**, 012021 (2017).
86. Kitaura, M. *et al.* Energy location of Ce <sup>3+</sup> 4f level and majority carrier type in Gd<sub>3</sub>Al<sub>2</sub>Ga<sub>3</sub>O<sub>12</sub>:Ce crystals studied by surface photovoltage spectroscopy. *Appl. Phys. Lett.* **110**, 251101 (2017).



87. Harwell, J. R. *et al.* Probing the energy levels of perovskite solar cells via Kelvin probe and UV ambient pressure photoemission spectroscopy. *Phys Chem Chem Phys* **18**, 19738–19745 (2016).
88. Singh, S. D., Porwal, S., Sinha, A. K. & Ganguli, T. Surface photovoltage spectroscopy of an epitaxial ZnO/GaP heterojunction. *Semicond. Sci. Technol.* **32**, 055005 (2017).
89. Minj, A. *et al.* Surface properties of AlIn-GaN/GaN heterostructure. *Mater. Sci. Semicond. Process.* **55**, 26–31 (2016).
90. Robert, C. *et al.* Electronic wave functions and optical transitions in (In,Ga)As/GaP quantum dots. *Phys. Rev. B* **94**, (2016).
91. Singh, J. *Electronic and Optoelectronic Properties of Semiconductor Structures*. (Cambridge University Press, 2007).
92. Silvaco Inc. ATLAS user's manual. (2012).
93. Bludau, W., Onton, A. & Heinke, W. Temperature dependence of the band gap of silicon. *J. Appl. Phys.* **45**, 1846–1848 (1974).
94. Zhao, J., Wang, A., Green, M. A. & Ferrazza, F. 19.8% efficient “honeycomb” textured multicrystalline and 24.4% monocrystalline silicon solar cells. *Appl. Phys. Lett.* **73**, 1991–1993 (1998).
95. Paetzold, U. W. *et al.* Plasmonic reflection grating back contacts for microcrystalline silicon solar cells. *Appl. Phys. Lett.* **99**, 181105 (2011).
96. Chen, Z. *et al.* High-Performance Color-Tunable Perovskite Light Emitting Devices through Structural Modulation from Bulk to Layered Film. *Adv. Mater.* **29**, 1603157 (2017).
97. Blancon, J.-C. *et al.* The Effects of Electronic Impurities and Electron-Hole Recombination Dynamics on Large-Grain Organic-Inorganic Perovskite Photovoltaic Efficiencies. *Adv. Funct. Mater.* **26**, 4283–4292 (2016).
98. Stranks, S. D. *et al.* Recombination Kinetics in Organic-Inorganic Perovskites: Excitons, Free Charge, and Subgap States. *Phys. Rev. Appl.* **2**, 034007 (2014).
99. Varshni, Y. P. Temperature dependence of the energy gap in semiconductors. *Physica* **34**, 149–154 (1967).
100. Kronik, L. Surface photovoltage phenomena: theory, experiment, and applications. *Surf. Sci. Rep.* **37**, 1–206 (1999).
101. Barnea-Nehoshtan, L., Kirmayer, S., Edri, E., Hodes, G. & Cahen, D. Surface Photovoltage Spectroscopy Study of Organo-Lead Perovskite Solar Cells. *J. Phys. Chem. Lett.* **5**, 2408–2413 (2014).
102. Gheno, A. *et al.* Printable WO<sub>3</sub> electron transporting layer for perovskite solar cells:



- Influence on device performance and stability. *Sol. Energy Mater. Sol. Cells* **161**, 347–354 (2017).
103. Sadewasser, S. & Glatzel, T. *Kelvin Probe Force Microscopy - Measuring and Compensating* / Sascha Sadewasser / Springer.
  104. Kronik, L. Surface photovoltage phenomena: theory, experiment, and applications. *Surf. Sci. Rep.* **37**, 1–206 (1999).
  105. Tang, H., Prasad, K., Sanjinès, R., Schmid, P. E. & Lévy, F. Electrical and optical properties of TiO<sub>2</sub> anatase thin films. *J. Appl. Phys.* **75**, 2042–2047 (1994).
  106. Rühle, S. & Cahen, D. Electron Tunneling at the TiO<sub>2</sub>/Substrate Interface Can Determine Dye-Sensitized Solar Cell Performance. *J. Phys. Chem. B* **108**, 17946–17951 (2004).
  107. Snaith, H. J. & Grätzel, M. The Role of a “Schottky Barrier” at an Electron-Collection Electrode in Solid-State Dye-Sensitized Solar Cells. *Adv. Mater.* **18**, 1910–1914 (2006).
  108. Dymshits, A., Henning, A., Segev, G., Rosenwaks, Y. & Etgar, L. The electronic structure of metal oxide/organo metal halide perovskite junctions in perovskite based solar cells. *Sci. Rep.* **5**, 8704 (2015).
  109. Forro, L. *et al.* High mobility *n*-type charge carriers in large single crystals of anatase (TiO<sub>2</sub>). *J. Appl. Phys.* **75**, 633–635 (1994).
  110. Palermo, V. *et al.* Influence of Molecular Order on the Local Work Function of Nanographene Architectures: A Kelvin-Probe Force Microscopy Study. *ChemPhysChem* **6**, 2371–2375 (2005).
  111. Miyagi, T. *et al.* Deep Level Transient Spectroscopy Analysis of an Anatase Epitaxial Film Grown by Metal Organic Chemical Vapor Deposition. *Jpn. J. Appl. Phys.* **40**, L404–L406 (2001).
  112. Ono, L. K. & Qi, Y. Surface and Interface Aspects of Organometal Halide Perovskite Materials and Solar Cells. *J. Phys. Chem. Lett.* **7**, 4764–4794 (2016).
  113. Kronik, L. & Shapira, Y. Surface photovoltage spectroscopy of semiconductor structures: at the crossroads of physics, chemistry and electrical engineering. *Surf. Interface Anal.* **31**, 954–965 (2001).
  114. Brattain, W. H. & Bardeen, J. Surface Properties of Germanium. *Bell Syst. Tech. J.* **32**, 1–41 (1953).
  115. Colella, S. *et al.* MAPbI<sub>3</sub>-xCl<sub>x</sub> Mixed Halide Perovskite for Hybrid Solar Cells: The Role of Chloride as Dopant on the Transport



- and Structural Properties. *Chem. Mater.* **25**, 4613–4618 (2013).
116. Tsai, H. *et al.* Effect of Precursor Solution Aging on the Crystallinity and Photovoltaic Performance of Perovskite Solar Cells. *Adv. Energy Mater.* **7**, 1602159 (2017).
  117. Ball, J. M. *et al.* Optical properties and limiting photocurrent of thin-film perovskite solar cells. *Energy Env. Sci* **8**, 602–609 (2015).
  118. Aharon, S., Gamliel, S., Cohen, B. E. & Etgar, L. Depletion region effect of highly efficient hole conductor free CH<sub>3</sub>NH<sub>3</sub>PbI<sub>3</sub> perovskite solar cells. *Phys. Chem. Chem. Phys.* **16**, 10512 (2014).
  119. Yang, Y. *et al.* Low surface recombination velocity in solution-grown CH<sub>3</sub>NH<sub>3</sub>PbBr<sub>3</sub> perovskite single crystal. *Nat. Commun.* **6**, 7961 (2015).
  120. Levine, I. *et al.* Mobility–Lifetime Products in MAPbI<sub>3</sub> Films. *J. Phys. Chem. Lett.* **7**, 5219–5226 (2016).
  121. Zhou, H. *et al.* Interface engineering of highly efficient perovskite solar cells. *Science* **345**, 542–546 (2014).
  122. Lin, Q., Armin, A., Nagiri, R. C. R., Burn, P. L. & Meredith, P. Electro-optics of perovskite solar cells. *Nat. Photonics* **9**, 106–112 (2014).
  123. Green, M. A. Solar cells: operating principles, technology, and system applications. (1982).
  124. Benninghoven, A., Rudenauer, F. G. & Werner, H. W. Secondary ion mass spectrometry: basic concepts, instrumental aspects, applications and trends. (1987).
  125. Heath, J. T., Jiang, C.-S. & Al-Jassim, M. M. Diffused junctions in multicrystalline silicon solar cells studied by complementary scanning probe microscopy and scanning electron microscopy techniques. in 000227–000232 (IEEE, 2010). doi:10.1109/PVSC.2010.5614484
  126. Huang, Y. *et al.* Influence of Schottky contact on the C-V and J-V characteristics of HTM-free perovskite solar cells. *EPJ Photovolt.* **8**, 85501 (2017).
  127. Peiner, E. Doping Profile Analysis in Si by Electrochemical Capacitance-Voltage Measurements. *J. Electrochem. Soc.* **142**, 576 (1995).
  128. Jiang, C.-S., Moutinho, H. R., Reedy, R., Al-Jassim, M. M. & Blosse, A. Two-dimensional junction identification in multicrystalline silicon solar cells by scanning Kelvin probe force microscopy. *J. Appl. Phys.* **104**, 104501 (2008).



129. Narchi, P. *et al.* Cross-Sectional Investigations on Epitaxial Silicon Solar Cells by Kelvin and Conducting Probe Atomic Force Microscopy: Effect of Illumination. *Nanoscale Res. Lett.* **11**, (2016).
130. Dong, J., Shi, J., Li, D., Luo, Y. & Meng, Q. Controlling the conduction band offset for highly efficient ZnO nanorods based perovskite solar cell. *Appl. Phys. Lett.* **107**, 073507 (2015).
131. Malinkiewicz, O. *et al.* Perovskite solar cells employing organic charge-transport layers. *Nat. Photonics* **8**, 128–132 (2014).
132. Tsai, K.-W., Chueh, C.-C., Williams, S. T., Wen, T.-C. & Jen, A. K. Y. High-performance hole-transporting layer-free conventional perovskite/fullerene heterojunction thin-film solar cells. *J Mater Chem A* **3**, 9128–9132 (2015).
133. Schulz, P. *et al.* Interface energetics in organo-metal halide perovskite-based photovoltaic cells. *Energy Environ. Sci.* **7**, 1377–1381 (2014).
134. Saliba, M. *et al.* A molecularly engineered hole-transporting material for efficient perovskite solar cells. *Nat. Energy* **1**, 15017 (2016).
135. Chappaz-Gillot, C. *et al.* Polymer solar cells with electrodeposited CuSCN nanowires as new efficient hole transporting layer. *Sol. Energy Mater. Sol. Cells* **120, Part A**, 163–167 (2014).
136. Chen, W. *et al.* Efficient and stable large-area perovskite solar cells with inorganic charge extraction layers. *Science* **350**, 944–948 (2015).
137. Etgar, L. *et al.* Mesoscopic CH<sub>3</sub>NH<sub>3</sub>PbI<sub>3</sub>/TiO<sub>2</sub> Heterojunction Solar Cells. *J. Am. Chem. Soc.* **134**, 17396–17399 (2012).
138. Mei, A. *et al.* A hole-conductor-free, fully printable mesoscopic perovskite solar cell with high stability. *Science* **345**, 295–298 (2014).
139. Habisreutinger, S. N. *et al.* Enhanced Hole Extraction in Perovskite Solar Cells Through Carbon Nanotubes. *J. Phys. Chem. Lett.* **5**, 4207–4212 (2014).
140. Aitola, K. *et al.* Carbon nanotube-based hybrid hole-transporting material and selective contact for high efficiency perovskite solar cells. *Energy Environ. Sci.* **9**, 461–466 (2016).
141. Liu, X. *et al.* Electronic structures at the interface between Au and CH<sub>3</sub>NH<sub>3</sub>PbI<sub>3</sub>. *Phys. Chem. Chem. Phys.* **17**, 896–902 (2014).
142. Liu, G., Jaegermann, W., He, J., Sundström, V. & Sun, L. XPS and UPS Characterization of the TiO<sub>2</sub>/ZnPcGly Heterointer-



- face: Alignment of Energy Levels. *J. Phys. Chem. B* **106**, 5814–5819 (2002).
143. Miller, E. M. *et al.* Substrate-controlled band positions in CH<sub>3</sub>NH<sub>3</sub>PbI<sub>3</sub> perovskite films. *Phys. Chem. Chem. Phys.* **16**, 22122–22130 (2014).
  144. Wang, Q. *et al.* Qualifying composition dependent p and n self-doping in CH<sub>3</sub>NH<sub>3</sub>PbI<sub>3</sub>. *Appl. Phys. Lett.* **105**, 163508 (2014).
  145. Michaelson, H. B. The work function of the elements and its periodicity. *J. Appl. Phys.* **48**, 4729–4733 (1977).
  146. Pivrikas, A. *et al.* Bimolecular Recombination Coefficient as a Sensitive Testing Parameter for Low-Mobility Solar-Cell Materials. *Phys. Rev. Lett.* **94**, 176806 (2005).
  147. Wang, C. *et al.* Surface analytical investigation on organometal triiodide perovskite. *J. Vac. Sci. Technol. B* **33**, 032401 (2015).
  148. Laux, S. E. Techniques for small-signal analysis of semiconductor devices. *IEEE Trans. Electron Devices* **32**, 2028–2037 (1985).
  149. Morii, A., Okagawa, H., Hara, K., Yoshino, J. & Kukimoto, H. Band Discontinuity at Al<sub>x</sub>Ga<sub>1-x</sub>P/GaP Heterointerfaces Studied by Capacitance Measurements. *Jpn. J. Appl. Phys.* **31**, L1161–L1163 (1992).
  150. Kroemer, H., Chien, W.-Y., Jr, J. S. H. & Edwall, D. D. Measurement of isotype heterojunction barriers by C-V profiling. *Appl. Phys. Lett.* **36**, 295–297 (1980).
  151. Nakade, S. *et al.* Enhancement of electron transport in nano-porous TiO<sub>2</sub> electrodes by dye adsorption. *Electrochem. Commun.* **5**, 804–808 (2003).
  152. Sommeling, P. M. *et al.* Influence of a TiCl<sub>4</sub> Post-Treatment on Nanocrystalline TiO<sub>2</sub> Films in Dye-Sensitized Solar Cells. *J. Phys. Chem. B* **110**, 19191–19197 (2006).
  153. Gamliel, S., Dymshits, A., Aharon, S., Terkieltaub, E. & Etgar, L. Micrometer Sized Perovskite Crystals in Planar Hole Conductor Free Solar Cells. *J. Phys. Chem. C* **119**, 19722–19728 (2015).
  154. Zhang, W. *et al.* Enhancement of Perovskite-Based Solar Cells Employing Core–Shell Metal Nanoparticles. *Nano Lett.* **13**, 4505–4510 (2013).
  155. Yuan, Y. *et al.* Electric-Field-Driven Reversible Conversion Between Methylammonium Lead Triiodide Perovskites and Lead Iodide at Elevated Temperatures. *Adv. Energy Mater.* **6**, 1501803 (2016).
  156. Yun, J. S. *et al.* Critical Role of Grain Boundaries for Ion Migration in Formamidinium and Methylammonium Lead Halide



- Perovskite Solar Cells. *Adv. Energy Mater.* **6**, 1600330 (2016).
157. Yu, H., Lu, H., Xie, F., Zhou, S. & Zhao, N. Native Defect-Induced Hysteresis Behavior in Organolead Iodide Perovskite Solar Cells. *Adv. Funct. Mater.* **26**, 1411–1419 (2016).
  158. Cheng, Y.-B., Pascoe, A., Huang, F. & Peng, Y. Print flexible solar cells. *Nature* **539**, 488–489 (2016).
  159. Krebs, F. C., Tromholt, T. & Jørgensen, M. Upscaling of polymer solar cell fabrication using full roll-to-roll processing. *Nanoscale* **2**, 873 (2010).
  160. Feldt, S. M. *et al.* Design of Organic Dyes and Cobalt Polypyridine Redox Mediators for High-Efficiency Dye-Sensitized Solar Cells. *J. Am. Chem. Soc.* **132**, 16714–16724 (2010).
  161. Sargent, E. H. Colloidal quantum dot solar cells. *Nat. Photonics* **6**, 133–135 (2012).
  162. Voggu, V. R. *et al.* Flexible CuInSe<sub>2</sub> Nanocrystal Solar Cells on Paper. *ACS Energy Lett.* **2**, 574–581 (2017).
  163. Kim, B. J. & Jung, H. S. Flexible Perovskite Solar Cell. in *Organic-Inorganic Halide Perovskite Photovoltaics* (eds. Park, N.-G., Grätzel, M. & Miyasaka, T.) 325–341 (Springer International Publishing, 2016).  
doi:10.1007/978-3-319-35114-8\_13
  164. Yin, X. *et al.* Highly Efficient Flexible Perovskite Solar Cells Using Solution-Derived NiOx Hole Contacts. *ACS Nano* **10**, 3630–3636 (2016).
  165. Yang, D. *et al.* Hysteresis-Suppressed High-Efficiency Flexible Perovskite Solar Cells Using Solid-State Ionic-Liquids for Effective Electron Transport. *Adv. Mater.* **28**, 5206–5213 (2016).
  166. Wang, K. *et al.* W(Nb)Ox-based efficient flexible perovskite solar cells: From material optimization to working principle. *Nano Energy* **31**, 424–431 (2017).
  167. Mahmood, K., Swain, B. S., Kirmani, A. R. & Amassian, A. Highly efficient perovskite solar cells based on a nanostructured WO<sub>3</sub>–TiO<sub>2</sub> core–shell electron transporting material. *J. Mater. Chem. A* **3**, 9051–9057 (2015).
  168. Gheno, A., Vedraïne, S., Boucle, J. & Ratier, B. Low-temperature annealed printed perovskite solar cells: the role of chlorine in wetting conditions. in (2017).
  169. Wiley: Physics of Semiconductor Devices, 3rd Edition - Simon M. Sze, Kwok K. Ng. Available at:  
<http://eu.wiley.com/WileyCDA/WileyTitle/productCd-0471143235.html>. (Accessed: 23rd May 2016)



170. Zhang, F. *et al.* Interfacial Oxygen Vacancies as a Potential Cause of Hysteresis in Perovskite Solar Cells. *Chem. Mater.* **28**, 802–812 (2016).
171. Ogomi, Y. *et al.* Control of Charge Dynamics through a Charge-Separation Interface for All-Solid Perovskite-Sensitized Solar Cells. *ChemPhysChem* **15**, 1062–1069 (2014).
172. Eames, C. *et al.* Ionic transport in hybrid lead iodide perovskite solar cells. *Nat. Commun.* **6**, 7497 (2015).
173. Azpiroz, J. M., Mosconi, E., Bisquert, J. & De Angelis, F. Defect migration in methylammonium lead iodide and its role in perovskite solar cell operation. *Energy Env. Sci* **8**, 2118–2127 (2015).
174. Miller, O. D., Yablonovitch, E. & Kurtz, S. R. Strong Internal and External Luminescence as Solar Cells Approach the Shockley–Queisser Limit. *IEEE J. Photovolt.* **2**, 303–311 (2012).
175. Lee, H. *et al.* Direct Experimental Evidence of Halide Ionic Migration under Bias in  $\text{CH}_3\text{NH}_3\text{Pb}_{1-x}\text{Cl}_x$ -Based Perovskite Solar Cells Using GD-OES Analysis. *ACS Energy Lett.* **2**, 943–949 (2017).
176. Mosconi, E., Meggiolaro, D., Snaith, H. J., Stranks, S. D. & De Angelis, F. Light-induced annihilation of Frenkel defects in organo-lead halide perovskites. *Energy Env. Sci* **9**, 3180–3187 (2016).
177. Staebler, D. L. & Wronski, C. R. Reversible conductivity changes in discharge-produced amorphous Si. *Appl. Phys. Lett.* **31**, 292–294 (1977).
178. Meftah, A. F., Meftah, A. M. & Merazga, A. A theoretical study of light induced defect creation, annealing and photoconductivity degradation in a-Si:H. *J. Phys. Condens. Matter* **16**, 3107–3116 (2004).
179. Shockley, W. & Queisser, H. J. Detailed Balance Limit of Efficiency of p-n Junction Solar Cells. *J. Appl. Phys.* **32**, 510–519 (1961).
180. Adhyaksa, G. W. P., Johlin, E. & Garnett, E. C. Nanoscale Back Contact Perovskite Solar Cell Design for Improved Tandem Efficiency. *Nano Lett.* **17**, 5206–5212 (2017).
181. Kurtz, S. R., Faine, P. & Olson, J. M. Modeling of two-junction, series-connected tandem solar cells using top-cell thickness as an adjustable parameter. *J. Appl. Phys.* **68**, 1890–1895 (1990).
182. Vurgaftman, I., Meyer, J. R. & Ram-Mohan, L. R. Band parameters for III–V compound semiconductors and their alloys. *J. Appl. Phys.* **89**, 5815 (2001).
183. Seyrling, S. *et al.*  $\text{CuIn}_{1-x}\text{Ga}_x\text{Se}_2$  photovoltaic devices for tandem solar cell appli-



- cation. *Thin Solid Films* **517**, 2411–2414 (2009).
184. Noh, J. H., Im, S. H., Heo, J. H., Mandal, T. N. & Seok, S. I. Chemical Management for Colorful, Efficient, and Stable Inorganic–Organic Hybrid Nanostructured Solar Cells. *Nano Lett.* **13**, 1764–1769 (2013).
  185. Mailoa, J. P. *et al.* A 2-terminal perovskite/silicon multijunction solar cell enabled by a silicon tunnel junction. *Appl. Phys. Lett.* **106**, 121105 (2015).
  186. Bush, K. A. *et al.* 23.6%-efficient monolithic perovskite/silicon tandem solar cells with improved stability. *Nat. Energy* **2**, 17009 (2017).
  187. Sheng, R. *et al.* Four-Terminal Tandem Solar Cells Using  $\text{CH}_3\text{NH}_3\text{PbBr}_3$  by Spectrum Splitting. *J. Phys. Chem. Lett.* **6**, 3931–3934 (2015).
  188. Baudrit, M. & Algara, C. Modeling of GaInP/GaAs Dual-Junction solar cells including Tunnel Junction. in *33rd IEEE Photovoltaic Specialists Conference, 2008. PVSC '08* 1–5 (2008). doi:10.1109/PVSC.2008.4922476
  189. Baudrit, M. & Algara, C. Tunnel Diode Modeling, Including Nonlocal Trap-Assisted Tunneling: A Focus on III–V Multijunction Solar Cell Simulation. *IEEE Trans. Electron Devices* **57**, 2564–2571 (2010).
  190. Rolland, A. *et al.* Design of a lattice-matched III–V–N/Si photovoltaic tandem cell monolithically integrated on silicon substrate. *Opt. Quantum Electron.* **46**, 1397–1403 (2014).
  191. Keiser, G. Optical Fiber Communications. in *Wiley Encyclopedia of Telecommunications* (ed. Proakis, J. G.) (John Wiley & Sons, Inc., 2003). doi:10.1002/0471219282.eot158
  192. Wang, Z. *et al.* Novel Light Source Integration Approaches for Silicon Photonics: Novel Light Source Integration Approaches for Silicon Photonics. *Laser Photonics Rev.* **11**, 1700063 (2017).
  193. Li, T., Mastro, M. & Dadgar, A. *III–V Compound Semiconductors: Integration with Silicon-Based Microelectronics*. (CRC Press, 2010).
  194. Chen, S. *et al.* Electrically pumped continuous-wave 1.3  $\mu\text{m}$  InAs/GaAs quantum dot lasers monolithically grown on on-axis Si (001) substrates. *Opt. Express* **25**, 4632 (2017).
  195. Wan, Y. *et al.* 1.3  $\mu\text{m}$  submilliamp threshold quantum dot micro-lasers on Si. *Optica* **4**, 940 (2017).
  196. Megalini, L. *et al.* 1550-nm InGaAsP multi-quantum-well structures selectively



- grown on v-groove-patterned SOI substrates. *Appl. Phys. Lett.* **111**, 032105 (2017).
197. Liu, A. Y. *et al.* Electrically pumped continuous-wave 1.3  $\mu\text{m}$  quantum-dot lasers epitaxially grown on on-axis (001) GaP/Si. *Opt. Lett.* **42**, 338 (2017).
  198. Liebich, S. *et al.* Laser operation of Ga(NAsP) lattice-matched to (001) silicon substrate. *Appl. Phys. Lett.* **99**, 071109 (2011).
  199. Robert, C., Perrin, M., Cornet, C., Even, J. & Jancu, J. M. Atomistic calculations of Ga(NAsP)/GaP(N) quantum wells on silicon substrate: Band structure and optical gain. *Appl. Phys. Lett.* **100**, 111901 (2012).
  200. Nguyen Thanh, T. *et al.* Room temperature photoluminescence of high density (In,Ga)As/GaP quantum dots. *Appl. Phys. Lett.* **99**, 143123 (2011).
  201. Song, Y. & Lee, M. L. InGaAs/GaP quantum dot light-emitting diodes on Si. *Appl. Phys. Lett.* **103**, 141906 (2013).
  202. Shen, J., Song, Y., Lee, M. L. & Cha, J. J. Spatially resolved In and As distributions in InGaAs/GaP and InGaAs/GaAs quantum dot systems. *Nanotechnology* **25**, 465702 (2014).
  203. Stracke, G. *et al.* Indirect and direct optical transitions in  $\text{In}_{0.5}\text{Ga}_{0.5}\text{As}/\text{GaP}$  quantum dots. *Appl. Phys. Lett.* **104**, 123107 (2014).
  204. Golz, C., Dadgostar, S., Masselink, W. T. & Hatami, F. Thermal behavior and carrier injection of GaAs/GaP quantum dots light emitting diodes. *Appl. Phys. Lett.* **110**, 091101 (2017).
  205. Heidemann, M., Höfling, S. & Kamp, M. (In,Ga)As/GaP electrical injection quantum dot laser. *Appl. Phys. Lett.* **104**, 011113 (2014).
  206. Goetz, K. -H. *et al.* Optical and crystallographic properties and impurity incorporation of  $\text{Ga}_x\text{In}_{1-x}\text{As}$  ( $0.44 < x < 0.49$ ) grown by liquid phase epitaxy, vapor phase epitaxy, and metal organic chemical vapor deposition. *J. Appl. Phys.* **54**, 4543–4552 (1983).
  207. Fukami, F. *et al.* Analysis of quantum levels for self-assembled InGaAsN/GaP quantum dots. *Phys. Status Solidi C* **8**, 322–324 (2011).
  208. Robert, C. *et al.* Electronic, optical, and structural properties of (In,Ga)As/GaP quantum dots. *Phys. Rev. B* **86**, (2012).
  209. Quinci, T. *et al.* Defects limitation in epitaxial GaP on bisterped Si surface using UHV-CVD–MBE growth cluster. *J. Cryst. Growth* **380**, 157–162 (2013).



210. Tremblay, R. *et al.* MBE growth and doping of AlGaP. *J. Cryst. Growth* **466**, 6–15 (2017).
211. Robert, C. *et al.* Structural and optical properties of AlGaP confinement layers and InGaAs quantum dot light emitters onto GaP substrate: Towards photonics on silicon applications. *Thin Solid Films* **541**, 87–91 (2013).
212. Gauthier, J.-P. *et al.* Electrical injection in GaP-based laser waveguides and active areas. in 1–2 (IEEE, 2014). doi:10.1109/ICIPRM.2014.6880545
213. Sanguinetti, S. *et al.* Carrier thermal escape and retrapping in self-assembled quantum dots. *Phys. Rev. B* **60**, 8276–8283 (1999).
214. Giorgi, G., Fujisawa, J.-I., Segawa, H. & Yamashita, K. Small Photocarrier Effective Masses Featuring Ambipolar Transport in Methylammonium Lead Iodide Perovskite: A Density Functional Analysis. *J. Phys. Chem. Lett.* **4**, 4213–4216 (2013).
215. Nguyen, W. H., Bailie, C. D., Unger, E. L. & McGehee, M. D. Enhancing the Hole-Conductivity of Spiro-OMeTAD without Oxygen or Lithium Salts by Using Spiro(TFSI)<sub>2</sub> in Perovskite and Dye-Sensitized Solar Cells. *J. Am. Chem. Soc.* **136**, 10996–11001 (2014).
216. Spiro-OMeTAD (Spiro-MeOTAD). *Ossila* Available at: <https://www.ossila.com/products/spiro-ometad>. (Accessed: 4th April 2017)
217. Lucci, I., Cornet, C., Bahri, M. & Léger, Y. Thermal Management of Monolithic vs Heterogeneous Lasers Integrated on Silicon. *Submitt. IEEE Sel. Top. Quantum Electron.* (2016).
218. Suski, T. & Paul, W. *High pressure in semiconductor physics*. (Academic Press, 1998).



## List of publication

R. Tremblay, **Y. Huang**, J.P. Gauthier, R. Piron, A. Beck, C. Levallois, C. Paranthoën, J. P. Burin, L. Pedesseau, J. Even, T. Rohel, K. Tavernier, J. Stervinou, A. Balocchi, H. Carrère, X. Marie, O. Durand, Y. Léger and C. Cornet, Electroluminescence of InGaAs/GaP quantum dots and band engineering of AlGaP/GaP laser injection layers, Compound semiconductor week (2015)

L. Pedesseau, M. Kepenekian, D. Saponi, **Y. Huang**, A. Rolland, A. Beck, C. Cornet, O. Durand, S. Wang, C. Katan and J. Even, Dielectric properties of hybrid perovskites and drift-diffusion modelling of perovskite/silicon tandem cells, SPIE Photonics West conference (2016)

**Y. Huang**, S. Aharon, A. Rolland, L. Pedesseau, O. Durand, L. Etgar and J. Even, Influence of Schottky contact on the CV and JV characteristics of HTM-free perovskite solar cells, EPJ Photovoltaics 8, 85501 (2017)

**Y. Huang**, S. Aharon, A. Gheno, S. Vedraïne, L. Pedesseau, J. P. Burin, O. Durand, J. Bouclé, L. Etgar, J. Even and A. Rolland, Numerical simulation of HTM-free and WO<sub>x</sub> based perovskite cells: Effects of interface conditions, Numerical Simulation of Optoelectronic Devices (NUSOD) international Conference (2017)

**Y. Huang**, A. Gheno, A. Rolland, L. Pedesseau, S. Vedraïne, O. Durand, J. Bouclé, J. P. Connolly, L. Etgar and J. Even, A new approach to the modelling of Kelvin Probe Force Microscopy of heterostructures in dark and under illumination, Optical and Quantum Electronics 50, 41 (2018).

**Y. Huang**, S. Aharon, A. Gheno, S. Vedraïne, L. Pedesseau, J. P. Connolly, C. Katan, M. Kepenekian, J. P. Burin, O. Durand, J. Bouclé, L. Etgar, J. Even, A. Rolland, Numerical investigation of the effect of interface conditions in HTM-free, printable WO<sub>x</sub> based and inverted perovskite solar cells, ABXPV-PEROPTO (2018)

A. Rolland, L. Pedesseau, M. Kepenekian, C. Katan, **Y. Huang**, S. Wang, C. Cornet, O. Durand, J. Even, Computational analysis of hybrid perovskite on silicon 2-T tandem solar cells based on a Si tunnel junction, Optical and Quantum Electronics (2018) 50:21

**Y. Huang**, A. Rolland, J. Even, Modelling of V<sub>OC</sub> loss, hysteresis effect, and J<sub>SC</sub> degradation of perovskite solar cells, under preparation...

**Y. Huang**, R. Tremblay, A. Rolland, J. Even, Y. Léger and C. Cornet, Carrier transport in (In,Ga)As/GaP QDs based devices under electrical injection, under preparation...



## AVIS DU JURY SUR LA REPRODUCTION DE LA THESE SOUTENUE

**Titre de la thèse:**

Modélisation des cellules solaires pérovskites, des dispositifs optoélectroniques III-V et de la microscopie à sonde de Kelvin

**Nom Prénom de l'auteur : HUANG YONG**

**Membres du jury :**

- Monsieur RATIER Bernard
- Monsieur EVEN Jacky
- Monsieur ROLLAND Alain
- Madame DELEPORTE Emmanuelle
- Madame KATAN Claudine
- Monsieur REISS Peter
- Monsieur DJEBBOUR Zakaria

Président du jury : *Bernard RATIER*

Date de la soutenance : 14 Mars 2018

Reproduction de la these soutenue

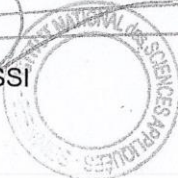
- ☒ Thèse pouvant être reproduite en l'état  
☐ Thèse pouvant être reproduite après corrections suggérées

Fait à Rennes, le 14 Mars 2018

Signature du président de jury

Le Directeur,

M'hamed DRISSI





## Résumé

Ce travail de thèse se concentre sur l'étude des modèles de type drift-diffusion. Des approches sont développées pour la modélisation de la Microscopie à sonde de Kelvin, des cellules solaires à base de matériaux pérovskites (PSCs), des cellules solaires tandem de type pérovskite/silicium et des îlots quantiques III-V/GaP. Tout d'abord, l'approche de la modélisation de la sonde de Kelvin est examinée pour la surface de TiOx et l'absorbeur pérovskite MAPbI3. Ensuite, des mesures avec sonde de Kelvin et des simulations sont proposées pour des jonctions diffusées à base de silicium et pour des PSCs à base de TiOx méso poreux. Les variations du potentiel interne sont étudiées, ouvrant la voie à une amélioration supplémentaire des dispositifs. L'influence de l'état de surface des couches WOx sur des mesures à sonde de Kelvin est étudiée théoriquement. Différents facteurs à l'origine des pertes de tension de circuit ouvert (Voc) des PSCs sont discutés. L'effet anormal d'hystérésis dans les PSCs est également simulé, en tenant compte des états de pièges d'interface et des ions mobiles. En outre, le design de cellules solaires tandem 2T pérovskite/silicium est étudié en détails. Une jonction tunnel à base de silicium entre les deux sous-cellules supérieure et inférieure est proposée pour assurer le bon fonctionnement des cellules en série. L'influence du profil de dopage dans la jonction tunnel est discutée. Au final, le transport des porteurs dans les îlots quantiques III-V/GaP est étudié dans le cadre plus général de l'intégration d'émetteurs III-V sur silicium. Les caractéristiques électroluminescentes et électriques de ces structures sont simulées dans une approximation symétrie cylindrique.

## Abstract

This PhD work focuses on optoelectronic device simulations based on drift-diffusion models. Approaches are developed for the modelling of Kelvin Probe Force Microscopy (KPFM), perovskite-based solar cells (PSCs), perovskite/silicon tandem solar cells and III-V/GaP quantum dots (QDs). Firstly, a new approach for the modelling of KPFM is applied to TiOx slabs and to the MAPbI3 perovskite absorber. Secondly, KPFM measurements and simulations are proposed for silicon-based diffused junctions and mesoporous TiOx based PSCs. The built-in potential is investigated, and this study paves the way toward further device improvements. In addition, the influence of the surface of WOx slabs on KPFM measurements is studied theoretically. Various factors influencing open circuit voltage (Voc) losses in PSCs are discussed. The abnormal hysteresis effect in the PSCs is simulated as well, considering interface trap states and mobile ions. The design of two-terminal perovskite/silicon tandem solar cells is studied in detail. A silicon based tunnel junction between the top and the bottom subcells is proposed for series current matching. The influence of the doping profile in the tunnel junction is discussed. At the end of the manuscript, the carrier transport in III-V/GaP QDs is investigated, for the integration of III-V emitters on silicon. The electro luminescence and electrical characteristics of these III-V light emitting devices are simulated by using a cylindrical approximation.